

# The dangling-bond defect in silicon

Insights into electronic and structural effects from first-principles  
calculations of the EPR-parameters

Gernot Pfanner

## **Dissertation**

zur Erlangung des akademischen Grades

DOCTOR RERUM NATURALIUM

vorgelegt der

Universität Gesamthochschule Paderborn

- Department Physik, Fakultät für Naturwissenschaften -

Promotionskommission

Vorsitzender:	Prof. Dr. habil. Klaus Lischka
Erstgutachter:	Prof. Dr. habil. Jörg Neugebauer
Zweitgutachter:	Prof. Dr. habil. Wolf Gero Schmidt



# Abstract

Hydrogenated amorphous silicon (a-Si:H) is an attractive material for low-cost solar cells. However, the light-induced formation of metastable defects leads to a degradation of the conversion efficiency with time. After more than 30 years of research, the common notion is that the 'dangling-bond' (db) defect plays an important role in it but the specific underlying mechanisms of this Staebler-Wronski effect (SWE) are still unknown. The db-defect is a singly under-coordinated silicon atom, that gives rise to a state in the band gap. If the state is singly occupied, it can be detected by electron spin resonance (EPR), which probes for the unpaired spin in an external magnetic field. In a-Si:H, the resulting absorption spectrum is characterized by the coupling of the unpaired spin with the external magnetic field (described by the  $g$ -tensor) and the hyperfine coupling to the central nucleus of the defect.

The complexity of the material makes it impossible to directly extract information about the local defect structure from the spectrum. To solve this problem, this thesis analyses the role of electronic and structural effects on the EPR-parameters of the silicon dangling bond by means of state-of-the-art *ab initio* computational methods. By their application, we are able to compute the EPR-parameters for realistic defect models and study their statistics. On the other hand, we can also study the influence of the further defect surrounding in a systematic way. The complementary statistical and systematic modelling is crucial for understanding the paramagnetic characteristics in such a complex material as a-Si:H, in which structural disorder leads to a strong influence of the network and to an huge variety of different local bond geometries.

First we establish the accuracy of our approach by considering small molecular and crystalline (c-Si) db-systems. We compare our method with another theoretical approach and we obtain excellent agreement with experiment for carefully selected c-Si dangling bonds. Consequently, we are able to relate the measured EPR-parameters to specific atomistic defect models and characterize the effect of a symmetry-lowering Jahn-Teller distortion.

We then use the molecular and c-Si db-systems to study the influence of the local defect geometry on the EPR-parameters in a systematic way. The  $g$ -tensor reacts sensitively to energy differences of the local electronic structure, which cannot be always interpreted intuitively. In contrast to this, the hyperfine interaction is characterized by the interplay between the expected  $sp$ -hybridization of the db-orbital as well as the spin delocalization, which can only be captured by our network models.

Since the generation of realistic amorphous structures is difficult, we can only calculate the EPR-parameters for a moderate number of defect configurations ( $\sim 50$  models). Within the limitations of this small statistics, we are still able to understand recent experimental findings and obtain insights into the role of the EPR-tensors specific to the amorphous defect environment. Yet the experimentally observed red-shift of the hyperfine satellites in a-Si:H can only be reproduced in part.

From the categorization of the a-Si:H dangling bonds by carefully chosen criteria, we show that they differ substantially from their crystalline counterparts. In contrast to the vacancy-related c-Si db-defect, it forms rather spontaneously in the network at suitable geometric distortions. For the modelling of the SWE by the db-defect, this suggests that the local structural disorder is an important influence.

Finally, we look at the effect of strain on the hyperfine interaction of our crystalline and amorphous db-models. Whereas the c-Si db-models follow essentially the intuitive trends expected from an  $sp$ -hybridization of the db-orbital, the a-Si:H db undergoes delocalization for compressive strain. This illustrates again the different origins of the db-defect in both phases of silicon. The investigation also suggests strain as a possible mechanism behind the remaining discrepancy between theoretical and experimental results, and our calculations point out the importance of this question, which has to be clarified by future experiments.



# Zusammenfassung

Wasserstoffhaltiges amorphes Silizium (a-Si:H) ist ein vielversprechendes Material für kostengünstige Solarzellen. Jedoch führt die lichtinduzierte Erzeugung von metastabilen Defekten mit der Zeit zu einer Degradierung der Stromumwandlungseffizienz. Nach mehr als dreißigjähriger Forschung ist die gängige Auffassung, dass der 'dangling bond' (db) Defekt eine wichtige Rolle spielt, aber die genauen Mechanismen dieses 'Staebler-Wronski'-Effektes (SWE) sind noch immer unbekannt. Der db-Defekt kennzeichnet ein einfach-unterkoordiniertes Siliziumatom, welches zu einem Zustand in der Bandlücke führt. Wenn dieser Zustand einfach besetzt ist, ist er mit Elektronenspinresonanz detektierbar, wobei diese experimentelle Methode auf der Messung des ungepaarten Spins in einem externen Magnetfeld basiert. In amorphen Silizium wird das resultierende Absorptionsspektrum von der Wechselwirkung des ungepaarten Spins mit dem externen Magnetfeld (charakterisiert durch den  $g$ -tensor) und die Hyperfeinkopplung mit dem Zentralatom des Defektes geprägt.

Die Komplexität des Materials macht es unmöglich, direkte Informationen über die lokale Defektstruktur aus dem Spektrum abzuleiten. Aus diesem Grunde beschäftigt sich diese Arbeit mit dem Einfluss elektronischer und struktureller Effekte auf die EPR-Parameter für den Silizium dangling bond. Dazu werden hochmoderne Computermethoden angewandt, die es uns ermöglichen, die EPR-Parameter für realistische Defektmodelle zu berechnen. Insbesondere können wir damit auch den Einfluss der weiteren Defektumgebung in einer systematischen Art und Weise untersuchen. Die komplementäre statistische und systematische Modellierung ist essenziell, um die paramagnetischen Eigenschaften in so einem komplexen Material wie a-Si:H zu verstehen, da die strukturelle Unordnung zu einem starken Einfluss des Netzwerkes und einer Vielzahl lokaler Bindungsgeometrien führt.

Zunächst erbringen wir den Nachweis über die Genauigkeit unseres Zuganges, in dem wir einfache molekulare und kristalline (c-Si) db-Systeme betrachten. Wir vergleichen unsere Methode mit einem anderen theoretischen Ansatz, und erhalten exzellente Übereinstimmung mit dem Experiment für sorgsam gewählte c-Si dangling bonds. Wir sind daher in der Lage, die gemessenen EPR-Parameter spezifischen atomistischen Defektmodellen zuzuordnen und Effekte wie z.B. eine Symmetrie-reduzierende Jahn-Teller-Verzerrung zu charakterisieren.

Desweiteren verwenden wir die molekularen und c-Si db-Systeme, um systematisch den Einfluss der lokalen Defektgeometrie auf die EPR-Parameter zu untersuchen. Der  $g$ -Tensor reagiert sensitiv auf Energiedifferenzen in der lokalen elektronischen Struktur, die nicht immer intuitiv erklärbar sind. Im Gegensatz dazu ist die Hyperfein-Wechselwirkung durch das Zusammenspiel der erwartungsgemäßen  $sp$ -Hybridisierung des db-Orbitals sowie der Spindelokalisierung gekennzeichnet. Letztere kann nur durch unsere Netzwerkmodelle erfasst werden.

Da die Generierung von realistischen amorphen Strukturen schwierig ist, können wir die EPR-Parameter nur für eine moderate Anzahl von Defektkonfigurationen berechnen (ca. 50 Modelle). Trotz dieser statistischen Einschränkung sind wir in der Lage kürzlich gefundene experimentelle Ergebnisse zu erklären und erhalten Einblicke in die Rolle der EPR-Tensoren in der amorphen Defektumgebung. Die experimentell beobachtete Rotverschiebung der Hyperfein-Satelliten in a-Si:H können wir nur zum Teil reproduzieren.

Durch die Klassifizierung der a-Si:H dangling bonds durch sorgsam gewählte Kriterien zeigen wir, dass sich diese substantiell von ihren kristallinen Gegenständen unterscheiden. Im Gegensatz zu den Vakanz-basierten c-Si db-Defekten, entstehen die a-Si:H spontan im Netzwerk an geeigneten geometrischen Verzerrungen. Für die Modellierung des SWE bedeutet dies, dass die lokale strukturelle Unordnung einen wichtigen Einfluss darstellt.

Zuletzt betrachten wir den Effekt von elastischer Verspannung auf die Hyperfein-Wechselwirkung in unseren kristallinen und amorphen db-Modellen. Während die c-Si db-Modelle praktisch dem intuitiven

Trend gemäß der *sp*-Hybridisierung des db-Orbitals folgen, delokalisieren die a-Si:H unter Kompression. Dies veranschaulicht wiederum die verschiedenen Ursprünge des db-Defekts in beiden Phasen von Silizium. Unsere Untersuchung regt auch an, dass Verspannungen die verbleibende Diskrepanz zwischen theoretischen und experimentellen Ergebnissen zumindest teilweise erklären könnten und weist auf die Bedeutung dieser Fragestellung hin, die durch zukünftige Experimente abgeklärt werden sollte.



# Contents

<b>1</b>	<b>Introduction: a-Si:H solar cells</b>	<b>10</b>
<b>2</b>	<b>Electron paramagnetic resonance</b>	<b>18</b>
2.1	Introduction . . . . .	18
2.2	EPR-parameters . . . . .	22
2.2.1	Overview . . . . .	22
2.2.2	The electron Zeeman interaction . . . . .	23
2.2.3	The hyperfine interaction . . . . .	25
2.3	Summary . . . . .	30
<b>3</b>	<b>Theoretical modelling of EPR-parameters</b>	<b>31</b>
3.1	Density-functional theory . . . . .	31
3.1.1	Fundamental concepts . . . . .	31
3.1.2	Practical aspects of DFT-calculations . . . . .	34
3.2	The g-tensor . . . . .	42
3.3	Hyperfine parameters . . . . .	46
3.4	Summary . . . . .	49
<b>4</b>	<b>Dangling bonds in molecular and crystalline silicon systems</b>	<b>50</b>
4.1	Modelling . . . . .	50
4.2	Quantification of the accuracy . . . . .	52
4.2.1	Convergence tests . . . . .	52
4.2.2	Comparison to an all-electron method . . . . .	56
4.2.3	Comparison to experiment . . . . .	56
4.3	General characteristics of the db-defect . . . . .	62
4.3.1	Molecular dangling bonds . . . . .	62
4.3.2	Crystalline dangling bonds . . . . .	64
4.3.3	Hydrogen . . . . .	66
4.4	Bond-parameter trends of EPR-parameters . . . . .	67
4.4.1	Bond-parameter dependence of the tetrasilyl radical . . . . .	67
4.4.2	Bond-angle dependence of c-Si models . . . . .	70
4.4.3	Strain dependence of c-Si models . . . . .	74
4.5	Summary . . . . .	76
<b>5</b>	<b>Dangling bonds in hydrogenated amorphous silicon</b>	<b>77</b>
5.1	Modelling . . . . .	77
5.2	Statistical analysis of EPR-parameters . . . . .	81

5.3	Structural aspects of dangling bonds in a-Si:H . . . . .	86
5.3.1	Categorization . . . . .	86
5.3.2	Localized db-defects . . . . .	88
5.3.3	Hydrogen . . . . .	92
5.4	The discrepancy between theory and experiment . . . . .	93
5.4.1	Methodological aspects . . . . .	93
5.4.2	Charging . . . . .	95
5.4.3	Strain . . . . .	97
5.5	Summary and Outlook . . . . .	100

# 1 Introduction: a-Si:H solar cells

The efficient storage and conversion of energy has become a key problem for our civilization, since fossil energy sources lack sustainability. For illustration, 80% of global primary energy is produced using fossil fuels (coal, oil, gas), and this percentage is expected to decrease only marginally in the next two decades [1]. The rest is shared between biomass and waste energy (10%), nuclear energy (6%), hydro energy (2%) and non-hydro modern renewable technologies including wind, solar, geothermal, tide and wave energy (2%). Within the last category, wind and solar power are the most promising future energy sources. For example, the International Energy Agency aims to increase the solar-energy contribution to 10% within the next 40 years [2].

At first glance, it is peculiar that solar energy contributes only a small part to the overall production, since in a single hour the sun provides enough energy to meet the annual global energy demand [2, 3]. The rather simple reason for this is that the retail price of solar-generated electricity is high even when compared to other renewable energy resources such as hydro, biomass or wind. Consequently, an important goal is to make photovoltaics more competitive. This can essentially be accomplished by improving the conversion efficiency and lowering the production costs.

There are three ways to use the sun's energy [2, 4]. First, there is direct conversion to electricity in photovoltaic cells, which is rather flexible and also suited for small-scale applications. Second, 'concentrated power systems' focus the solar energy to heat a receiver to high temperatures. The heat is then transferred first to mechanical energy (e.g. by turbines) and later to electricity. This approach also has the advantage of thermal storage, which makes it more adaptable to peak loads of electricity demand. Third and finally, one can directly use the thermal energy of the sun to heat or cool buildings.

The presented work is motivated by questions related to solar cells. Therefore let us briefly discuss the working principle of this device as sketched in Figure 1.1(a) [5, 6, 7, 8, 9]. Let us first consider the effect of doping in silicon. Group-V elements (phosphorus, arsenic, antimony) contribute one weakly-bond electron to the host lattice, which can be promoted to the conduction band by interacting with phonons. The impurity is thus an electron donor and the material is called '*n*-doped'. Conversely, Group-III elements (boron, aluminum, gallium, indium) remove free electrons from the crystal lattice, i.e. contribute hole states. These impurities consequently act as electron acceptors and the material is then *p*-doped. If both, *p*- and *n*-type silicon are brought in contact, a *pn*-junction is created. In this device, the higher free-electron concentration in the *n*-type material leads to a diffusion of electrons to the *p*-type layer. Similarly, free holes move from the *p*- to the *n*-type material. However, the fixed donor and acceptor impurity ions (now charge-unbalanced) create an internal electrostatic field, which prevents the

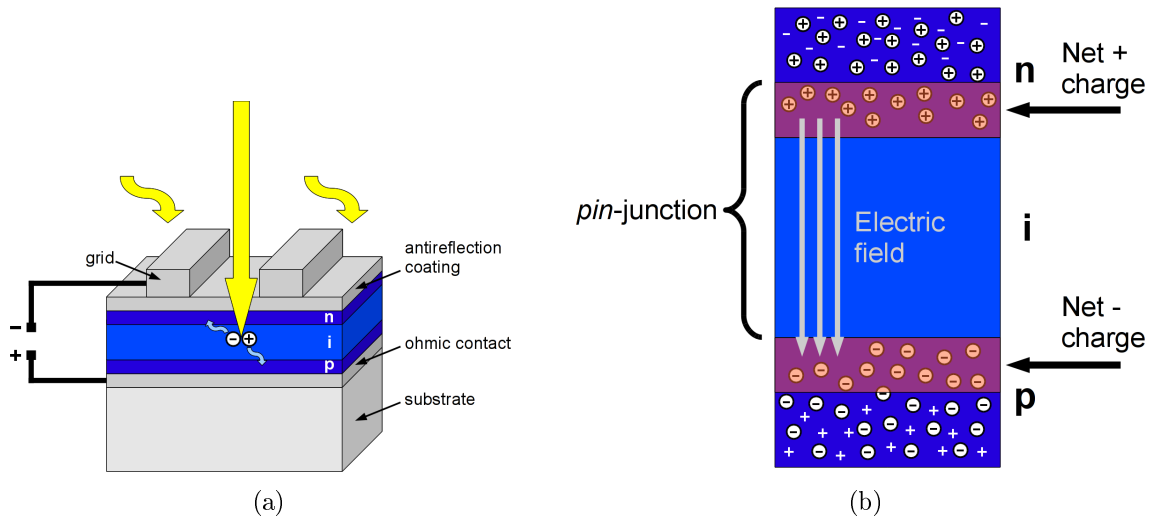


Figure 1.1: (a): Sketch of a solar cell with an intrinsic layer. Light creates electron-hole pairs, which drift towards opposite layers due to the internal electric field between the *n*- and *p*-layer. Figure (b) illustrates the charge distribution in a *pin*-junction in more detail.

complete diffusion of electrons and holes. Instead, a region with a net positive charge (on the *n*-doped side) and one with a net negative charge (on the *p*-doped side) builds up. Consequently, in thermal equilibrium no current will flow. However, light can create electron-hole pairs in the interface. The internal field then causes the electron to move to the *n*-side (making it negative) and the hole to the *p*-side (making it positive). In result, a bias between the ends of the device appears.

Hydrogenated amorphous silicon (a-Si:H) solar cells actually have a *pin*-device structure, where a-Si:H is usually used only for the intrinsic absorption layer and microcrystalline silicon for the contacts [10, 11, 12]. The *n*- and *p*-type layers are much smaller (<100 nm) than the *i*-layer (typically a few hundred nanometers) [8]. The *pin*-layout is necessary, since doped a-Si:H has a high defect density and therefore minority photo-carriers cannot move over a large range. The electronic characteristics of a *pin*-junction is depicted in Figure 1.2(a). Across the device, the bands are bent upwards in the direction of the electric field. The absorption of a photon promotes an electron from the valence- to the conduction band, leaving a hole behind. The electron then drifts to the minimum of the conduction band (on the *n*-doped side) and the hole to the maximum of the valence band (on the *p*-doped side).

A key characteristic of a solar cell is its conversion efficiency, which is defined as the ratio between the power output and the incident power [6, 13]. The power input is defined as the product of the device area and the total energy of the incident photons summed over all wavelengths. The power output depends on the product between the short-circuit current and the open-circuit voltage as well as a fill factor characterizing various loss effects with respect to the maximum power. One can then show that the

Solar-cell material	$\eta_{prod}$ (%)	$\eta_{R\&D}$ (%)	World production 2007 (MW)
<i>Bulk solar cells</i>			
Single crystal Si	13-18	25.0 (4 cm <sup>2</sup> )	1.355 (37%)
Multicrystalline Si	13-15	20.4 (1 cm <sup>2</sup> )	1.837 (51%)
GaInP/GaAs/Ge- Triple junction	-	41.1 (0.05 cm <sup>2</sup> ) [454 suns]	-
<i>Thin-film solar cells</i>			
a-Si	6-7	9.5 (1 cm <sup>2</sup> )	168 (5%) [part]
a-Si/ $\mu$ -Si	9-10	15.0 (1 cm <sup>2</sup> )	168 (5%) [part]
Double junction			
Cu(InGa)Se <sub>2</sub>	10-11	19.4 (1 cm <sup>2</sup> )	40 (1%)
CdTe	10-11	16.7 (1 cm <sup>2</sup> )	219 (6%)
Dye-sensitized	-	10.4 (1 cm <sup>2</sup> )	-
Organic semiconductor	-	5.15 (1 cm <sup>2</sup> )	-

Table 1.1: Conversion efficiency  $\eta$  for various solar-cell materials at the production level  $\eta_{prod}$  as well as at the R&D-level  $\eta_{R\&D}$ . Additionally, we show the total world production in 2007 to compare the market share of all approaches (from [18]).

optimal efficiency  $\eta_{max}$  is obtained for a material with a band gap of 1.3-1.5 eV and that it is about 30% (Shockley-Queisser limit) [13, 14, 15, 16]. In practice, the materials used have a band gap in the range of 1.0-1.7 eV [10]. Furthermore,  $\eta_{max}$  is much lower than the ideal thermodynamic (Carnot) efficiency  $\eta_{Carnot} = 86\%$  [16]. This illustrates that in a single-junction solar cell most of the incident photons are not used for the electron-hole generation due to their energetic (band gap) mismatch. This low efficiency can be improved by multijunction cells (tandem and triple junctions), which are serially connected solar cells with different band gaps [6, 16, 17]. The cells are arranged so that the band gap decreases successively from the top solar cell to the bottom one, and a larger part of the solar spectrum can be absorbed. Further improvement is achieved by concentrating the light with optical devices such as lenses or mirrors.

Table 1.1 shows that today almost all solar-based electricity is produced by bulk crystalline Si (c-Si) solar cells [2, 10, 17]. This can be explained by their relatively high efficiency, their proven, abundant and reliable technology, and their long lifetimes. However, c-Si has a low optical absorption coefficient, since it is an indirect band-gap material, and consequently the commonly used wafer-based modules have to be relatively thick (several  $\mu\text{m}$ ) to absorb most of the incident light. Due to the thickness of the absorber layer, light-induced electrons and holes have to move over a larger distance before reaching the contacts. Since defects can induce the recombination of these electron-hole pairs, one needs highly purified silicon with a low defect concentration. However, this in turn also makes c-Si solar cells rather expensive.

The second established solar-cell technology is based on thin-film materials, which have the following advantages [2, 8]. Most profoundly, they require less raw material, since they are typically 100 times thinner than Si-wafers. They can also be deposited

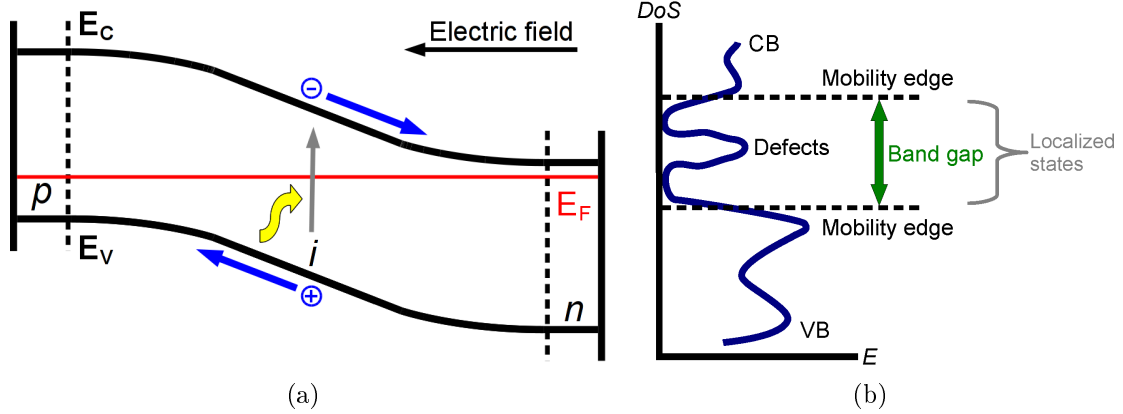


Figure 1.2: Left side: Sketch of the energetics in a *pin*-junction and the corresponding drift of light-induced electron-hole pairs. Right side: Sketch of the Density-of-States (DoS) for an amorphous semiconductor. Characteristic features are tail states as well as a continuous distribution of localized defect states in the band gap.

on cheaper substrates (glass, metal, plastic) continuously over large areas at much lower temperatures (200-500°C compared to  $\sim 1400^\circ\text{C}$  for c-Si). Furthermore, they may also contain a higher impurity concentration, are more flexible and easier to integrate into buildings, and they have a high automation and production efficiency. However, they suffer from lower conversion efficiencies, a less-developed general knowledge and technological base, and missing long-term studies of performance [2, 8]. Common features of thin-film solar cells are the usage of a transparent-conducting oxide (TCO) for the front contact as well as a reflective contact material on the back surface, and the fabrication of the devices on foreign substrates in either a substrate or superstrate configuration. In the substrate configuration, the solar cell is deposited starting from the back reflector to the top TCO-layer [10]. In the superstrate configuration, the cell is created the other way round from a TCO-based glass substrate (as e.g. convenient for integration into buildings). So far, the following materials have been used for thin-film solar cells [10, 17]: silicon (hydrogenated amorphous silicon, microcrystalline ( $\mu\text{c-Si}$ ), polycrystalline), cadmium telluride (CdTe), copper-indium (gallium-)diselenide ( $\text{CuIn(Ga)Se}_2$ ), and dye-sensitized solar cells. With respect to conversion efficiency, cadmium telluride and copper-indium (gallium-)diselenide perform best (Table 1.1) but their drawbacks are the toxicity of cadmium and the scarcity of indium and tellurium. Overall, there is no superior thin-film material and it is therefore likely that all of the options mentioned will have a share in the market.

The for thin-film solar cells relevant phases of silicon are amorphous, poly- or microcrystalline. Amorphous means the absence of any crystallinity and any long-range periodic ordering of the atoms [19]. However, the atoms are still bound covalently, and there is short-range order up to the third- or fourth-nearest neighbor. Furthermore, the average parameters for coordination (see Figure 1.3), bond length and bond angle, are

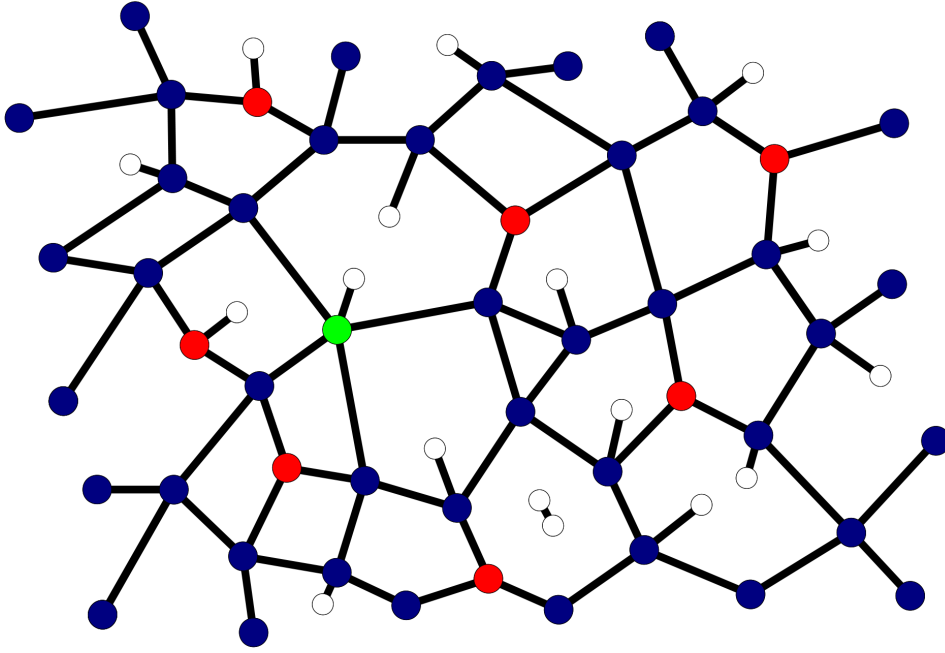


Figure 1.3: Random-network model of a-Si:H illustrating various local structural characteristics. The colors indicate coordination (white: 1 (hydrogen), red: 3-fold (dangling bond), blue: 4-fold, green: 5-fold (floating bond)).

rather similar to the crystalline phase (Section 5.3.2). Polycrystalline has many separate grains with inclined crystal planes that meet at grain boundaries (the grain size is larger than  $1\ \mu\text{m}$ ) [8, 20]. Microcrystalline silicon contains regions of crystalline silicon immersed in an amorphous matrix with grain sizes on the micro- and nanometer scale [10, 20]. In practice, the grain size depends strongly on the processing temperature  $T_p$ . The microcrystalline phase is obtained for  $T_p < 550\text{--}600^\circ\text{C}$ , and larger (polycrystalline) grains with increasing  $T_p$  (up to the melting point) [8, 20].

Hydrogenated amorphous silicon was first produced in 1969, and was soon also used for solar cells, with the first device reported in 1976 [8, 12, 21]. The hydrogen atoms play the important role of passivating defects, which are likely to occur due to the random network structure of the material (Figure 1.3). Besides that, they also passivate dopants and can cause a reconstruction of the network by breaking and removing weak Si-Si bonds in particular during growth [12]. Typical device applications of a-Si:H are solar cells, thin-film transistors in liquid-crystal displays, position and color sensors, and scanners [8, 10].

Hydrogenated a-Si thin-films are typically produced by vapor-phase deposition (CVD) such as plasma-enhanced CVD (PECVD) and hot-wire CVD (HWCVD) [8, 10, 11, 12]. The key idea is to decompose silane gas with other gases added for doping and alloying above a solid surface (substrate), on which the gas mixture is deposited. In the case of PECVD, the plasma acts as an energy source to dissociate the silane molecules (by inelastic collisions with these high-energetic electrons) at comparatively low tempera-

tures (150-350°C). Important growth parameters are pressure, substrate temperature, and electrode spacing, as well as the reduction of contaminants (e.g. oxygen, carbon, nitrogen). Lower pressure results in a uniform deposition, whereas higher pressure is required for microcrystalline growth (typical pressure range: 0.05-2 Torr) [8]. The substrate temperature  $T_d$  determines the hydrogen concentration and the optical band gap (as described below). A small electrode spacing leads to a uniform deposition, whereas a larger spacing makes it easier to maintain the plasma [8]. For HWCVD, the required energy is provided by hot metal wires (e.g. tungsten, tantalum), which are heated to temperatures larger than the melting point of silicon (>1500°C). The advantages of the latter approach are higher deposition rates, the absence of dust and ion damage, a better deposition uniformity, a wider selection of substrates and a better utilization of the process gases, but in turn, for example, it is more difficult to control the substrate temperature due to the exposure of the films to thermal radiation [10].

The global structural disorder leads to the following fundamental electronic characteristics of a-Si:H (Figure 1.2(b)) [11, 12, 19]. The optical band gap is broadened by about 0.6-0.8 eV (c-Si: 1.12 eV, hydrogenated a-Si: 1.7-2.0 eV), which in particular depends on the deposition temperature  $T_d$  (i.e. on the hydrogen content) [11]. In particular, the aforementioned lower limit corresponds to  $T_d = 300^\circ\text{C}$  (7% at.-H) and the upper limit to  $T_d = 75^\circ\text{C}$  (33% at.-H). Furthermore, a-Si:H contains a continuous distribution of localized states in the gap (tail and defect states) as illustrated in Figure 1.2(b). The 'mobility edge' separates the localized and extended states, and it is important for the transport properties of the material. The Fermi level  $E_F$  lies in the mobility gap, and conduction only occurs via thermal activation from  $E_F$  above the mobility edge, hopping in between localized states at non-zero temperatures and hopping conduction at  $E_F$ . Optical transitions can also occur via tail states, for example in the absence of defect states in the gap, electrons and holes relax first to localized states in the gap before they recombine radiatively. In contrast to the crystalline phase, the momentum needs not be conserved in electronic transitions, which leads to a much larger absorption in the amorphous phase. Specifically, whereas the absorption coefficient  $\alpha$  of c-Si is only on the order of  $100\text{ cm}^{-1}$  for photon energies larger than the band gap, a-Si:H has  $\alpha > 10^5\text{ cm}^{-1}$  correspondingly [10]. This means that a-Si:H layers of  $1\ \mu\text{m}$  are sufficient for the absorption of visible light [11].

Hydrogenated a-Si solar cells are particularly interesting because it is possible to deposit the cells on large areas (more than  $1\text{ m}^2$ ) and by a roll-to-roll manufacturing process [8, 17]. This means that the stainless-steel substrate is unrolled before each production step and rolled up again afterwards. It is appealing that in comparison to other thin-film technologies [8], a-Si:H has the largest knowledge base regarding long-term performance. Second, it is non-toxic and readily available, which makes solar-cell production consequently also rather cheap.

The major drawbacks of a-Si:H solar cells are their low conversion efficiency  $\eta$  (commercial solar modules have  $\eta = 5 - 6\%$  compared to laboratory cells with  $\eta \sim 12\%$  [10]), and -related to that- the light-induced degradation of the cells with time, the 'Staebler-Wronski effect' (SWE). This effect was discovered in 1977 and initially characterized the decrease of the photo- and the dark conductivity of a-Si:H solar cells exposed to light

for a long time [22]. Due to the SWE, a single-junction solar cell loses about 30% of its initial efficiency after 1000h of illumination [8]. The SWE is metastable and annealing at 100-250°C restores the conversion efficiency within a few minutes [12]. Similarly, one observes seasonal fluctuations in real-life a-Si:H solar cells, with a partial recovery of  $\eta$  in the summer months [17].

So far, the following strategies have been developed to reduce the SWE in single-junction solar cells [23, 24, 25]. Directly related ways are operation at elevated temperatures (60-90°C) (i.e. stimulation of the annealing process) and minimization of the thickness of the intrinsic layer (i.e. shortening of the diffusion path of the photoinduced electron-hole pairs, thus reducing their recombination rate). Chemically, one can suppress the light-induced degradation partly by using protocrystalline a-Si:H, by reducing the hydrogen concentration (and thus also the H-diffusion), or by using deuterium instead of hydrogen. On the technological side, the most powerful alternative consists in producing multijunction solar cells [8, 10]. This device structure not only has the previously mentioned advantage of more efficient light absorption, but the films can also be made thinner. Consequently, the internal electric field is larger, which increases the carrier collection rate. An optimal tandem design is a-Si:H/ $\mu$ c-Si:H (see also Table 1.1), with the amorphous cell on top, since it has the larger band gap. Alternatively, for the lower band-gap cell, alloys with germanium can be used, in particular in the combinations a-Si:H/a-SiGe:H and a-Si:H(1.8 eV)/a-SiGe:H(1.6 eV)/a-SiGe:H(1.4 eV), where the band gap of the lower two layers is adjusted by the silicon-to-germanium ratio [26]. Comparing the microcrystalline with the germanium-based approach, one finds again that both concepts have their advantages (higher efficiency of Ge-based cells, negligible light degradation in the case of  $\mu$ c-Si) and trade-offs (e.g. usage of expensive, toxic Germane source-gas, thicker  $\mu$ c-Si intrinsic layer).

The SWE is related to structural changes in the material, i.e. the formation of metastable defects. However, a full understanding of the relevant processes has not been obtained so far. One of the reasons is that the notion of a structural defect is conceptually complicated in the amorphous phase. Initially, it is only characterized by the corresponding deviation from the ideal nearest-neighbor coordination  $N = 4$  (see Figure 1.3). However, the complex local structure often makes a clear distinction between different kinds of defects (e.g. dangling bond, broken bond, floating bond) difficult. Commonly, the SWE is believed to be related to the creation of a dangling bond (db), i.e. a three-fold coordinated silicon atom with the remaining electron being unpaired. But there is no consensus on the specific defect-creation mechanism and several models exist. We now sketch only the most popular ones [23, 24]. The 'hydrogen bond-switching' model suggests that some of the photoexcited electron-hole pairs recombine at weak Si-Si bond sites. The phonon energy released subsequently breaks the bond and a back-bonded hydrogen moves in to spatially separate the two dangling bonds. In one variant of this principle, the hydrogen atom subsequently switches further bonds so that the distance between both dangling bonds is increased [11]. The 'charge-transfer' model is based on the assumption that natively charged dangling bonds are converted to neutral dangling bonds by capturing excess carriers, which leads to large structural distortions in the network. The 'H-collision' model assumes that the photoexcited carriers create mobile

hydrogen, which mostly rebinds with native dangling bonds. However, in some cases two of the hydrogen atoms collide, which then results in the formation of a metastable complex with two Si-H bonds close by and two separated dangling bonds. In the 'floating bond' model, alternatively, mobile floating bonds (5-fold coordinated silicon atoms) move around in the network and can convert to dangling bonds by bond breaking. However, all these models explain only part of the large amount of accumulated phenomenological knowledge about the SWE.

It is clear that information about the defect microstructure is crucial for a better understanding of the Staebler-Wronski effect. Experimentally, this can in particular be obtained by 'Electron paramagnetic resonance' (EPR), which probes for the local atomic structure of defects with unpaired spins, such as the silicon dangling bond. Within the EPR-Solar project, state-of-the-art experiments are carried out to measure the relevant spectral parameters with an unprecedented resolution [27, 28]. However, the structural disorder of the material leads to a broad spectral distribution, which cannot be assigned to a specific defect structure. Further insights into the relevant features can only be obtained by comparing experimental results with theoretical calculations. In this work we present a corresponding *ab initio* study of the EPR-parameters of the dangling bond in a-Si:H. The most important novelties of our approach are an accuracy which is superior to existing methods for systems with periodic boundary conditions, the unambiguous assignment of measured EPR-data to structural features of c-Si dangling bonds, the systematic study of the influence of the local defect geometry on the EPR-parameters (in particular regarding the effect of the network), and a statistical study of a sufficiently large number of a-Si:H db-models with a variety of different defect geometries.

The organization of this work is as follows. In the next chapter we will describe the EPR-technique as well as introduce the characteristic parameters. In Chapter 3, we establish the theoretical framework for the computation of these parameters. In doing so, we acknowledge that most of these topics have been already outlined extensively in the literature. For that reason, we will put our focus on only those aspects, which are of imminent importance for the understanding of this study, while referencing to some of the many well-written texts for a broader description. As mentioned, the db-defect is not a well-defined concept in an amorphous surrounding. It is therefore indispensable to start with a structurally simpler situation as, for example, provided by molecules or in a crystalline environment (Chapter 4). It gives us the possibility to establish the necessary computational parameters, and we can also conveniently quantify the achievable accuracy with respect to another theoretical approach and to experiment. Furthermore, in these crystalline environments one can systematically vary the local defect geometry, and consequently look at the effect of such changes on the EPR-parameters. In the last Chapter we turn to the computation of the EPR-parameters for the a-Si:H dangling bond. In particular, we show in which way the notion of an amorphous dangling bond deviates from its crystalline counterpart. This result is also of great importance for the understanding of the SWE, since it helps in identifying the relevant influences, which are unique to the amorphous phase. We conclude with an in-depth discussion of the remaining discrepancies between theory and experiment, and how they can be addressed by future studies.

# 2 Electron paramagnetic resonance

## 2.1 Introduction

Electron paramagnetic resonance is a key technique for the study of systems with one or more unpaired spins and a corresponding magnetic dipole moment  $\mu$  [29, 30, 31, 32]. In such a system, electromagnetic radiation can induce dipole transitions, which results in an absorption (EPR-)spectrum. A sketch of an experimental setup is shown in Figure 2.1. The most important parts of the apparatus are the radiation source, the resonator inside a magnetic field and the detector [31]. Typical applications of EPR are free radicals in the solid, liquid, or gaseous phase, transition-metal ions including actinide ions, systems with more than one unpaired electron (e.g. biradicals, which have two spatially well-separated unpaired electrons) or sufficiently localized point defects in solids. For the latter, EPR can be used to obtain information about the defect structure as well as some of their dynamic properties as a function of temperature [30]. Most importantly, EPR can give hints on the defect symmetry (e.g. whether it is isotropic or not) and its chemical identity.

Let us first consider the simple case of a free electron in a magnetic field aligned in  $z$ -direction ( $\mathbf{B} = B_0 \mathbf{e}_z$ ). Then the dipole energy for the two levels reads

$$E_{\pm} = -\boldsymbol{\mu} \cdot \mathbf{B} = \pm(1/2)g_e\mu_B B_0 \quad (2.1)$$

where  $g_e$  is the electronic  $g$ -factor<sup>1</sup> and  $\mu_B$  the Bohr magneton<sup>2</sup>. The absorption of a photon with energy  $E = \hbar\omega$  ( $\hbar$  ... Planck constant<sup>3</sup>,  $\omega$  ... angular frequency) promotes the electron from the lower to the higher energy state. From both equations, one obtains the following resonance condition ( $c$  ... speed of light<sup>4</sup>)

$$\hbar\omega = 2\pi\hbar c/\lambda = g_e\mu_B B_0 \quad (2.2)$$

This shows that the angular frequency of the photon is directly proportional to the magnetic field (or equivalently, the wave length  $\lambda$  is inversely proportional to  $B_0$ ). Consequently, there are two ways of inducing a transition from the lower to the upper energy level [31]. First, one can fix the frequency (usually in the microwave range) and vary the magnetic-field strength until resonance is obtained. This is cost-saving and easy to implement, since the field strength can be controlled by the current in an electromagnet.

---

<sup>1</sup> $g_e = 2.0023193043718$  (adapted from [31])

<sup>2</sup> $\mu_B = e\hbar/2m_e = 9.27400949 \times 10^{-24} \text{ JT}^{-1}$  (adapted from [31])

<sup>3</sup> $\hbar = 1.05457168 \times 10^{-34} \text{ Js}$  (adapted from [31])

<sup>4</sup> $c = 2.99792458 \times 10^8 \text{ ms}^{-1}$  (adapted from [31])

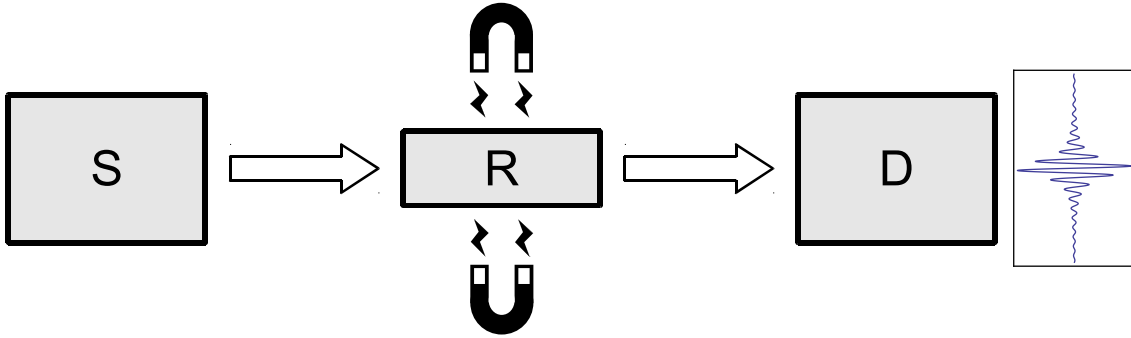


Figure 2.1: Sketch of a simple EPR-spectrometer. Radiation from a source S (usually a klystron, i.e. vacuum tube, or a Gunn oscillator) passes through a resonator R (usually a resonant cavity) containing the sample inside a magnetic field. The cavity is a rectangular metal box, and its length is on the order of one wavelength of the absorbed microwave radiation [32]. In this case, resonance occurs, which minimizes the power loss. Dipole transitions between energy levels lead to an absorption spectrum in the detector D. One usually plots the first-derivative spectrum, since it has a better resolution.

On the other hand, the variation of the frequency for a constant magnetic field is also feasible by using pulsed microwave sources and Fourier-transformation techniques. One of the advantages of this approach is that a single-pulse spectrum can be recorded on a short time scale ( $\sim 1$  ms), which makes it suitable for the study of the kinetics of a spin system.

In practice, if we extend the two-level model to  $N$  spins, the emission of photons will occur as well [30, 32]. The characteristic quantity is then the population difference  $\Delta N$ , which follows a Boltzmann distribution in thermal equilibrium. In the high-temperature approximation  $E \ll kT$ , one obtains the relation  $\Delta N = Ng\mu_B B_0 / 2kT$  where  $k$  denotes the Boltzmann factor<sup>5</sup>, and  $T$  the temperature. Therefore, the sensitivity of the spectrometer increases with the total number of spins, for larger magnetic fields and at lower temperatures. Due to the proportionality of the magnetic field and the frequency (2.2), we would now suspect that the sensitivity improves with larger frequencies as well. But in this case, the corresponding waveguides become smaller, which means that the samples have to be smaller too. Consequently, they also contain fewer detectable spins  $N$ , and this parameter is usually the more important one. Besides that, several aspects restrict the used frequency range to the microwave region [31]. For example, in the high-frequency regime, it is difficult to produce sufficiently homogeneous magnetic fields and it is expensive to shrink the microwave components. On the other hand, in a real material system, not all of the EPR-detectable mechanisms are field-dependent (i.e. frequency-dependent). Consequently, it is beneficial to measure some parameters at low fields whereas others at high fields as e.g. done in the EPR-Solar project [27, 28]. An overall good compromise is the 'X'-band, which corresponds to an operating frequency

<sup>5</sup> $k = 1.3806505 \times 10^{-23} \text{ JK}^{-1}$  (adapted from [31])

Band Label	Frequency $f = \omega/2\pi$ (GHz)	Wavelength $\lambda$ (cm)	Field $B_0$ (mT)
L	1.5	20	54
S	3.0	10	110
C	6.0	5	220
X	9.5	3	340
K	23	1	820
Q	36	0.8	1300
V	50	0.6	1800
W	95	0.3	3400

Table 2.1: Typical microwave frequencies used in EPR-experiments (adapted from [31])

of about 10 GHz (further frequency bands are listed in Table 2.1). As a rule-of-thumb, one can then detect about  $10^{12}$  spins at room temperature [32].

Interesting information from the EPR-spectrum results from the coupling of the unpaired electron spin to the magnetic environment. First, the electromagnetic fields of other electrons and nuclei give rise to local magnetic fields, which add to the applied magnetic field, thus shifting the  $g$ -value from its free-electron value [31]. These fields can be either induced by  $\mathbf{B}$  (i.e. magnitude- and orientation-dependent) or permanent (only orientation-dependent). Most notably, they are anisotropic. In this general case, the  $g$ -factor becomes a  $3 \times 3$  matrix, which is most conveniently described by its eigensystem consisting of 3 eigenvalues with corresponding principle axis. For an isotropic system all eigenvalues coincide. Uniaxial symmetry means that there is a linear rotational symmetry (at least three-fold) about a unique axis. In this case, two of the eigenvalues are the same. The most general situation, i.e. that all principal values are different, is referred to as rhombic. Overall, the anisotropy of the  $g$ -tensor reflects the local symmetry of a point defect. Furthermore, if the  $g$ -factor is sufficiently distinctive, one can identify the paramagnetic species by the line position in the spectrum.

The spin of the unpaired electron (or hole) also interacts with neighboring nuclear dipole moments  $I$ , resulting in the so-called hyperfine splitting. Due to this coupling,  $2nI + 1$  ( $n \dots$  number of equivalent nuclei) equally spaced lines appear in the spectrum, which consequently gives information on the specific isotope [30]. The intensities are characterized by a Pascal triangle<sup>6</sup> for  $I = 1/2$  (in general by a binomial series). Thus the largest intensity is observed either as a single, central peak or as two equal, symmetric peaks respectively. The hyperfine interaction is commonly also orientation-dependent, i.e. it is characterized by a  $3 \times 3$ -matrix and it can be decomposed in an isotropic part (independent of the field-orientation) and an anisotropic contribution. The interaction with the lattice surrounding (superhyperfine interaction) is usually smaller but can be useful to determine the site of the impurity as well as several further structural details. However, in solids, these interactions are rarely resolved due to the inhomogeneous line width, which arises from the superposition of all homogeneous EPR-lines of the surrounding nuclei.

<sup>6</sup>The intensity ratio is therefore 1, 1:1, 1:2:1, 1:3:3:1, 1:4:6:4:1, etc. for increasing  $N$ .

A further important characteristic is that the line shape depends upon the broadening mechanism. A Lorentzian line shape is caused by a homogeneous broadening mechanism, which means that all dipoles are subjected to the same static and time-averaged magnetic fields but different instantaneous magnetic fields [29, 31, 32]. This is the case for systems with no hyperfine broadening, low concentrations of paramagnetic centers (e.g. amorphous silicon with a natural abundance of  $^{17}\text{Si}$  of 4.68% [28]) and dynamic averaging (e.g. by spin exchange in liquid solutions). An inhomogeneous broadening is caused by small differences in the local magnetic field, and it can be described by a Gaussian. This can be due to the already mentioned unresolved superhyperfine interaction, an inhomogeneous external magnetic field, anisotropic interactions in randomly oriented systems in the solid state and dipolar couplings with other paramagnetic centers.

The spectral lines of a time-averaged response (e.g. paramagnetic species in solutions) are narrower than those of a space-averaged one (e.g. powder-spectra) [31]. In the latter case, the EPR-signal is an envelope of all orientation-dependent resonance positions of all centers. The homogeneously broadened line width can be heuristically reasoned by the energy-time uncertainty relation  $\Delta E \cdot \tau \geq \hbar$  where  $\Delta E$  is the uncertainty of the energy level and  $\tau$  the lifetime of the state [29, 30, 31, 33]. Thus a long lifetime corresponds to a small  $\Delta E$  with a narrow line width, and a short lifetime to a large one. Physically,  $\tau$  is the spin-lattice relaxation time  $T_1$ . This is the characteristic time for the coupling of the spin system to the surrounding by electron-phonon interactions. These couplings stabilize the population difference, which would otherwise gradually vanish due to saturation. Consequently, a long  $T_1$  also means that the system is only weakly coupled to the environment. Several different phonon mechanisms contribute to  $T_1$  (e.g. direct absorption/emission of a phonon, phonon scattering, etc.) in dependence of the temperature and the magnetic-field strength. Overall,  $T_1$  becomes larger for lower temperatures. Another important adiabatic coupling mechanism is the dephasing of the electron spins, which results in a further broadening of the EPR-lines. It is characterized by a separate relaxation time  $T_2$ , which is in solids usually much smaller as  $T_1$ .

Analogously to the dipole transitions of unpaired electron spins, it is possible to induce resonant transitions between energy levels of nuclear dipoles [30, 31, 33, 34]. The occurrence of such a transition requires a nonzero nuclear-spin quantum number ( $I \neq 0$ ), which excludes all isotopic nucleus with an even number of protons and an even number of neutrons (e.g.  $^{12}\text{C}$ ,  $^{16}\text{O}$ ). However, as for EPR, for these elements, suitable isotopes (e.g.  $^{13}\text{C}$ ,  $^{17}\text{O}$ ) can be detected. One can also derive a similar resonance condition as for the unpaired electron (in the style of Equation (2.2)), but due to the smaller level splitting, the (usually pulsed) electromagnetic fields are now typically in the radio frequency-range (10 MHz to 1 GHz). One advantage of this 'nuclear paramagnetic resonance' (NMR) technique is that the number of superhyperfine lines is significantly reduced. For comparison, for an electron spin-1/2 defect coupled to  $N$  nuclei, one observes  $2^N$  superhyperfine lines in the EPR-spectrum but only 2 lines in the corresponding NMR-spectrum (neglecting further small splittings due to the nuclear quadrupole interaction). But the downside of NMR is that it is not sensitive enough and therefore one needs a significantly larger number of nuclei (on the order of  $10^{19}$ ). One way to overcome all these problems is to use a technique called 'electron nuclear double resonance'

(ENDOR) [30, 31, 32]. It works by partially saturating an EPR-transition for a fixed field while simultaneously sweeping the NMR-frequency through nuclear-spin transitions until resonance with an appropriate NMR-transition occurs. Whenever this happens, one observes an increase in the intensity of the saturated EPR-transition, thus basically mapping the NMR-transition to a change in the EPR-spectrum. With this method, one obtains a gain in sensitivity on the order of  $10^3$ - $10^4$  compared to conventional NMR.

Overall, EPR and ENDOR yield information on the symmetry of the defect ( $g$ -tensor) and on the shell containing the nuclei as well as the nuclear spin and the number of interacting nuclei (hyperfine interaction) [30]. Further structural insights are obtained from the superhyperfine interaction, when it can be resolved. For systems with  $I > 1/2$ , ENDOR-spectra yield information on the chemical identity of the neighboring nuclei (magnitude of the nuclear  $g$ -value for each neighboring nuclei) as well as the charge state of the defect (by knowledge of the electric fields around the defect as derived from the quadrupole interaction of neighboring nuclei with local electric-field gradients).

## 2.2 EPR-parameters

### 2.2.1 Overview

We now turn to the formal description of the relevant processes which affect the EPR spectrum [30]. First, for conventional EPR, it is sufficient to consider only the electronic ground state, since the energy difference between the ground and excited states of the defect system (on the order of eV) is significantly higher than the one between the dipole transitions (in the range of  $\mu\text{eV}$ - $\text{meV}$ ). Furthermore, one introduces an effective spin ( $S_{\text{eff}} = S$ ) to simplify the complex coupling between the actual spin, the orbital momenta and the magnetic field. It uses the same algebraic concepts as the conventional spin (i.e. Pauli matrices), even though it differs from the actual spin in particular if there are significant orbital contributions to the total angular momentum. In the absence of a zero-field splitting and  $S > 1/2$ , the defect ground state has a  $(2S + 1)$ -fold degeneracy [30, 35], and the Hamiltonian characterizing the coupling to a single nucleus reads ( $g_n$  ... nuclear  $g$ -factor,  $\mu_n$  ... nuclear magneton<sup>7</sup>)

$$\mathcal{H}(\mathbf{r}) \equiv \mathcal{H} = \mathcal{H}^Z + \mathcal{H}^{FS} + \mathcal{H}^{HF} + \mathcal{H}^{NZ} + \mathcal{H}^Q \quad (2.3)$$

$$\mathcal{H}^Z = \mu_B \mathbf{B}^T \cdot \mathbf{g} \cdot \mathbf{S} \quad \dots \text{electron Zeeman interaction} \quad (2.4)$$

$$\mathcal{H}^{FS} = \mathbf{S}^T \cdot \mathbf{D} \cdot \mathbf{S} \quad \dots \text{fine-structure interaction} \quad (2.5)$$

$$\mathcal{H}^{HF} = \mathbf{S}^T \cdot \mathbf{A} \cdot \mathbf{I} \quad \dots \text{hyperfine interaction} \quad (2.6)$$

$$\mathcal{H}^{NZ} = -\mu_n \mathbf{B}^T \cdot \mathbf{g}_n \cdot \mathbf{I} \quad \dots \text{nuclear Zeeman interaction} \quad (2.7)$$

$$\mathcal{H}^Q = \mathbf{I}^T \cdot \mathbf{P} \cdot \mathbf{I} \quad \dots \text{nuclear quadrupole interaction} \quad (2.8)$$

---

<sup>7</sup> $\mu_n = e\hbar/2m_p = (m_e/m_p)\mu_B \sim \mu_B/1836$  (adapted from [30])

where  $\mathbf{g}$ ,  $\mathbf{D}$  (fine-structure tensor),  $\mathbf{A}$  and  $\mathbf{P}$  (nuclear quadrupole coupling tensor) are symmetrical, three-dimensional matrices, which can be diagonalized and are characterized by their principal values and eigenvectors. Commonly, one sorts the eigenvalues by  $g_X \geq g_Y \geq g_Z$ ,  $D_Z > D_X \geq D_Y$ , and  $A_Z > A_Y \geq A_X$  respectively. The matrix character of  $\mathbf{P}$  is denoted by an asymmetry parameter, which quantifies the deviation from uniaxial symmetry [31]. In experiments, it is easier to obtain the relative signs for the matrix elements (e.g.  $g_{ij}$ ) than the overall one (e.g.  $\mathbf{g}$ ) [31]. From the above equations, we see that  $\mathcal{H}^Z$  depends on the magnetic field but not  $\mathcal{H}^{HF}$ . This characteristic is exploited within the EPR-Solar project to resolve both EPR-tensors at a higher accuracy [27, 28]. In the presence of  $g$ -strain (broadening of the  $g$ -values in a frozen solution or powder spectrum [32]), it is better to obtain the hyperfine tensor at low magnetic fields and corresponding frequencies (S- and X-band), whereas the  $g$ -tensor is measured at high frequencies (Q- and W-band).

The fine-structure and nuclear quadrupole interaction occurs in spin systems with  $S > 1/2$ . The fine-structure coupling originates from the influence of the electrical crystal field felt by the spins through the spin-orbit interaction as well as the magnetic dipole-dipole interaction between the unpaired electrons [30]. Since this interaction does not depend on the magnetic field, it is also called 'zero-field splitting'. However, EPR-relevant splittings have to be on the order of the microwave energy ( $1 \text{ cm}^{-1}$ ), and depend on the defect symmetry, the spin and on the relative energy difference with respect to the Zeeman interaction. The  $\mathbf{D}$ -tensor is traceless, since it only describes a non-detectable shift of the ground-state multiplet energy. Even though the effect of this coupling can be non-trivial, it still yields useful information on the spin multiplicity and thus often also on the charge state of the defect as well as the symmetry of the defect wavefunction. The nuclear quadrupole interaction is the analogue to the fine-structure splitting for the nuclear spin  $\mathbf{I}$  [30, 31]. It denotes the coupling between the nuclear quadrupole moment (occurring for a non-spherical charge distribution in the nucleus) with the electric-field gradient of the local electron distribution (e.g. charged defect, low-symmetry lattice). In general, there is a competition to align the nuclear spin according to the local electric-field gradient, the local magnetic field caused by the unpaired electron(s) and the externally applied field. The nuclear quadrupole tensor can also be measured by EPR, and it yields very detailed information about the electron distribution close to the nucleus.

## 2.2.2 The electron Zeeman interaction

Let us start with the relation of the  $g$ -tensor to the defect symmetry [31]. The Zeeman interaction is independent of the orientation of the magnetic field in an isotropic medium. In this case, the  $g$ -tensor is actually a scalar, and the Hamiltonian (2.4) reads  $\mathcal{H} = g\mu_B(B_x S_x + B_y S_y + B_z S_z)$ . For uniaxial (i.e. tetragonal) symmetry, there are two components of the  $g$ -tensor, a parallel- ( $g_{\parallel}$ ) and a normal ( $g_{\perp}$ ) component with respect to the symmetry axis ( $g_{xx} = g_{yy} = g_{\perp}$ ,  $g_{zz} = g_{\parallel}$ ). For the general case of rhombic symmetry, let us first consider the dipole energy (2.2) again, which follows from the expectation value of Equation (2.4). The Hamiltonian can be interpreted as an interaction between

the spin and an effective magnetic field defined by  $\mathbf{B}_{eff}^T = \mathbf{B}^T \cdot \mathbf{g}/g_e$ . The magnitude of this field is given by ( $\mathbf{n} = \mathbf{B}/B_0$ )

$$\begin{aligned} B_{eff} &= [(\mathbf{g}^T \cdot \mathbf{B})^T \cdot (\mathbf{g}^T \cdot \mathbf{B})]^{1/2}/g_e = [\mathbf{B}^T \cdot \mathbf{g} \cdot \mathbf{g}^T \cdot \mathbf{B}]^{1/2}/g_e \\ &= \underbrace{\{\mathbf{n}^T \cdot (\mathbf{g} \cdot \mathbf{g}^T) \cdot \mathbf{n}\}^{1/2}/g_e}_g \mathbf{B} = gB_0 \end{aligned}$$

Consequently, for a spin-1/2 system, the energy values read  $E_{\pm} = \pm(1/2)g\mu_B B_0$  where the  $g$ -factor is defined by

$$g \equiv g(\mathbf{n}) = [\mathbf{n}^T \cdot (\mathbf{g} \cdot \mathbf{g}^T) \cdot \mathbf{n}]^{1/2}/g_e \quad (2.9)$$

Thus the  $g$ -factor only depends on the direction of the magnetic field, and it is positive for systems, which do not deviate significantly from  $g_e$  [31]. The dipole-transition energy  $\Delta E = E_+ - E_-$  follows from the experimental determination of the  $g$ -factor and depends consequently on the orientation of  $\mathbf{B}$ . Furthermore, it is evident that the product  $\mathbf{g} \cdot \mathbf{g}^T \equiv \mathbf{g}\mathbf{g}$  is the actually relevant quantity. In fact, due to the asymmetry of the matrix elements (as well as their relative signs), it is in general not possible to obtain  $\mathbf{g}$  from  $\mathbf{g}\mathbf{g}$ , since its principle system is non-orthogonal and does not coincide with  $\mathbf{g}\mathbf{g}$  anymore. Strictly speaking, in such low-symmetry systems (monoclinic, triclinic symmetry)  $\mathbf{g}$  (as well as  $\mathbf{A}$ ) is a matrix but not a tensor [36, 37]. In contrast,  $\mathbf{g}\mathbf{g}$  and  $\mathbf{A} \cdot \mathbf{A}^T \equiv \mathbf{A}\mathbf{A}$  are always tensors of rank 2.

For the formal discussion of the  $g$ -shift, let us consider a free atom with zero nuclear spin. The total magnetic-moment operator then reads  $\boldsymbol{\mu}(\mathbf{r}) = -\mu_B(\mathbf{L} + g_e\mathbf{S})$ , where  $\mathbf{L}$  is the total electronic orbital angular-momentum operator for the ground-state configuration of the atom. Furthermore, we have to take the spin-orbit interaction into account, which characterizes the interaction between the magnetic field due to the electric field of the proton and the dipole moment of the electron [38, 39]. The basic idea can already be understood in a simple classical picture of hydrogen. In this system, the electron orbits the proton, and the proton is seen as a current in the electron's rest frame, which thus gives rise to a magnetic field in accordance with the Biot-Savart law<sup>8</sup>. All together, we arrive at the following Hamiltonian [31]

$$\mathcal{H} = \mathcal{H}^Z + \mathcal{H}^{SO} = \mu_B \mathbf{B}^T \cdot (\mathbf{L} + g_e \mathbf{S}) + \lambda \mathbf{L}^T \cdot \mathbf{S}$$

In this equation,  $\lambda$  stands for the spin-orbit constant, which depends on the chemical element. From second-order perturbation theory, one can now derive for an orbitally non-degenerate ground state,  $\mathcal{H}^{FS}$  (2.5) as well as  $\mathcal{H}^Z$  (2.4) with the following expression for the  $g$ -tensor

---

<sup>8</sup>To see that the spin-orbit coupling is essentially also a dipole-energy term, let us sketch how it is derived for hydrogen [39]. The magnetic field in the electron's rest frame reads  $\mathbf{B} = const \cdot (\mathbf{v} \times (-\mathbf{r})) = const \cdot \mathbf{l}$ . For the dipole-energy term then follows ( $\boldsymbol{\mu}_s = \mathbf{s}$ )  $E = -\boldsymbol{\mu}_s \cdot \mathbf{B} = const \cdot (\mathbf{s} \cdot \mathbf{l})$ . Notably, the relativistic transformation back into the rest frame of the nucleus yields the well-known factor 1/2 due to the Thomas precession of the electron.

$$\mathbf{g} = g_e \mathbf{1} - 2\lambda \sum_{n \neq G} \frac{\langle G, m_S | \mathbf{L} | n, m_S \rangle \langle n, m_S | \mathbf{L} | G, m_S \rangle}{E_n^{(0)} - E_G^{(0)}} \quad (2.10)$$

where  $G$ ,  $n$  denotes the spatial wavefunctions of the ground and excited states respectively, and  $m_S$  stands for the spin state. This expression illustrates that the  $g$ -shift originates from the orbital angular momentum from excited states [30, 31]. As can be seen, the shift depends on the spin-orbit constant (the larger it is, the larger the deviation from  $g_e$ ) and on the difference of the energy splitting between the ground and excited states (the smaller they are, the larger the deviation). Overall, we can distinguish between [30]

- $\Delta g \approx 10^{-5} - 10^{-2}$ : typical for defects with a weak spin-orbit coupling ( $\lambda \approx 1 - 100 \text{ cm}^{-1}$ ) in a strong crystal field. This applies for example to light impurity atoms in ionic crystals and defects with an  $s$ -ground state, which in principle do not have a spin-orbit coupling at all.
- $\Delta g \approx 10^{-2} - \text{a few } 10^{-1}$ : typical for transition-metal ions with a  $3d^n$ -configuration ( $\lambda \approx 10^2 - 10^3 \text{ cm}^{-1}$ ) in a strong crystal field (e.g. ionic crystals)
- $\Delta g \approx 1$ : the concept of a  $g$ -shift is no longer applicable. This is for example the case for rare-earth ions with a  $4f^n$ -orbital configuration

The following two aspects affect the sign of the  $g$ -shift [30, 32]. First, the spin-orbit constant is typically positive for systems with a less than half-filled valence shell (negative  $g$ -shift), and negative otherwise (positive  $g$ -shift). Furthermore, the coupling to filled shells gives a positive contribution to  $\Delta g$  (since  $E_n^{(0)} < E_G^{(0)}$ ), whereas the coupling to empty shells gives a negative one.

### 2.2.3 The hyperfine interaction

The hyperfine interaction characterizes the interaction between the spin of the unpaired electron with the nuclear magnetic moment [29]. This gives rise to dipole transitions, which can occur between levels fulfilling the optical selection rules  $\Delta m_S = \pm 1$ ,  $\Delta m_I = 0$  for the electron- and nuclear-spin quantum number respectively. A simple example for the effect of the hyperfine coupling in an EPR-spectrum is given in Figure (2.2). In the case of NMR-transitions, the selection rules are actually just the opposite, i.e.  $\Delta m_S = 0$ ,  $\Delta m_I = \pm 1$ .

In analogy to  $\mathbf{g}\mathbf{g}$ , one can derive a symmetric matrix for the hyperfine tensor in Equation (2.6) [30, 31]. Experimentally, one can then obtain the magnitude of the elements from the square root of the principal values of the  $\mathbf{A}\mathbf{A}$ -tensor. The relative signs of the principal values can be measured for large magnetic fields from the nuclear Zeeman interaction. Besides that, it is also common use to decompose the  $\mathbf{A}$ -tensor into its isotropic and anisotropic parts, hence  $\mathbf{A} = a\mathbf{1} + \mathbf{T}$  where  $\mathbf{T}$  denotes a traceless, symmetric matrix. Formally, the  $\mathbf{A}$ -tensor can also be described by the following set of hyperfine parameters

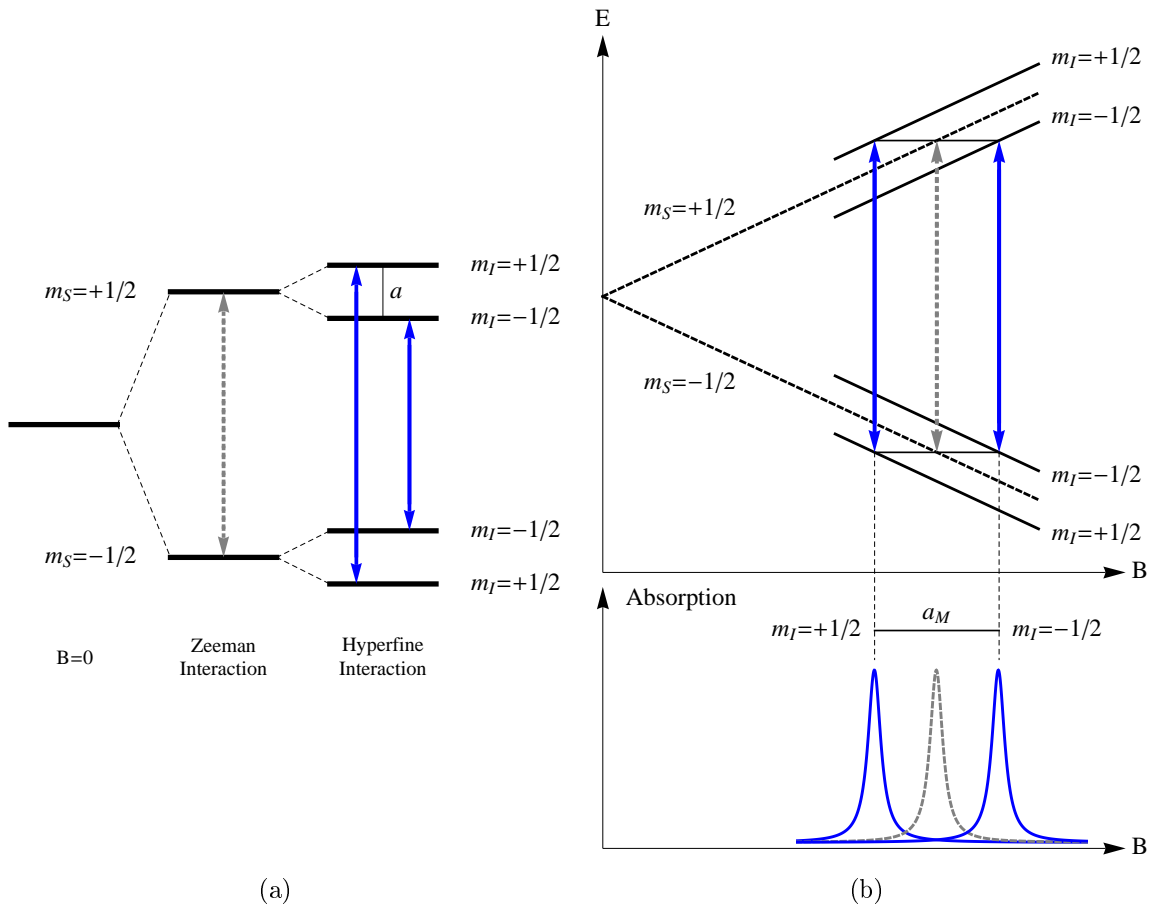


Figure 2.2: Illustration of the two most important coupling mechanisms of an electron spin ( $S = 1/2$ ) to a nucleus ( $I = 1/2$ ). (a): Level diagram for sufficiently high constant magnetic fields. Whereas the coupling of the electron spin to the magnetic field gives rise to a single transition (dashed line), there are two possible transitions (blue lines) due to the coupling between electron and nuclear spin. Both transitions fulfill the optical selection rules  $\Delta m_S = \pm 1$ ,  $\Delta m_I = 0$ . The illustrated ordering assumes that the triplet state lies above the singlet state. Notably, it cannot be distinguished from the other case in the EPR-spectrum. The isotropic hyperfine parameter  $a$  characterizes in first order the spacing between the nuclear spin states. (b): Level diagram at constant microwave frequency as a function of applied magnetic field. Absorption occurs, when  $B$  matches the resonance frequency. The  $a_M$ -parameter (in magnetic-field values) is proportional to the spacing between the resonant field values of both transitions. (concept adapted from [30, 31])

$$a = \text{tr}(\mathbf{A})/3 \quad (2.11)$$

$$= (A_X + A_Y + A_Z)/3 \quad \dots \text{Fermi contact interaction} \quad (2.12)$$

$$b = [A_Z - (A_X + A_Y)/2]/3 \quad \dots \text{Uniaxiality parameter} \quad (2.13)$$

$$c = (|A_Y| - |A_X|)/2 \quad \dots \text{Asymmetry (rhombicity) parameter} \quad (2.14)$$

First, note that  $a$  is essentially the trace of the  $A$ -matrix, and it can be therefore directly obtained from the  $A$ -tensor without diagonalization. Furthermore, the parameters reflect the symmetry of the  $A$ -tensor [30, 31]. In the case of cubic symmetry ( $A_X = A_Y = A_Z$ ,  $b$  and  $c$  are zero, thus these parameters truly quantify the deviation from this symmetry. On the other hand, when the two smaller eigenvalues  $A_X$ ,  $A_Y$  coincide (uniaxial symmetry),  $c$  vanishes, which illustrates that this parameter indeed characterizes the deviation from this kind of symmetry. For uniaxial symmetry, one can also separate the eigenvalues into a normal and a parallel field-component. They are related to the hyperfine parameters by  $A_{\parallel} = a + 2b$ ,  $A_{\perp} = a - b$ . Since uniaxial symmetry is also the most important case, we mention the corresponding angular dependence of the  $AA$ -tensor, which reads  $A^2(\theta) = A_{\parallel}^2 \cos^2(\theta) + A_{\perp}^2 \sin^2(\theta)$  with  $\theta$  being the angle between the symmetry axis and the magnetic field. Note that a similar relation also holds for a uniaxial  $g$ -tensor. Finally, the hyperfine parameters have the SI-units of energy (Joule), but since the energies are small, they are usually measured in frequency (MHz) or wavenumber units ( $10^{-4}\text{cm}^{-1}$ ) [30, 32]. As indicated in Figure (2.2), the isotropic coupling constant is related to the spacing between the resonance fields of both transitions. For that reason, one also uses magnetic-field units, hence  $a_M = a/g_e\mu_B$  with  $a_M$  measured in Gauss or millitesla<sup>9</sup>.

The sign of  $a$  determines the order of the zero-field levels, and it is related to the alignment of the nuclear and electron magnetic moment [31]. For example, for hydrogen, it is positive, when the triplet state lies above the singlet state and negative in the other case. Both situations yield the same EPR-spectrum, even though one could in principle distinguish them by NMR (i.e. at sufficiently low magnetic fields and temperatures). It is much easier to obtain the relative sign between the hyperfine parameters  $a$  and  $b$ , which consequently should also be checked for in theoretical calculations.

Formally, the isotropic hyperfine interaction is defined by the Hamiltonian [31]

$$\mathcal{H}^{HF} = \frac{2\mu_0}{3} g_n g \mu_n \mu_B |\psi(\mathbf{R} = 0)|^2 \mathbf{S}^T \cdot \mathbf{I}$$

where  $\psi(\mathbf{r})$  stands for the one-particle wavefunction at the atomic site  $\mathbf{R}$ . This means that it is proportional to the probability of presence at the position of the nucleus. Since only  $s$ -wavefunctions are nodeless at  $\mathbf{R}$ , this implies that the  $a$ -parameter arises from only such contributions and thus effectively probes for the  $s$ -like character of a system. As discussed below, experimentally one frequently estimates the  $s$ -character of the unpaired

---

<sup>9</sup>Useful conversion factors:  $a(\text{MHz}) = 2.8025(g/g_e)a(\text{G})$ ,  $a(10^{-4}\text{cm}^{-1}) = 0.93480(g/g_e)a(\text{G})$ ,  $1 \text{ mT} = 10 \text{ G}$  (adapted from [32])

electron by considering the ratio of the experimental and theoretical  $a$ -value, where the latter is computed for atomic wavefunctions [29]. In general,  $|\psi(\mathbf{R} = 0)|^2$  has to be replaced by the spin density, which is denoted by the difference between spin-up and spin-down electrons, i.e.  $m(\mathbf{r}) = n_\uparrow(\mathbf{r}) - n_\downarrow(\mathbf{r})$ . From Equation (2.6) and the decomposition of the  $A$ -tensor, we see that the isotropic hyperfine constant can also be written in the non-relativistic limit as

$$a = \frac{2\mu_0}{3} g_n g \mu_n \mu_B m(\mathbf{R}) \quad (2.15)$$

In multi-electron systems, the outer electrons cause a spin-alignment of the inner electrons (parallel/antiparallel), which is referred to as 'core polarization'. In this situation, the net electron-spin polarization determines the sign of  $a$ . The effect of core polarization is particularly important for transition-metal defects [30]. Finally, as we will discuss in the next chapter, a scalar-relativistic approach causes a modification of Equation (2.15), since the relativistic  $s$ -wavefunctions diverges at  $\mathbf{R} = 0$ .

From Equation (2.15) we also see that the  $a$ -parameter depends on the nuclear  $g_n$ -factor. This means that two magnetic isotopes of the same chemical element have two distinctive isotropic hyperfine couplings (with the same ratio as the corresponding  $g_n$ -factors). Additionally, their line intensities are proportional to the isotope abundances. Together, one can use these findings to identify the impurity (e.g. Te in silicon [30]).

The anisotropic dipole interaction is described by the following Hamiltonian [30, 31]

$$\mathcal{H}^{dip}(r) = \frac{\mu_0}{4\pi} g_n g \mu_n \mu_B \left[ \frac{3(\mathbf{I}^T \cdot \mathbf{r})(\mathbf{S}^T \cdot \mathbf{r})}{r^5} - \frac{\mathbf{S}^T \cdot \mathbf{I}}{r^3} \right]$$

where  $\mathbf{r}$  is the distance vector between the electron and nucleus. From the corresponding expectation value, one can derive an explicit expression for the anisotropic tensor

$$\mathbf{T} = \frac{\mu_0}{4\pi} g_n g \mu_n \mu_B \int m(\mathbf{r}) \frac{3\mathbf{r} \otimes \mathbf{r} - r^2 \mathbf{1}}{r^5} d^3\mathbf{r} \quad (2.16)$$

An important situation is again the case of uniaxial symmetry [31, 32]. When the electron is in a pure  $p$ -orbital centered on the interacting nucleus and the magnetic field is aligned along  $\mathbf{z}$ , one can write the dipolar coupling as

$$\mathcal{H}^{dip} = \frac{\mu_0}{4\pi} g_n g \mu_n \mu_B \left\langle \frac{3 \cos^2 \theta - 1}{r^3} \right\rangle S_z I_z$$

where  $\theta$  denotes the angle between  $\mathbf{z}$  and the axis of the  $p$ -orbital. Furthermore, the corresponding expression for the uniaxiality parameter  $b$  reads [40]

$$b = \frac{\mu_0}{4\pi} g_n g \mu_n \mu_B \int m(\mathbf{r}) \frac{3 \cos^2 \theta - 1}{2r^3} d^3r \quad (2.17)$$

The factor  $(3 \cos^2 \theta - 1)/2$  is a  $d$ -like ( $l = 2$ ) spherical harmonic. Therefore the  $b$ -parameter projects out these contributions from the spin density, thus it effectively probes in  $sp$ -bonded systems such as silicon for the  $p$ -like character of the defect orbital.

A second important application of relation (2.17) is that one can use it to estimate the distance  $R$  between the db-atom (more precisely: the center-of gravity of the spin density) and a second atom with a sufficiently small isotropic coupling [30]. When additionally, the hyperfine tensor of the second atom points towards the defect, it is reasonable to assume that there is no magnetization density at this atom. In this case, one can replace the defect by a point dipole (in the defect center), and one obtains the following classical relation [41]

$$b = g_n g \mu_n \mu_B / R^3 \Rightarrow R = \sqrt[3]{\frac{b}{g_n g \mu_n \mu_B}} \quad (2.18)$$

It is also common practice to approximate the defect wavefunction by a LCAO-model ('linear combination of atomic orbitals'), which for silicon reads [42, 43, 44, 45]

$$|\psi\rangle = \sum_i \alpha_i (\sigma_i |s\rangle + \pi_i |p\rangle) \quad (2.19)$$

where  $|s\rangle$  and  $|p\rangle$  stand for the atomic  $s$ - and  $p$ - valence states,  $i$  indexes all atoms belonging to the defect complex, and the expansion coefficients  $\alpha_i$ ,  $\sigma_i$ ,  $\pi_i$  fulfill the normalization conditions  $\sum_i \alpha_i^2 = 1$ ,  $\sigma_i^2 + \pi_i^2 = 1$ . For uniaxial symmetry and sufficiently localized defects (so that at the site  $i$  only contributions from orbitals centered on atom  $i$  itself have to be taken into account), the hyperfine parameters are given by

$$a_i = \frac{2\mu_0}{3} g_n g \mu_n \mu_B \cdot \alpha_i^2 \sigma_i^2 |\psi_s(0)|^2 \quad b_i = \frac{\mu_0}{4\pi} g_n g \mu_n \mu_B \cdot \alpha_i^2 \pi_i^2 \frac{2}{5} \langle \psi_p | r^{-3} | \psi_p \rangle$$

The quantities  $|\psi_s(0)|^2$ ,  $\langle \psi_p | r^{-3} | \psi_p \rangle$  are computed from atomic wavefunctions. Overall, when  $a$  and  $b$  are known from experiment, one can then estimate the  $s$ -character fraction  $\sigma_i^2$ , the  $p$ -character fraction  $\pi_i^2$  as well as the degree of localization  $\alpha_i^2$ . For example, for the dangling-bond defect in hydrogenated amorphous silicon, the following values have been deduced from experiment [45]:  $\alpha_0^2 = 47 - 67\%$ ,  $\sigma_0^2 = 6 - 9\%$ ,  $\pi_0^2 = 91 - 94\%$ . With respect to an ideal  $sp^3$ -hybrid<sup>10</sup>, we see that the amorphous dangling bond is more delocalized, has a smaller  $s$ - and a larger  $p$ -character [12]. With such estimates for the db-character, it is possible to make further conclusions on the bond angle of the defect atom [46]. However, this approach neglects many effects such as the spin polarization or the spin delocalization into the network. The latter can be very important as we will show later on for dangling-bond defects in crystalline and amorphous silicon.

In a complex material such as amorphous silicon, the spectral broadening is large. In this case, the already mentioned multi-frequency approach can improve the accuracy of the EPR-parameters [27, 28]. However, for the experimental determination of these quantities, it is necessary to carry out numerical simulations of the EPR-spectrum based on the spin Hamiltonian (2.3). In particular, for the hyperfine interaction this becomes difficult, since it is not possible to include all nuclei, and therefore further approximations have to be made. For example, one has to specify the line shape of the unresolved hyperfine interaction (by an empirical broadening function), or one has to assume that

---

<sup>10</sup> $\alpha^2 = 100\%$ ,  $\sigma^2 = 25\%$ ,  $\pi_0^2 = 75\%$

the  $g$ - and  $A$ -tensor are collinear to each other. Even though these simplifications are reasonable, they introduce an uncertainty in the analysis. Furthermore, due to the structural disorder in amorphous silicon, it is unclear, how the experimental values are related to the defect microstructure. Both aspects require insights from theoretical studies, and this also characterizes the fundamental motivation for our work.

## 2.3 Summary

In this chapter, we have discussed the EPR-technique, which can be exploited to study defects with one or more unpaired electron spins. From such experiments one gets information on the defect symmetry and the chemical identity of the defect. The most important couplings of the EPR-spectrum are the Zeeman interaction (interaction of the unpaired electron spin with the external magnetic field) and the hyperfine interaction (interaction of the unpaired spin with the nuclear spin of atoms of the defect surrounding). Both can be expressed as  $3 \times 3$ -matrices, and can be therefore upon diagonalization characterized by three principal values with corresponding eigenvectors, or alternatively by parameters that reflect the symmetry of the matrix.

# 3 Theoretical modelling of EPR-parameters

## 3.1 Density-functional theory

### 3.1.1 Fundamental concepts

For the theoretical computation of the EPR-parameters, we have to specify the underlying description of paramagnetic defects in solids. This in turn brings us to the most general starting point, the formal description of interacting electrons and nuclei. The corresponding Hamiltonian reads [47, 48]

$$\mathcal{H} = T_e + T_I + V_{ee} + V_{eI} + V_{II} \quad (3.1)$$

with the following terms (in Hartree atomic units, i.e.  $\hbar = m_e = e = 4\pi/\epsilon_0 = 1$ )

- $T_e, T_I$ : kinetic energies of the electrons and nuclei ( $T_{e/I} = -\frac{1}{2m} \sum_i \nabla_i^2$  where  $m = 1$  for electrons and  $m = m_I$  for protons)
- $V_{ee}$ : Coulomb interaction between electrons ( $V_{ee} = \frac{1}{2} \sum_{i \neq j} \frac{1}{|\mathbf{r}_i - \mathbf{r}_j|}$ )
- $V_{eI}$ : Coulomb interaction between electrons and nuclei ( $V_{eI} = -\frac{1}{2} \sum_{i,I} \frac{Z_I}{|\mathbf{r}_i - \mathbf{R}_I|}$ )
- $V_{II}$ : Coulomb interaction between nuclei ( $V_{II} = \frac{1}{2} \sum_{I \neq J} \frac{Z_I Z_J}{|\mathbf{R}_I - \mathbf{R}_J|}$ )

In these equations, lower-case subscripts and upper-case subscripts stand for electrons and nuclei, respectively. With this Hamiltonian at hand it is possible to state the formal eigenvalue problem, i.e. the time-independent Schrödinger equation. However, it cannot be solved directly and simplifications are required. The first step consists in neglecting the only small term in the Hamiltonian, the nuclear kinetic energy [30, 47, 48]. This 'Born-Oppenheimer' or 'adiabatic' approximation is usually physically reasonable since the time scale associated with the motion of nuclei is usually much slower than that associated with electrons<sup>1</sup>. Physically, it means that the electrons follow the motion of the nuclei instantaneously while remaining always in the same stationary state of the electronic Hamiltonian. In this case one can separate the wavefunction into a product of an electronic wavefunction  $\Psi_e(\{\mathbf{r}\})$  (in which the nuclear positions only enter as fixed

---

<sup>1</sup>Since the kinetic energy is inversely proportional to the mass, we can also see this point by considering the mass ratio  $m_I/m_e$ . Already for a single proton, it is 1836:1, hence  $m_I \gg m_e$ , and therefore  $T_I \ll T_e$  [47].

parameters) and a nuclear wavefunction. This ansatz reduces the complexity of the electronic problem, and it is reasonable as long as the electronic excitation energy  $E_e$  is sufficiently larger as the vibrational excitation energy [47]. This condition is usually fulfilled for insulators and semiconductors, since  $E_e$  is then determined by the band gap (typically on the order of a few eV). On the other hand, metals possess a continuous excitation spectrum and in this case, the adiabatic approximation is in principle only applicable with auxiliary conditions. However, for typical temperatures (between room temperature and a few thousand degrees) it is usually still valid [47].

The two key effects characterizing the many-body problem are exchange and correlation [47, 48, 49]. In a single-particle picture, the Pauli principle states that two electrons must not have the same set of quantum numbers. This implies that the many-electron wavefunction must be antisymmetric under particle exchange and two electrons of the same spin cannot be at the same position at the same time. This leads to a spatial separation of corresponding electrons, which reduces the Coulomb energy of the system by an amount called 'exchange energy'. A similar effect occurs for electrons of opposite spin, which also try to maximize their spatial separation due to Coulomb repulsion. This phenomenon is called 'correlation', and we will specify the corresponding energy contribution below.

The solution of the electronic eigenvalue problem remains difficult despite the Born-Oppenheimer approximation, and there is no universal approach for all materials and phenomena [30, 47, 48, 49, 50]. The two most accurate approaches are post-Hartree-Fock (HF) quantum chemistry and quantum Monte-Carlo methods (QMC). Within HF one writes the electronic wavefunction as a Slater determinant of single-particle spin-orbitals (each being a product of a spatial and a spin wavefunction), and subsequently looks for the single determinant that minimizes the total energy for the Hamiltonian (3.1). The HF-approach naturally includes the exchange interaction but not electron correlation. However, these (small but not necessarily unimportant) effects<sup>2</sup> can be incorporated in a post-HF method such as 'Configuration interaction' or Møller-Plesset perturbation theory [47]. In fact, correlation is often defined as the difference between the full ground-state energy (obtained with the true many-body wave function) and the total Hartree-Fock energy. Alternatively to HF, QMC uses statistical sampling techniques to directly evaluate quantum mechanical observables such as the energy [49].

Density-functional theory (DFT) provides a simpler and less expensive alternative to post-HF- and QMC-methods [30, 47, 48, 50, 51]. The key idea consists in reformulating the many-body problem in terms of the electron density. This is possible due to the Hohenberg-Kohn theorems [48]

- I) The ground-state particle density  $n_0(\mathbf{r})$  determines the external potential  $V_{ext}(\mathbf{r}) \equiv V_{ext}[n(\mathbf{r})]$  uniquely up to a constant.
- II) A universal functional for the energy  $E[n]$  in terms of the density  $n(\mathbf{r})$  can be defined and the exact ground-state energy of the system is the global minimum

---

<sup>2</sup>For example, for a nitrogen molecule, the correlation energy is only 0.5% of the total energy but 50% of the molecular binding energy [49].

value of this functional.

The external potential includes the Coulomb interaction between the electrons and the nuclei and any external field applied to the whole system. The first theorem states that all properties of the system are completely characterized by  $n_0(\mathbf{r})$ . The second one relates the total energy of the system to the density and determines the ground state. The total energy is fundamental to the formalism, since further quantities such as atomic forces<sup>3</sup> are derived from it.

For our purposes it is particularly important that these theorems can be easily extended to include an external magnetic field, which acts only on the spins but not on the orbital motion [47, 48, 51]. In this case the above statements are generalized to two kinds of density, the particle density  $n(\mathbf{r})$  and spin density  $m(\mathbf{r})$

$$n(\mathbf{r}) \xrightarrow{\text{spin}} \begin{cases} n(\mathbf{r}) = n(\mathbf{r}, \uparrow) + n(\mathbf{r}, \downarrow) \\ m(\mathbf{r}) = n(\mathbf{r}, \uparrow) - n(\mathbf{r}, \downarrow) \end{cases} \quad E[n(\mathbf{r})] \xrightarrow{\text{spin}} E[n(\mathbf{r}), m(\mathbf{r})]$$

The description by two spin densities does not work for non-collinear magnetism, which can occur e.g. due to spin-orbit coupling, and such effects can only be treated by a relativistic approach [51]. But the corresponding formalism is more complicated than spin-DFT. Alternatively also a non-relativistic current-DFT turns out to be useful. It is based explicitly on the spin density and the non-relativistic paramagnetic current-density vector.

Since the exact density-functional expressions for the electron kinetic- and exchange-correlation (XC) energies are unknown, one has to introduce approximations either by solving for the density in orbital-free (OF) DFT or by solving for a single-electron configuration in Kohn-Sham (KS) DFT. The OF-DFT approach requires only the density, which however means that the kinetic energy must be approximated in terms of  $n(\mathbf{r})$  [50, 52]. Consequently, the usage is limited to conceptually simple local situations (e.g. Thomas-Fermi approach for the free-electron gas). The key idea of KS-DFT [30, 47, 48, 50, 51] is to map the ground-state density  $n_0(\mathbf{r})$  for interacting particles to the density  $n(\mathbf{r})$  for a system of noninteracting particles (see Figure 3.1). The latter density is then expanded in terms of single-particle orbitals  $\varphi_n(\mathbf{r})$ , i.e.  $n(\mathbf{r}) = \sum_{n=1}^N |\varphi_n(\mathbf{r})|^2$ . The kinetic energy can be calculated quite accurately from  $\varphi_n(\mathbf{r})$  (except for small contributions from exchange and correlation to the many-body kinetic energy). The minimization of the corresponding total energy yields the following 'Kohn-Sham equations' ( $v_i(\mathbf{r}) \equiv v_i[n(\mathbf{r})]$ )

$$\left[ \frac{1}{2} \nabla^2 + v_{ext}(\mathbf{r}) + v_H(\mathbf{r}) + v_{xc}(\mathbf{r}) \right] \varphi_n(\mathbf{r}) = \varepsilon_n \varphi_n(\mathbf{r}) \quad (3.2)$$

where  $v_{ext}(\mathbf{r})$  is the external potential,  $v_H(\mathbf{r})$  the Hartree potential and the exchange-correlation potential  $v_{xc}(\mathbf{r}) = \delta E_{xc}[n(\mathbf{r})]/\delta n(\mathbf{r})$ . The advantage of this formulation is that the significant local terms (kinetic energy,  $v_{ext}(\mathbf{r})$ ,  $v_H(\mathbf{r})$ ) are treated exactly, and

---

<sup>3</sup>For the derivative of the energy with respect to any parameter  $\lambda$  holds  $\partial_\lambda E_n = \langle \Psi_\lambda | \partial_\lambda \mathcal{H} | \Psi_\lambda \rangle$  where  $E_n(\lambda)$  and  $\psi_n(\lambda)$  are the eigenvalues and eigenfunctions of  $H(\lambda)$  (Feynman-Hellmann theorem) [38].

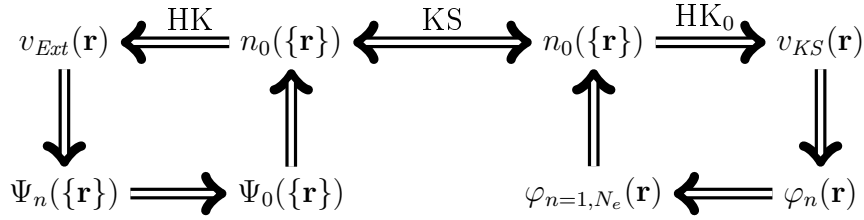


Figure 3.1: Schematic representation of the Kohn-Sham ansatz. The many-body problem in terms of the density is mapped on a system of noninteracting particles (concept adapted from [48]).

that only the exchange-correlation term must be approximated. The latter cannot be neglected but at least it is smaller compared to the other contributions. As for the Hartree-Fock orbitals, one can write the exchange part explicitly in terms of the Kohn-Sham orbitals  $\varphi_n(\mathbf{r})$ . However the same thing is in general not possible for the density. Thus the problem again consists in describing the effect of correlation.

The KS-eigenvalues do not have a true physical meaning, with the only exception of the highest occupied eigenvalue, which corresponds to the negative of the first ionization energy [48, 50, 51, 52]. But this relation only holds strictly for the exact functional. For calculations with an approximate XC-functional, the ionization energy is actually in better agreement with experiment, when it is computed by total-energy differences, i.e.  $I = E_0(N - 1) - E_0(N)$  [50]. Nevertheless, the KS-eigenvalues do provide an empirical first approximation to the actual energy levels (typically in the presence of fermionic quasi-particles and absence of strong correlations). This resemblance is exploited in band-structure calculations, for which one considers Equation (3.2) as a true physical approximation to the many-body problem. A more accurate approach is the GW-method, which is based on a set of Green's functions equations and an approximation for the electron's self-energy [53].

### 3.1.2 Practical aspects of DFT-calculations

We will now outline how density-functional theory is implemented in practice. The most important point here is that the numerical solution of the KS-equations (3.2) further broadens the methodological spectrum by a variety of different approaches. Overall the determination of the KS-DFT ground state contains the following ingredients [30, 47, 48, 51, 54, 55, 56, 57]

- *kinetic energy*: this might be either non-relativistic (Schrödinger equation), scalar-relativistic (relativistic kinetic-energy operator and other simple relativistic corrections but not spin-orbit coupling) or relativistic (Dirac equation including spin-orbit coupling).
- *external potential  $v_{ext}(\mathbf{r})$* : for the electron-nuclear interaction one has the choice in between treating all electrons equally (all-electron method) or removing the core

electrons and the Coulomb singularity from the atomic nuclei by substituting the external potential with a smooth pseudopotential around each atom.

- *exchange-correlation potential  $v_{xc}(\mathbf{r})$* : the exchange energy can be expressed in terms of the single-particle orbitals but its actual computation is rather unfeasible. On the other hand, there is no way of calculating the correlation energy at a comparable level of accuracy. Consequently the basic strategy consists in finding an approximation for the overall effect as outlined below.
- *basis set*: the expansion of the KS-orbitals requires the choice of a basis set, which can be distinguished according to the localization of the basis set [47]. Extended basis sets exploit delocalized basis functions, either floating (independent of the nuclear position) or centered at the nuclear positions. They sample all space equally and are therefore in particular useful for condensed phases such as solids or liquids. Typical representatives are plane waves (PW), floating Gaussians (which are spatially fixed) or Lagrange polynomials. On the other hand, localized basis functions are centered e.g. at the atomic positions, and are consequently most suitable for the description of molecular systems. The used basis functions can be e.g. atomic orbitals, Slater-type orbitals, or Gaussian-type orbitals. Both approaches can be combined, either in a mixed basis set (including both kind of basis functions) or by augmenting an extended or atomic-centered basis set with atomic-like wavefunctions in spherical regions around the nuclei (e.g. 'augmented plane waves' or 'linearized muffin-tin orbital method'). The choice of the basis set is correlated to the one for the external potential, since e.g. an huge number of plane waves is necessary to model the Coulomb singularity at the nuclei. Therefore within the PW-approach it becomes convenient to replace the nuclear potential by a pseudopotential.
- *self-consistency*: the KS-equations must be solved self-consistently (SCF), since the potentials depend on the density (Figure 3.2). In this scheme, one starts with a trial density and constructs the effective potential. This potential is plugged into the KS-equations, which can then be solved. From the resulting wavefunctions one can compute a new density, which is compared to the initial guess. If both agree within the predefined accuracy, one has found the solution to the problem. In the other case, one computes a new initial density (by mixing the old with the new density) and starts all over again. Many numerical concepts and parameters are connected to the SCF-cycle such as the construction of the initial density (atomic orbitals, etc.), the minimization method (steepest descent, conjugate gradient, etc.) or the density-mixing scheme (linear, etc.). Noteworthy, structural relaxation follows from the SCF-cycle by adding another outer loop, in which the atomic forces are minimized.

### *Pseudopotentials*

The *ab initio* pseudopotential (PP) approach is based on the idea that only the outer (valence) electrons participate in chemical bonding whereas the inner (core)

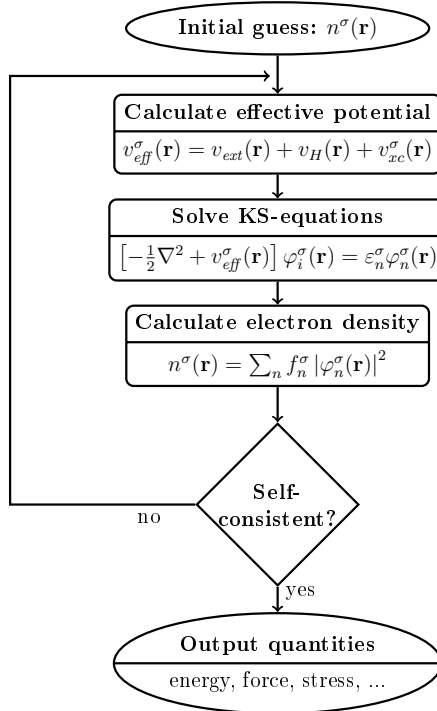


Figure 3.2: Work-flow of the SCF-solution of the KS-equations. For spin-polarized systems the loop has to be done for each spin component  $\sigma = \uparrow, \downarrow$  separately. The Fermi distribution is denoted by  $f_n^\sigma \equiv f^\sigma(\epsilon_n)$ . (adapted from [48])

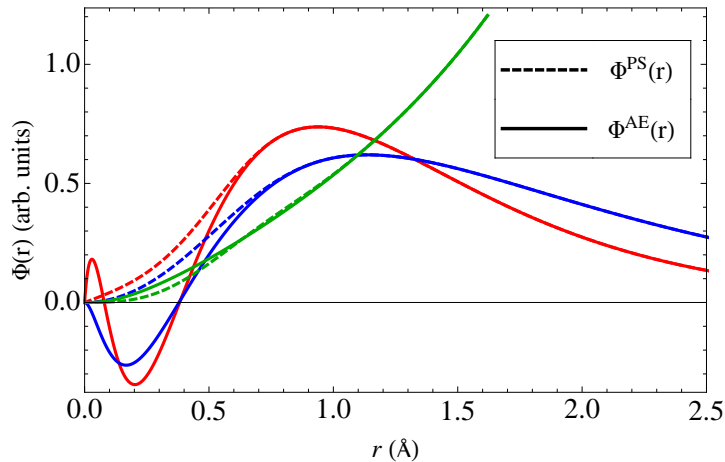


Figure 3.3: Pseudo and all-electron radial wavefunctions for a silicon potential (scalar-relativistic Hamann-type) generated with the fhi98-PP code [58]. The dashed lines show the pseudo wavefunctions and the solid lines the all-electron wavefunctions. Two features are important. First, the pseudo wavefunctions are nodeless in the core region. Secondly, they match the all-electron wavefunctions outside a cutoff-radius  $r_C$  (with  $r_C$  increasing with increasing angular-momentum component).

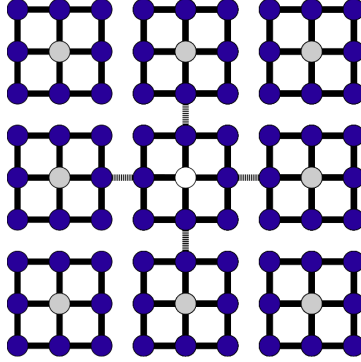


Figure 3.4: Illustration of the supercell-based point-defect model. The original defect (removed atom in the middle indicated by a white circle) is repeated throughout space (gray circles) due to periodic boundary conditions.

electrons stay in an approximately atomic-like, environment-independent configuration. Consequently, one only considers the valence electrons. The Hartree and XC-potential become functionals of the valence density  $n_v$ . The external potential is replaced by a pseudopotential  $v_{ext}^{PP}$  according to a two-step procedure [51, 58]. First, one generates an effective pseudopotential  $v_s^{PP}[n_v] = v_{ext}^{PP} + v_H[n_v] + v_{xc}[n_v]$  from an atomic calculation, so that for a suitable reference configuration, the pseudo wavefunctions are equal to the corresponding all-electron valence wavefunctions outside a cutoff radius and that their logarithmic derivatives lead to the same scattering properties. Thus the valence densities of the pseudo and the all-electron atom are the same. In the second step one subtracts the atomic valence contributions of the Hartree and exchange potential from  $v_s^{PP}[n_v]$ . This 'unscreening' is necessary to make the pseudopotential independent of the chemical environment ('transferable'), but it can be done exactly only for the Hartree potential (linear dependence in the density). There are several ways to construct pseudopotentials and many additional choices can be made. For example, pseudopotentials can be either local or nonlocal, include relativistic effects, be norm-conserving, or include non-linear core corrections. Local means that one uses the same potential for all angular-momentum components whereas a nonlocal potential is angular-dependent. One common practice is to consider only low-angular momenta as nonlocal whereas the others are treated as local (e.g. the  $d$ -component in the case of silicon). Relativistic effects become in particular important for heavier atoms from the fifth row onwards [47]. Norm-conservation requires that the norm of the true and pseudo wavefunctions is the same inside the pseudized region [47]. Finally, non-linear core corrections are important when the valence orbitals of one atom overlap with the core orbitals of other atoms as in II-VI semiconductor compounds [47]. Along with these aspects, there are a variety of parameters, that affect the quality of the pseudopotential. For instance, one has to specify the electronic configuration (most commonly the neutral atom), the states included in the valence and core respectively, the maximal nonlocal angular-momentum component, or the radius of the core region  $r_c$ . The latter parameter illustrates also an important aspect in the PP-generation, the trade-off between accuracy and hardness

of the pseudopotential. A small value for  $r_c$  results in a hard potential, but which is also more transferable from one to the other chemical environment. However, as mentioned, such a potential requires a larger number of plane waves. On the other hand, a smooth pseudopotential works with a smaller number of plane waves but it consequently also less accurately describes effects due to the core region. Overall the generation of pseudopotentials is a complex matter, and its usage has always to be tested critically. This can be done by carrying out a PP-calculation for a simple test system and then comparing it with a corresponding all-electron calculation. The latter can be accomplished by comparing the PP test-calculation with a corresponding all-electron calculation (e.g. see Subsection 4.2.2). The EPR-parameters sensitively depend on the wavefunctions in the core region. They cannot be computed directly from a pseudopotential calculation, but it is still possible to reconstruct the missing all-electron information as we will discuss below.

### *The XC-Functional*

The simplest approach is the 'local density approximation' (LDA), which takes the inhomogeneous electron gas as locally homogeneous [47]. The exchange energy is then proportional to the integral of  $(n(\mathbf{r}))^{4/3}$  over  $\mathbf{r}$ . However, even in this elementary case one cannot compute the correlation energy analytically. It is usually estimated by parameterizations of QMC-calculations for the electron gas. The resulting overall XC-functional yields in general reasonable results, even for systems that are quite different from the homogeneous electron gas [51]. This can be explained by a systematic error cancellation since LDA underestimates the correlation energy but overestimates the exchange energy at the same time<sup>4</sup>. Noteworthy, the LDA-functional can conveniently be extended to include spin polarization (LSDA). The approximation of the true electron distribution by a locally homogeneous density results in the following general trends [47]. L(S)DA-calculations overestimate the binding energy of molecules and the cohesive energy of solids. The geometric properties of systems with strong bonds (covalent, ionic, metallic) are described within a few percent in comparison to experiment. However, the over-binding problem leads in general to an underestimation of bond lengths. Similar trends are also found for the elastic constants and phonon frequencies. On the other hand, LDA fails to cancel the self-interaction in the Hartree term, which is significant for strongly localized states (e.g. electron density of atoms in the core region), and underestimates the band gap in semiconductors typically by about 30-50% [59]. In small-gap materials such as Ge the system actually becomes metallic [47].

The generalized-gradient approximation (GGA) incorporates semi-local electronic effects by including the gradient into the XC-functional. Remarkably, the main strategy here is to look for general functions  $f(n(\mathbf{r}), |\nabla n(\mathbf{r})|)$  of the density and its gradient, whereas a systematic power expansion in terms of gradients does not improve the

---

<sup>4</sup>The conceptual reason behind it is that the exchange-correlation hole  $n_{xc}^{LDA}(\mathbf{r}, \mathbf{r}')$  (characterizing the reduction of probability of an electron at  $\mathbf{r}'$  given a second one at  $\mathbf{r}$ ) obeys the sum rule  $\int n_{xc}^{LDA}(\mathbf{r}, \mathbf{r}') d^3r = -1$  [51].

accuracy compared to LDA [51]. However, these general functions can be obtained in different ways, which results in a variety of GGA-functionals. In chemistry, the typical approach consists in fitting the necessary parameters to experimental molecular data (e.g. BLYP). In contrast to that, in physics one aims at incorporating formal properties and limits (e.g. Perdew-Burke-Ernzerhof (PBE) functional [60]). The GGA-XC energy is lower than for LDA [48]. This effect is more pronounced in atoms than in condensed matter due to the more rapidly varying density, and it leads to an overall better agreement with experiment. GGA-functionals improve binding energies, atomic energies, bond parameters, the gap energy and dielectric constant (but not substantially). However, they also do not compensate satisfactorily for the self-interaction present in the Hartree term [47].

Conceptually more advanced functionals have been developed as well. For example, meta-GGAs include the kinetic-energy density (i.e. higher derivatives of the density) in the XC-functional. This improves in particular atomization energies, however, within this approach open questions remain (such as the incomplete cancellation of the self-energy [47]). Hybrid functionals incorporate some Hartree-Fock exchange into the DFT XC-functional so that the exchange-correlation energy becomes dependent on  $E_{xc}^{DFT}[n(\mathbf{r})]$ ,  $E_{xc}^{HF}[n(\mathbf{r})]$  and mixing parameters. A popular example for molecular applications is the B3LYP-functional, which is able to reproduce the geometry and binding energies at the same level as post-HF methods [47]. But the mixing parameters are obtained by fitting to molecular data, which is conceptually unsatisfactory. The HSE-functional has turned out to be quite successful for molecules and semiconductors [61]. The concept of this functional is to separate the XC-potential into short and long-range parts by an error function with a characteristic screening length  $\sim 10 \text{ \AA}$ . In the former region one mixes the PBE- with with the nonlocal Hartree-Fock exchange potential in the ratio 75/25. The long-range part is described purely by PBE, which is also used for the overall characterization of correlation. The HSE-functional improves the band gap for many materials but it is computationally expensive and there is still some arbitrariness in the choice of the mixing parameters. Besides meta-GGAs and hybrid functionals there are a number of other important approaches to the XC-Functional [48] such as SIC (self-interaction correction), LDA/GGA+U, OEP (optimized effective potential), ADA (average-density approximation) and WDA (weighted-density approximation).

#### *Plane-wave basis set*

Bloch's theorem states that we can write each electronic wavefunction in an external periodic potential  $v(\mathbf{r}) = v(\mathbf{r} + \mathbf{a}_i)$  ( $\mathbf{a}_i \dots$  unit vector) as a sum of plane waves [47]

$$\psi_{\mathbf{k}}(\mathbf{r}) = e^{i\mathbf{k}\mathbf{r}}u_{\mathbf{k}}(\mathbf{r}) \text{ with } u_{\mathbf{k}}(\mathbf{r}) = u_{\mathbf{k}}(\mathbf{r} + \mathbf{a}_i) \implies \psi_{\mathbf{k}}(\mathbf{r}) = e^{i\mathbf{k}\mathbf{r}} \sum_{\mathbf{G}} c_{\mathbf{k}+\mathbf{G}} e^{i\mathbf{G}\mathbf{r}}$$

where  $\mathbf{G}$  stands for all reciprocal lattice vectors and  $c_{\mathbf{k}+\mathbf{G}}$  for the Fourier coefficients. This makes it then possible to map the problem of calculating the wavefunction of all electrons of the infinite solid to the one of calculating the wavefunction for a finite number of electrons in the unit cell for an infinite number of  $\mathbf{k}$ -vectors [56]. The corresponding

KS-equations (3.2) in reciprocal space read

$$\sum_{\mathbf{G}'} \left[ \frac{1}{2} |\mathbf{k} + \mathbf{G}|^2 \delta_{\mathbf{G}\mathbf{G}'} + v_{DFT}(\mathbf{G} - \mathbf{G}') \right] c_{i,\mathbf{k}+\mathbf{G}} = \varepsilon_i c_{i,\mathbf{k}+\mathbf{G}}$$

where  $v_{DFT}(\mathbf{G} - \mathbf{G}')$  includes the external, Hartree and XC-potential.

In this equation, the kinetic energy is diagonal whereas, on the other hand, the potential term is almost local (up to the nonlocal component of the pseudopotential) in real space [47]. Taking advantage of that, one usually solves the KS-equations by constructing the effective potential by a combined real- and reciprocal-space approach. First one computes the Hartree potential and the local external pseudopotential in reciprocal space and transforms this to real space to include the exchange-correlation potential term. Then one applies the total local-potential part to the wavefunction and transforms the product back to reciprocal space to incorporate the contribution from the nonlocal PP-component as well as the kinetic energy. This scheme heavily relies on the fast-Fourier-transform, which makes an efficient transformation between real and reciprocal space possible (the scaling is  $\mathcal{O}(M \log M)$  where  $M$  denotes the number of plane waves).

Two important approximations have to be made for the actual PW-based calculation. First, one cannot compute the wavefunctions for an infinite number of  $\mathbf{k}$ -vectors, but only for a finite set of  $\mathbf{k}$ -points ('Brillouin-zone sampling') [47]. One of the mostly used approaches for that purpose is the 'Monkhorst-Pack' mesh, which creates a uniform  $\mathbf{k}$ -grid for all crystals [48]. In practice it is (particularly for cubic lattices) advantageous not to include the highest symmetry points in the mesh (such as the  $\Gamma$ -point). However, the application of symmetry operations can reduce the calculation time significantly. For example, in cubic crystals, a mesh with 216  $\mathbf{k}$ -points in the Brillouin zone can be mapped to 10  $\mathbf{k}$ -points in the irreducible Brillouin zone, which is the smallest fraction of the Brillouin zone that is sufficient to determine all the information on the excitations of the crystal [48]. One important aspect of  $\mathbf{k}$ -point sampling is to check that the quantity of interest is converged with respect to the mesh (see Section 4.2.1). This depends, among other things, also on the system, since metals need a much denser grid than semiconductors. However, this problem can be solved by smearing the occupations near the Fermi level [47, 57], which removes instabilities in the convergence of the self-consistent procedure. But on the other hand, this also leads to an additional convergence parameter ('electronic Fermi temperature').

The second approximation is related to the representation of the wavefunction by an infinite PW-basis set. In practice, one has to truncate the series at a certain energy ('cutoff energy'  $E_C$ ), and include only plane waves with a kinetic energy smaller as  $E_C$  (formally:  $(1/2) |k + G|^2 < E_C$ ). As for the  $\mathbf{k}$ -point sampling, one has to systematically increase  $E_C$  until the quantity of interest converges to a specific value (see Section 4.2.1). As a starting point, it is useful to look at the cutoff dependence of the pseudo atom, which is often included in the output of the generated pseudopotential (e.g. in the case of the fhi98PP-code [58]). As discussed before, the number of plane waves is related to the hardness of the pseudopotential. In systems with different chemical species, it is important to keep in mind that  $E_C$  is indeed determined by the hardest pseudopotential,

and consequently this potential should be the first choice for optimization of the overall cutoff dependence [47].

Plane waves have the advantage that they incorporate the periodicity within a system naturally and the calculation of the energy and its derivatives (force, stress) is analytic and rather simple [47]. On the other hand, they are not optimized for non-periodic systems (e.g. molecules, surfaces) and systems with rapidly varying wavefunctions close to the nucleus (e.g. first-row elements).

### *Supercells*

Picking up the last point let us briefly specify how to model defects in solids. For Green's function methods the defect is incorporated into an otherwise perfect crystal [30]. Within PW-DFT, periodic boundary conditions lead to the notion of supercells. As illustrated in Figure 3.4, the idea is to represent the defect surrounded by a certain amount of bulk. This unit is then repeated periodically throughout space, which essentially means that the solid is idealized by a homogeneous arrangement of the considered defect system. Obviously this raises the problem of a spurious interaction between periodic defect images. This artificial coupling causes a dispersion of the defect bands, long-range elastic effects originating from structural distortions around the defect, and for charged defects, an artificial Coulomb interaction between the image charges and between them and the charge-compensating background. The latter effect is more important than the elastic interaction, since it scales with  $1/L$  (compared with  $1/L^3$ ) where  $L$  stands for the length scale of the supercell [62]. To address this problem, several correction schemes for the defect-formation energy have been proposed [62, 63]. In practice, one has to assure that these artificial interactions are negligible. For that purpose, one computes the quantity of interest for different supercell sizes and studies the corresponding convergence trend (Section 4.2.1). In doing so, it is important to keep the mesh density constant among different supercell sizes  $i$ . It can be estimated from the ratio  $(p_a/p_b)^3 = \Omega_b/\Omega_a$  where  $p_i$  is the mesh parameter and  $\Omega_i$  the volume of the corresponding reciprocal lattice [64].

Within the supercell approach, surfaces (and interfaces) can be modeled by a crystal slab which are separated from each other by a vacuum layer. In this case, further aspects have to be considered such as the thickness of the slab and the vacuum layer, the number of actual surface layers as well as the passivation of dangling bonds in the bulk region (i.e. the other surface of the slab). As for bulk defects, the biggest problems arise from charge and polarization effects [47]. The modelling of bulk amorphous systems by supercells is even more challenging, since they are extended in all spatial directions but without any periodicity. It is therefore difficult to match this structural features to periodic boundary conditions. We will return to this point in Section 5.1.

It has several advantages to use supercells for studying defects compared to the cluster approach [65, 66], which is particularly suited for molecular problems. First, in a cluster or nanocrystal the HOMO-LUMO gap can be considerably larger than the gap in the bulk material due to quantum confinement. Consequently, cluster models result in a smaller  $g$ -shift (Equation (2.10)) compared to a network model. Furthermore, localized surface states affect the electronic properties in the bulk region (typically according

to an exponential decay). One solution to this problem consists in passivating the surface with hydrogen, i.e. shifting these states deep into the valence band [30]. Besides that, insufficiently large clusters have a spurious macroscopic electric field. It is more important compared to the effect of surface states, since it converges to the bulk value with cluster size according to a power law. In principle, such electrostatic effects can be compensated by an external electric field. However, for that, the cluster size should be on the order of at least one crystalline unit cell.

In practice DFT-calculations include a variety of methodological and numerical approximations, which reveals the true complexity of the theoretical many-body problem stated in the beginning. Not all aspects are well understood and consequently there remains an element of empiricism in corresponding theoretical studies of material properties. In this sense, *ab initio* calculations reassemble many facets of experiments carried out in a laboratory. As for a real-world measurement apparatus, it is important to be aware of the accuracy and limitations of the used approach. Since computer experiments can also be expensive (in both, calculation time and money), they require careful planning and design before the actual submission to a computer. In doing so, it often helps to start with a simplified situation of the actual problem, which can give ideas for further more elaborated studies.

## 3.2 The g-tensor

Cluster-based approaches are computationally unfeasible for the characterization of paramagnetic defects in solids. It is far more efficient to study these systems by the sketched PW-method utilizing supercells with periodic boundary conditions and norm-conserving pseudopotentials. However, this raises conceptual problems for the computation of the EPR-parameters as we will outline in the following.

The first obstacle consists in reconstructing the all-electron information from the pseudopotential calculation. As mentioned, the pseudo wavefunction is smoother than the true wavefunction (and for norm-conserving PPs in principle even node-less [47]) in the core region. However, it is clear that such information is crucial for e.g. the isotropic hyperfine parameter (Equation (2.15)), which essentially depends on the spin density at the position of the nucleus. The solution to this problem is given by the projector-augmented method (PAW), which relates the computationally more efficient PW-approach with the more accurate concept of augmentation around each nucleus. Formally, the all-electron wavefunction  $|\psi^{AE}\rangle$  is build from the smooth pseudo wavefunction  $|\psi^{PS}\rangle$  extending throughout space and localized contributions in a muffin-tin sphere centered around each nucleus. The corresponding linear transformation reads [47, 48, 67, 68]

$$|\psi^{AE}\rangle = |\psi^{PS}\rangle + \sum_{\mathbf{R},j} (|\phi_{\mathbf{R},j}^{AE}\rangle - |\phi_{\mathbf{R},j}^{PS}\rangle) \langle p_{\mathbf{R},j} | \psi^{PS}\rangle = \mathcal{T} |\psi^{PS}\rangle \quad (3.3)$$

where  $|\phi_{\mathbf{R},j}^{AE}\rangle$  and  $|\phi_{\mathbf{R},j}^{PS}\rangle$  denote the atomic all-electron- and pseudo partial waves respectively. The projector functions  $p_{\mathbf{R},j}$  are orthogonal to the corresponding atomic pseudo partial waves ( $\langle p_{\mathbf{R},j} | \phi_{\mathbf{R}',j'}\rangle = \delta_{\mathbf{R},\mathbf{R}'}\delta_{j,j'}$ ) and are located in the augmentation region

around each nucleus. The summation runs over all atomic sites  $\mathbf{R}$ , angular momenta  $(l, m)$  and projector functions per angular-momentum channel. One typical choice is to use two projectors per  $l$ -channel with one for the bound and one for the unbound state [67, 69, 70]. By using the transformation (3.3), one can obtain the density and energy, which split into parts on either a Cartesian grid (pseudized contribution) or on radial grids (localized contributions). Consequently and advantageously, known concepts for pseudopotentials and muffin-tin potentials can be applied. From the energy, one can derive a corresponding expression for the forces and subsequently also a formulation of molecular dynamics [68]. Thus the PAW-transformation is the cornerstone for a whole formalism, which combines the efficiency of the pseudopotential plane-wave method with the accuracy of the augmented-waves methods.

To apply the PAW-formalism to the computation of the  $g$ -tensor, we first need to specify the formal problem. As mentioned in Chapter 2.2.2, the  $g$ -tensor can be obtained from second-order perturbation theory of Equation (2.4) [71, 72] (with the fine-structure constant<sup>5</sup>  $\alpha$ )

$$\mathbf{g} = \frac{2}{\alpha} \frac{\partial^2 \langle \Psi | \mathcal{H} | \Psi \rangle}{\partial \mathbf{B} \partial \mathbf{S}} \Big|_{\mathbf{B}=\mathbf{S}=0} \quad (3.4)$$

This means that the components of the  $g$ -tensor are obtained from the derivation of the Hamiltonian  $\mathcal{H}$  with respect to the external magnetic field  $\mathbf{B}$  and the net electron-spin component  $\mathbf{S}$ . Two aspects are important. First, the order in which the derivatives are taken can be interchanged [71, 73]. Secondly, the contributing terms in the Hamiltonian have to be linear in the electron spin operator or the external magnetic field or bilinear in both perturbations [73].

The magnetic field is usually incorporated into the unperturbed Hamiltonian (3.1) by the principle of minimal coupling according to which one substitutes the electron momentum operator by  $\mathbf{p} + \alpha \mathbf{A}$  [73, 74]. Within a non-relativistic treatment, this leads to the following form for  $\mathcal{H}$  within the BO-approximation [73, 74, 75]

$$\mathcal{H} = T_e + V_{ee} + V_{el} + V_{II} + \mathcal{H}^{SO} + \mathcal{H}^Z + \mathcal{H}^{ZKE} + \mathcal{H}^{SOO} \quad (3.5)$$

with the following contributions ( $g' = 2(g_e - 1)$ )

- $T_e$ : modified kinetic energy of the electrons ( $T_e = -\frac{1}{2} \sum_i [\mathbf{p}_i + \alpha \mathbf{A}(\mathbf{r}_i)]^2$ )
- $\mathcal{H}^{SO}$ : spin-orbit coupling ( $\mathcal{H}^{SO} = \frac{\alpha^2 g'}{4} \sum_i \mathbf{S}_i \cdot (\nabla V_{ee} + \nabla V_{el}) \times [\mathbf{p}_i + \alpha \mathbf{A}(\mathbf{r}_i)]$ )
- $\mathcal{H}^Z$ : electron Zeeman energy ( $\mathcal{H}^Z = \frac{\alpha g_e}{2} \sum_i \mathbf{S}_i \cdot \mathbf{B}$ )
- $\mathcal{H}^{ZKE}$ : electron Zeeman kinetic-energy correction ( $\mathcal{H}^{ZKE} = -\frac{\alpha^3 g_e}{2} \sum_i \frac{p_i^2}{2} \mathbf{S}_i \cdot \mathbf{B}$ )
- $\mathcal{H}^{SOO}$ : spin-other-orbit energy ( $\mathcal{H}^{SOO} = \alpha^2 \sum_{j \neq i} \mathbf{S}_i \cdot \nabla V_{ee} \times [\mathbf{p}_j + \alpha \mathbf{A}(\mathbf{r}_j)]$ )

---

<sup>5</sup> $\alpha = \frac{e^2}{4\pi\epsilon_0\hbar c} = 7.297353 \times 10^{-3}$  (from [39])

The spin-orbit terms can also be interpreted as the cross-product  $(-1/2)\mathbf{S}[\mathbf{p} \times \mathbf{E} - \mathbf{E} \times \mathbf{p}]$  between the momentum operator and the electric field  $\mathbf{E}_i(\mathbf{r}) = -\nabla V_i(\mathbf{r})$  due to the electronic/nuclear potential [73]. As discussed in Section 2.2.2, the spin-orbit interaction is caused by the magnetic field of the ions and other electrons as seen by the unpaired electron. The spin-other-orbit term characterizes the screening of the external magnetic field by the induced electronic currents again in the unpaired electron's system [75]. The electron Zeeman kinetic-energy correction is a relativistic effect [74]. Notably, further terms (such as the diamagnetic corrections to the spin-orbit and spin-other-orbit coupling [74] or further relativistic corrections [73]) can be included in a more sophisticated approach.

The following two problems arise for the DFT-calculation of the  $g$ -tensor [74]. First, the XC-energy becomes a functional of the relativistic four-current density ( $E_{XC}[\rho] \rightarrow E_{XC}[\rho, \mathbf{j}]$ ). However, so far there are no indications that this is a crucial aspect in the case of silicon [76]. Secondly and more importantly, one has to define the origin of the vector potential, which is however not unique ('gauge-problem'). This characteristic is crucial for the induced current density, which characterizes the response of the system to an uniform external magnetic field, and which consequently depends on  $\mathbf{A}$ . The current density is only for an infinite basis set truly gauge-invariant as expected from any physically observable quantity [77]. For a finite basis set, several techniques have been developed in the context of molecular EPR- and NMR-chemistry to circumvent this problem. Specifically, these concepts include 'gauge invariant atomic orbitals' (GIAO, a local gauge origin is incorporated in each wavefunction), the 'continuous set of gauge transformations' method (CSGT, a continuous shift of the gauge origin in real space by a parametric function) and 'individual gauges for atoms and molecules' (IGAIM, a discrete shifting of the gauge origin from one nuclei to the other) [74, 77].

However it has also become possible to account for the gauge problem within the PAW-formalism [67], which is best suited for defects in solids. One common choice for the gauge is  $\mathbf{A}(\mathbf{r}) = (1/2)\mathbf{B} \times \mathbf{r}$  so that the coordinate origin coincides with an atomic site (center of a single augmentation region). This has the advantage that the number of partial waves to describe the valence all-electron eigenstates in the augmentation region is minimized. However, the description of other augmentation regions (atomic sites) requires correspondingly large partial-wave basis sets. This can also be seen from applying a translation to the all-electron wavefunction by a vector  $\mathbf{t}$ , which reads<sup>6</sup>

$$\psi'^{AE}(\mathbf{r} - \mathbf{t}) \equiv \exp[i\mathbf{t} \cdot \mathbf{p}']\psi^{AE}(\mathbf{r} - \mathbf{t}) = \exp[(i/2c)\mathbf{r} \cdot \mathbf{t} \times \mathbf{B}]\psi^{AE}(\mathbf{r})$$

The problem of the original PAW-formulation (3.3) is that the pseudo wavefunction does not transform accordingly. One can fix it by adding the phase factor to the augmentation spheres, which means that the correspondingly modified PAW-transformation operator  $\mathcal{T}_B$  is denoted by

$$\mathcal{T}_B = 1 + \sum_{\mathbf{R}, j} e^{(i/2c)\mathbf{r} \cdot \mathbf{R} \times \mathbf{B}} [|\phi_{\mathbf{R}, j}^{AE}\rangle - |\phi_{\mathbf{R}, j}^{PS}\rangle] \langle p_{\mathbf{R}, j} | e^{-(i/2c)\mathbf{r} \cdot \mathbf{R} \times \mathbf{B}} \quad (3.6)$$

---

<sup>6</sup>A translation is defined by the operator  $f(\mathbf{r} - \mathbf{t}) = U(\mathbf{t})f(\mathbf{r}) = \exp[-i\mathbf{t} \cdot \mathbf{p}']f(\mathbf{r})$  [78]

This operator is the fundamental building block of the so-called GIPAW-approach ('gauge-including projector augmented waves'). From this transformation one can evaluate the all-electron operators  $O^{AE}$  required for the  $g$ -tensor from the corresponding pseudo-electron operators by  $O^{PS} = \mathcal{T}_B^+ O^{AE} \mathcal{T}_B$  [67, 68]. However, to illustrate the complexity of the subsequent derivation of the  $g$ -tensor, let us consider the significant contributions, which are obtained from perturbation theory for the Hamiltonian (3.5) [72, 74, 75, 79]

$$\mathbf{g} = \mathbf{1}g_e + \Delta\mathbf{g}^{ZKE} + \Delta\mathbf{g}^{SO} + \Delta\mathbf{g}^{SOO}$$

with

- $\Delta g_{xy}^{ZKE} = -\alpha^2 g_e (T^\uparrow - T^\downarrow) \delta_{xy}$  ( $T^\sigma$  is the unperturbed kinetic energy)
- $\Delta g_{xy}^{SO} = \alpha (g_e - 1) \int \left[ \mathbf{j}_x^\uparrow(\mathbf{r}) \times \nabla V_{KS}^\uparrow(\mathbf{r}) - \mathbf{j}_x^\downarrow(\mathbf{r}) \times \nabla V_{KS}^\downarrow(\mathbf{r}) \right]_y d^3r$   
( $\mathbf{j}_i^\sigma$  is the spin-dependent induced current density)
- $\Delta g_{xy}^{SOO} = 2 \int \mathbf{B}'_{xy}(\mathbf{r}) (\rho^\uparrow(\mathbf{r}) - \rho^\downarrow(\mathbf{r})) d^3r$   
( $\mathbf{B}'_{xy}(\mathbf{r})$  is the magnetic field due to the total induced current  $\mathbf{j}(\mathbf{r})$  including a self-interaction correction)

The spin-orbit coupling terms require the calculation of the induced current and magnetic field. Within the GIPAW-approach, one applies the transformation operator (3.6) to the all-electron current operator  $\mathbf{J}(\mathbf{r}) = -(1/2) \{\mathbf{p}, |\mathbf{r}\rangle \langle \mathbf{r}|\} - (\mathbf{A}(\mathbf{r})/c) |\mathbf{r}\rangle \langle \mathbf{r}|$  where  $\{\}$  stands for the anti-commutator [67, 77]. Within first-order perturbation theory, the first term causes a paramagnetic current contribution, which depends on the first-order perturbed wavefunction. The second term results in a diamagnetic contribution, which only depends on the unperturbed charge density, which can be further processed by using density-functional perturbation theory [67]. The induced magnetic field follows then from the first-order induced current by using Biot-Savart's law.

In conclusion, the computation of the  $g$ -tensor requires elaborate theoretical concepts and the actual implementation is tedious. In the following, we will use Quantum Espresso [80] for that purpose. For completeness, we mention that the GIPAW-approach was originally developed for the computation of the conceptually similar NMR-parameters [67]. Furthermore, there are two important alternatives to the sketched perturbative  $g$ -tensor calculation in periodic systems. One is based on writing the  $g$ -tensor in terms of the orbital magnetization [81], in which one essentially interchanges the order of the derivatives in Equation (3.4) and evaluates the derivative to  $\mathbf{S}$  numerically from a fixed- $\mathbf{S}$  calculation with SO-coupling in the self-consistent Hamiltonian. In the other approach, one uses maximally localized Wannier orbitals to compute the current densities [72]. Besides that, corresponding approaches for Gaussian and augmented plane-waves [79] as well as for atomic orbitals [82] have been developed.

### 3.3 Hyperfine parameters

The hyperfine tensor follows analogously to the  $g$ -tensor from second-order perturbation theory with respect to the nuclear-spin angular-momentum and the electron spin [73]

$$\mathbf{A} = \left. \frac{\partial^2 \langle \Psi | \mathcal{H} | \Psi \rangle}{\partial \mathbf{I} \partial \mathbf{S}} \right|_{\mathbf{B}=\mathbf{S}=0} \quad (3.7)$$

which is then often decomposed into an isotropic and an anisotropic part (as discussed in Chapter 2.2.3). In contrast to the  $g$ -tensor there are no methodological problems to solve, but instead the main challenges arise from including effects such as relativistic corrections or core polarization.

Within spin-DFT one usually starts from the Dirac equation by making the same substitution for the momentum operator  $\mathbf{p} + \alpha \mathbf{A}$  as for the  $g$ -tensor [30, 83, 84]. First-order perturbation theory and rewriting of the small two-component Pauli spinor in terms of the large spinor  $\Phi_1$  (feasible for light atoms) yields then the following expectation value for the hyperfine interaction

$$E^{HF} = E^{contact} + E^{orb} + E^{dip}$$

where the terms read explicitly

- $E^{contact} = -\frac{4\pi}{3} \langle \Phi_1 | U(\mathbf{r}) \boldsymbol{\mu}_I \cdot \boldsymbol{\sigma} \delta(\mathbf{r}) | \Phi_1 \rangle + \langle \Phi_1 | \frac{1}{r^4} \frac{\partial U}{\partial r} [\boldsymbol{\mu}_I \cdot \boldsymbol{\sigma} r^2 - (\boldsymbol{\mu}_I \cdot \mathbf{r})(\boldsymbol{\sigma} \cdot \mathbf{r})] | \Phi_1 \rangle$
- $E^{orb} = -\alpha \boldsymbol{\mu}_I \cdot \langle \Phi_1 | \frac{\mathbf{U}(\mathbf{r}) \cdot \mathbf{L}}{r^3} | \Phi_1 \rangle$
- $E^{dip} = \frac{1}{2} \langle \Phi_1 | \frac{U(\mathbf{r})}{r^5} [\boldsymbol{\sigma} \cdot \boldsymbol{\mu}_I r^2 - 3(\boldsymbol{\mu}_I \cdot \mathbf{r})(\boldsymbol{\sigma} \cdot \mathbf{r})] | \Phi_1 \rangle$

with  $U(\mathbf{r}) = [1 + \frac{\alpha^2}{2}(E - V(\mathbf{r}))]$  and where  $\boldsymbol{\mu}_I = g_N \mu_N \mathbf{I}$  is the magnetic moment of the nucleus, and  $\boldsymbol{\sigma}$  the Pauli spin matrices.

Let us first discuss the contact term  $E^{contact}$  for a pure Coulomb potential  $V(r) = -Z/r$  [30, 83, 85]. In the non-relativistic limit  $U(\mathbf{r}) \rightarrow 1$  only the first term contributes, which also corresponds to the classical finding that the contact energy just depends on the density at the nucleus (see also Equation (2.15)). However, in the relativistic case this term vanishes, since  $U(\mathbf{r}) \sim \mathbf{r}$ . For the second term, it is important to note that the derivative  $\partial U(\mathbf{r})/\partial r$  yields a broadened delta-function, which then modifies the definition of the isotropic coupling

$$\mathcal{H}^{contact} = a \mathbf{S}^T \cdot \mathbf{I}, \quad a = \frac{4\pi}{3S} g_n g \mu_n \mu_B \int m(r) \delta_{TH}(r) d^3r \quad (3.8)$$

where the smeared delta-function is given by

$$\delta_{Th}(|\mathbf{r}|) = \frac{1}{4\pi r^2} \frac{\partial U}{\partial r} = \frac{1}{4\pi r^2} \frac{Z\alpha^2/2}{[(1 + \alpha^2 E/2)r + Z\alpha^2/2]^2}$$

To summarize, the isotropic hyperfine coupling is averaged over a sphere with radius  $Z\alpha^2$ , which is about ten times the size of the nucleus [30]. It is clear that such relativistic

corrections become more important for heavier atoms. However, they also solve the problem of the divergence occurring for relativistic  $s_{1/2}$ - and  $p_{1/2}$ -wavefunctions, which scale close to the nucleus like  $\Phi(r) \sim r^{\lambda-1}$  with  $\lambda = (1 - \alpha^2 Z^2)^{1/2}$  [85]. This also implies that the scalar-relativistic correction becomes in practice larger, the more we move the origin of the radial grid closer to  $r = 0$ .

The orbital momentum is quenched if the ground state of the defect is a single-determinant orbital singlet, i.e. the ground state corresponds to only one Slater determinant and is non-degenerate except for spin degeneracy [30, 83]. In this case the orbital hyperfine coupling  $E^{orb}$  essentially vanishes. The degeneracy of an orbital multiplet is removed by either a Jahn-Teller distortion (see Section 4.1) or interactions such as (most importantly) the spin-orbit coupling.

Within the PAW-formalism, one can compute the isotropic coupling from Equation (3.8) where the corresponding density is obtained from  $m^{AE}(\mathbf{r}) = m^{PS}(\mathbf{r}) + m_{at}^{AE}(\mathbf{r}) - m_{at}^{PS}(\mathbf{r})$ , i.e. the pseudo density  $m^{PS}(\mathbf{r})$  and the atomic all-electron/pseudo densities  $m_{at}^{PS}(\mathbf{r})$ ,  $m_{at}^{AE}(\mathbf{r})$  as obtained from the PAW partial waves. The anisotropic contribution can be computed from (2.16) by the following expression [86]

$$T_{ij}(\mathbf{R}) = \frac{\mu_0}{4\pi} g_n g \mu_n \mu_B \int \left( \partial_i \partial_j - \frac{1}{3} \delta_{ij} \nabla^2 \right) \bigg|_{\mathbf{R}} \frac{m(\mathbf{r}')}{|\mathbf{r} - \mathbf{r}'|} d^3 r$$

Noteworthy, if one considers only one partial wave per angular momentum and site [40], the expressions for the hyperfine coupling simplify significantly. In particular, the spin density at the nucleus is then given by

$$m^{AE}(\mathbf{R}) = m^{PS}(\mathbf{R}) |\phi^{AE}(\mathbf{R})|^2 / |\phi^{PS}(\mathbf{R})|^2 \quad (3.9)$$

which essentially means that the all-electron spin density is the rescaled pseudo density. This form has the advantage that it is easy to implement also if scalar-relativistic effects (3.8) are taken into account. Furthermore, it is often sufficient for conceptual studies such as the dependence of the hyperfine parameters on the local defect geometry in silicon [87].

On the other hand, it is important to be aware of the limitations of this single-projector approach. For that purpose, let us consider the silyl-radical ( $\text{SiH}_3$ ), which will be further characterized in the next chapter. The implementation of Equation (3.9) into S/PHI/nX reveals the following important deficiencies. First, the isotropic hyperfine shows a significant dependence on the cutoff energy and convergence is only obtained for  $E_C > 100$  Ry. However, this problem can be solved by rescaling the spin density  $m^{AE}(\mathbf{R})$  with the spin density of a free atom computed in a large supercell and at the same cutoff energy [40, 88]. This improves the convergence trend dramatically and follows the same principle of error cancellation as also observed for total energies and their differences respectively. Besides that, there are two other problems related to the usage of only one projector. If we compute the  $a$ -parameter from the projection over a finite range  $r_{PAW}$  on the radial grid, we obtain the trends shown in Figure 3.5. We learn from it, that there is a strong dependence on the used functional and pseudopotential type. The latter is resolved for projections over a sufficiently large region. However,

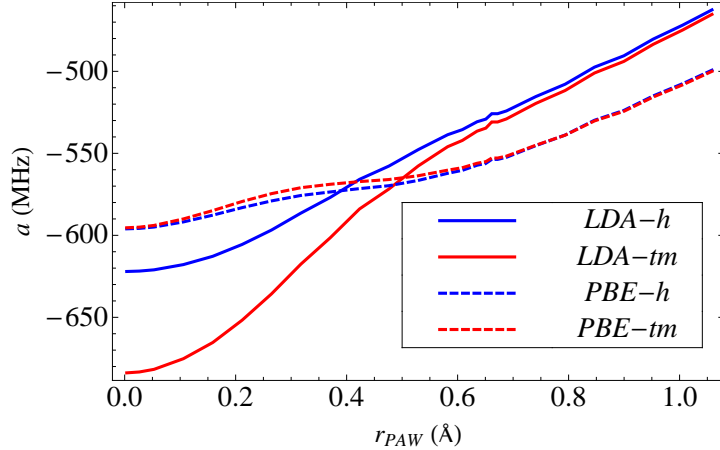


Figure 3.5: Dependence of the isotropic hyperfine parameter on the radius of the PAW-reconstruction for the  $\text{SiH}_3$  radical. We consider the LDA- and PBE-functional and Hamann (h) and Troullier-Martin (tm) pseudopotentials generated with the fhi98-PP code [58] using default values. We use the same relaxed structure for both pseudopotentials to remove geometrical effects (even though they are small). The projector cutoff function is a step function.

we also see that the  $a$ -parameter depends sensitively on  $r_{PAW}$  and we consequently do not obtain a reliable value. Notably, similar effects are also observed for the anisotropic hyperfine parameter. These problems are only solved by using more projectors, and we will use a corresponding implementation (Quantum Espresso [80]) in the following to assure that our findings are independent from such influences.

Core polarization can also be incorporated into the pseudopotential-based computation of the hyperfine parameters. In one approach one solves the unrestricted KS-equations only for core states in the external potential of the spin-dependent frozen valence densities [89]. The second method consists of a two-step procedure [90]. First, one reconstructs the frozen-core all-electron wavefunctions by using the PAW-transformation (3.3). From these wavefunctions one computes a local spin-dependent perturbing potential, which is subsequently used for the calculation of the spin-polarized core levels within first-order perturbation theory. Most notable applications of these schemes are first-row based molecules (e.g.  $\text{CH}_3$  [89, 90], fullerenes [91]), and transition-metal complexes [90]. However, for our silicon-based defects, core polarization can be in general neglected.

The computation of the hyperfine parameters has a long history within all-electron approaches, since it can be obtained directly from the spin density. In chemistry, it has been applied to the study of molecular radicals and technical aspects such as the basis set or the XC-functional have been studied extensively [65, 92, 93]. Recent concepts applicable to periodic boundary conditions include a Green’s function approach using a linear muffin-tin potential [83], a mixed basis-set approach (i.e. localized nucleus-centered orbitals and plane waves) [90], a hybrid Gaussian and augmented plane-wave scheme (all-electron treatment of the nuclei of interest and a pseudopotential approx-

imation for the remaining atoms) [72], and a Bloch basis set consisting of numerical and Slater-type atomic orbitals [94]. This illustrates that also the computation of the hyperfine parameters is still an active field.

### 3.4 Summary

Density-functional theory is a powerful practical approximation to the many-body problem of electronic-structure theory. In the most important realization of DFT, one solves the Kohn-Sham equations for an auxiliary system of noninteracting particles in a self-consistent way. In practice, several additional approximations, both conceptual and numerical, are required. One convenient method for solids is a pseudopotential approach combined with a plane-wave basis set.

The computation of the EPR-parameters within a pseudopotential approach is only possible by reconstructing the all-electron wavefunction in the core region. The PAW-transformation provides the necessary framework, which, however, in its original formulation does not account for the gauge-freedom of the vector potential. For the computation of the  $g$ -tensor it is therefore necessary to modify the transformation by appropriate phase factors in the augmentation regions (GIPAW-formalism). In contrast to that, it is rather easy to obtain the hyperfine parameters from the all-electron density. Within a pseudopotential approach, the parameters can be computed by making again use of the PAW-reconstruction scheme. For the isotropic hyperfine parameter it is important to account for the divergence of scalar-relativistic wavefunctions at the nucleus by averaging the corresponding density over a region slightly larger as the core radius. Furthermore, the  $a$ -parameter depends critically on the choice of the projector within the single-projector approximation. Consequently, this simplified approach is only useful for the characterization of general trends.

# 4 Dangling bonds in molecular and crystalline silicon systems

## 4.1 Modelling

Before we address to the dangling bond in the amorphous matrix, let us consider its crystalline counterpart. In this case, the dangling bond is embedded in a homogeneous network and can therefore be characterized by the local defect structure. This gives us the possibility of considering the influence of the bonding geometry at the db-atom on the EPR-parameters in a systematic way. Furthermore, some crystalline db-systems have been studied experimentally by EPR, and from these db-defects we can get an estimate for the achievable agreement between theory and experiment.

From the theoretical point of view, the simplest dangling-bond test systems are small radicals such as the silyl- ( $\text{SiH}_3$ ), disilyl- ( $\text{Si}_2\text{H}_5$ ), trisilyl- ( $\text{Si}_3\text{H}_7$ ), and tetrasilyl ( $\text{Si}_4\text{H}_9$ ) radical. The silyl and the tetrasilyl radical are particularly interesting, since they characterize the bonding of the db-atom to only hydrogen or to only silicon respectively. Consequently, the overall db-structure is also homogeneous, which makes it easier to study the influence of the structural parameters on the EPR-parameters. Unfortunately it is difficult to isolate these radicals experimentally. For example, the silyl radical is obtained by the reaction of silane ( $\text{SiH}_4$ ) with H produced by the photolysis of hydrogen iodide (HI) in a host matrix such as argon, xenon, or krypton at low temperatures [95, 96]. However, the rare-gas matrix exerts an important influence as can be seen from Table 4.2. Similar reasoning holds for the other mentioned radicals and it is therefore not possible to use these systems for the purpose of comparison between theory and experiment. Despite that, we can employ these cluster models to benchmark the GIPAW-method with a more accurate all-electron approach (Section 4.2.2). Additionally they are valuable for simple conceptual studies (as e.g. in the previous chapter or in Section 4.3.1 and 4.4.1).

The effect of the further defect surrounding on the EPR-parameters can only be investigated by sufficiently large cluster models. But they have several drawbacks such as the (possibly artificial) termination of surface bonds or the overestimation of the electronic gap due to quantum confinement (Chapter 3.1.2). These problems can be circumvented by using supercells with periodic boundary conditions, which we will use in the following. For that purpose we have to generate the db-defect in the continuous crystalline network. In doing so, the first step consists in removing a silicon atom from the lattice (Figure 4.1(a)). This cuts 4 Si-Si bonds, and creates up to four dangling bonds in very close proximity. Notably the resulting monovacancy  $V$  in its charge states

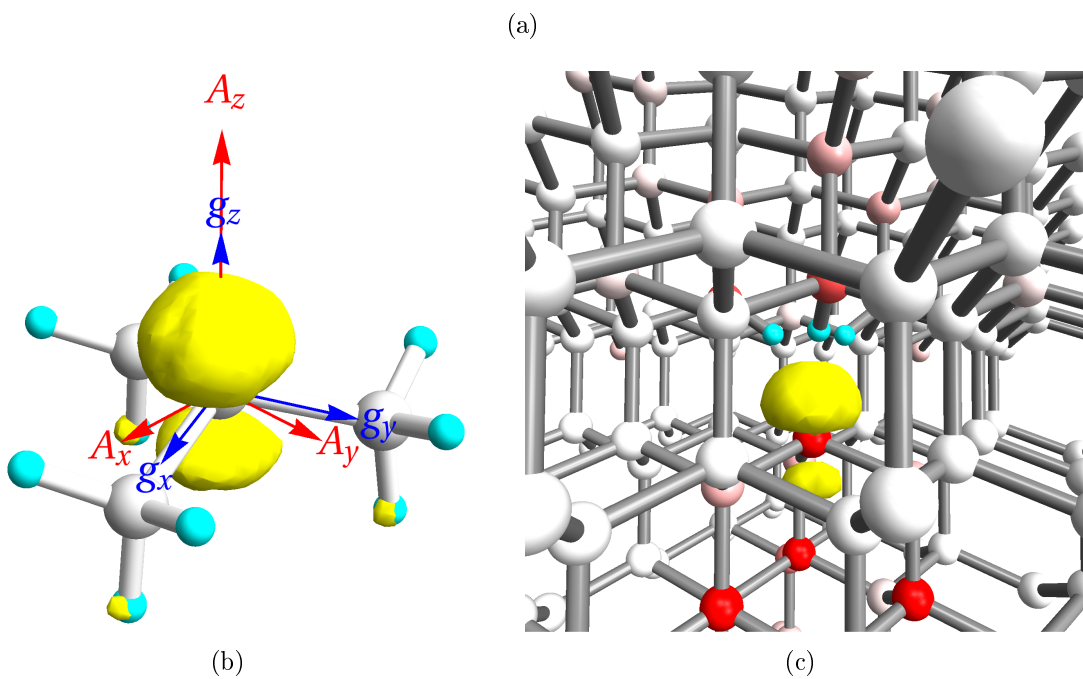
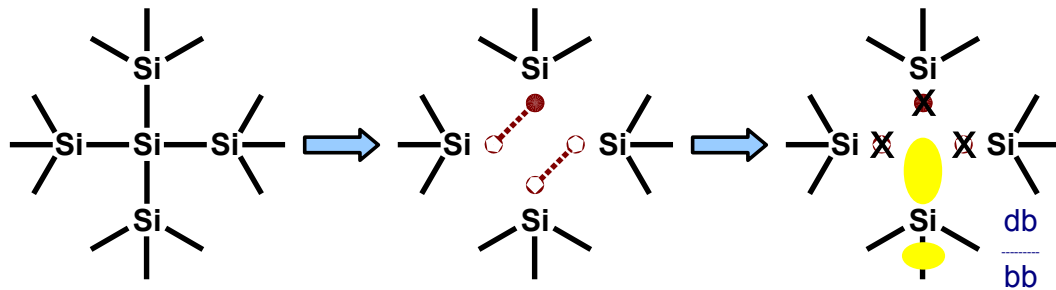


Figure 4.1: Illustration of the db-defect in silicon. (a): The creation of a db-defect in bulk. (b): Molecular db-system (tetrasilyl) with principal values for the EPR-tensors and spin density (yellow color). (c): The db-defect in the crystalline network. The turquoise color indicates hydrogen and the red color a strong isotropic hyperfine interaction.

is also EPR-active [43] but for theory it is difficult to obtain a reliable relaxed structure due to the flat energy surface [30, 97, 98, 99]. In the second step we have to find a way to remove three of the electrons in the vacancy, so that only one unpaired electron remains. One possibility is to passivate the corresponding bonds with hydrogen yielding the defect configuration  $V(\text{SiH})_3$  (the defect neighbors are given in brackets). This defect (Figure 4.1(c) and Figure 4.2(b)) has in fact been detected by Fourier-transform infrared [100, 101, 102] and Raman [103, 104] spectroscopy. We also apply the same idea of hydrogen passivation to a larger vacancy  $V_4(\text{SiH})_9$ , since this corresponds to a more open defect configuration inside the vacancy. Another approach to remove three of the excessive electrons consists in replacing the vacancy neighbors by impurities, e.g. by phosphorus  $V(\text{P}_3)$  or aluminum  $V(\text{Al}_2\text{SiH})$ . Besides these bulk-based db-defects, we also consider the extreme case that there are no atoms opposite the dangling bond. This is achieved by creating the defect on a H-passivated Si(111) surface, and it can be thought of as removing all layers above the db-atom in Figure 4.1(c).

There is no EPR-data available for the sketched db-models. With the exception of the  $V(\text{SiH})_3$  defect, this is not surprising, since the models are rather artificial and unlikely to be stable in nature. Thus the problem of finding a good test system for the comparison with experiment remains. It is solved by the vacancy-oxygen complex (the *A*-center) when an additional hydrogen binds to one of the silicon defect neighbors ( $V(\text{SiHO})$ , Figure 4.2(a)). The EPR-parameters of this system have been measured successfully [41]. Besides that, there are two defect complexes, which have also shown a db-character in experiment [42, 105]: the vacancy with substitutional phosphorus (the *E*-center,  $V(\text{Si}_3\text{P})$ , Figure 4.2(d)) and with a single hydrogen trapped inside the vacancy ( $V(\text{Si}_3\text{H})$ , Figure 4.2(c)). The novelty of both is that the geometrical arrangement of the three equivalent silicon defect neighbors causes a symmetry-lowering Jahn-Teller (JT) distortion<sup>1</sup> during relaxation. We will show in the following section that theory can reproduce the observed characteristics even for these JT-distorted systems quite well.

## 4.2 Quantification of the accuracy

### 4.2.1 Convergence tests

To quantify the accuracy of our supercell-based DFT-approach we have to test the corresponding computational and physical approximations. As discussed in Section 3.1.2, the relevant parameters are checked by convergence tests, which means that one computes the dependence of the quantity of interest (e.g. the principal values of the *g*-tensor) on the numerical input parameters (e.g. the cutoff energy). Ideally, one carries out such tests for all parameters. In practice this also depends on the problem at hand. For example, a well-relaxed atomic structure is not so crucial for the study of bond-parameter dependencies (see Section 4.4), where relaxation is mainly used to recover the correct

---

<sup>1</sup>Every nonlinear molecule or crystal defect that has orbital electronic degeneracy when the nuclei are in a symmetrical configuration is unstable with respect to at least one asymmetric distortion of the nuclei which lifts the degeneracy. (cited from [106])

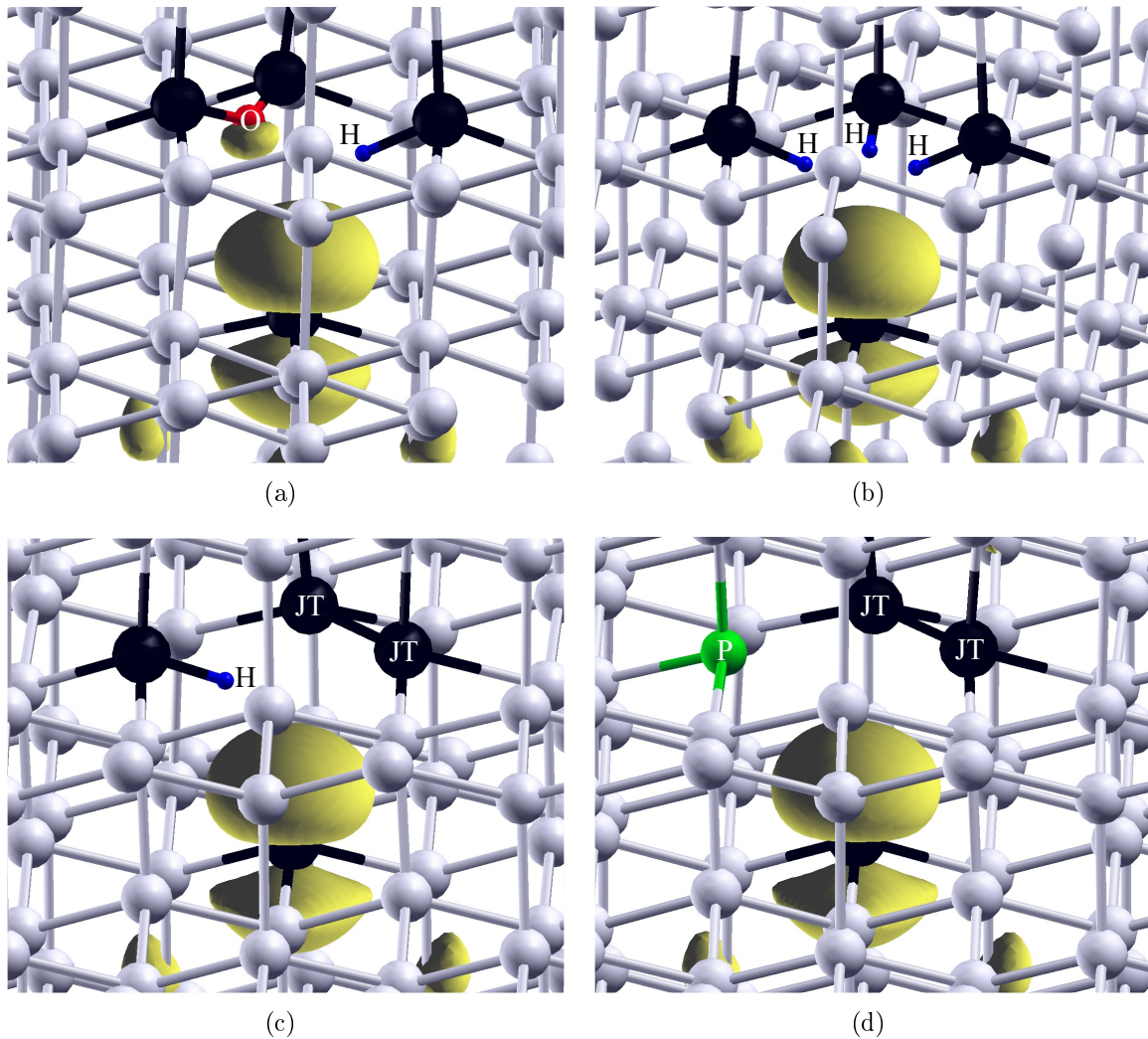


Figure 4.2: (a): The  $V(\text{SiHO})$  db-model: oxygen (red color) bonds to two neighbors (black color) of the vacancy. The hydrogen atom (in blue) passivates the broken bond of the third neighbor, leaving one unpaired electron, which is located on the fourth neighbor of the vacancy (as indicated by the spin density in yellow). Notably there is also spin polarization on the oxygen atom. (b): The  $V(\text{SiH})_3$  db-model: three hydrogen atoms passivate the corresponding broken bonds of the vacancy. (c): The  $V(\text{Si}_3\text{H})$  db-model: Two neighbors (JT) of the vacancy form a long bond, whereas the third is again passivated by hydrogen. (d):  $V(\text{Si}_3\text{P})$  db-model: Again two silicon atoms (JT) combine. Substitutional phosphorus (green color) removes the third electron from the vacancy.

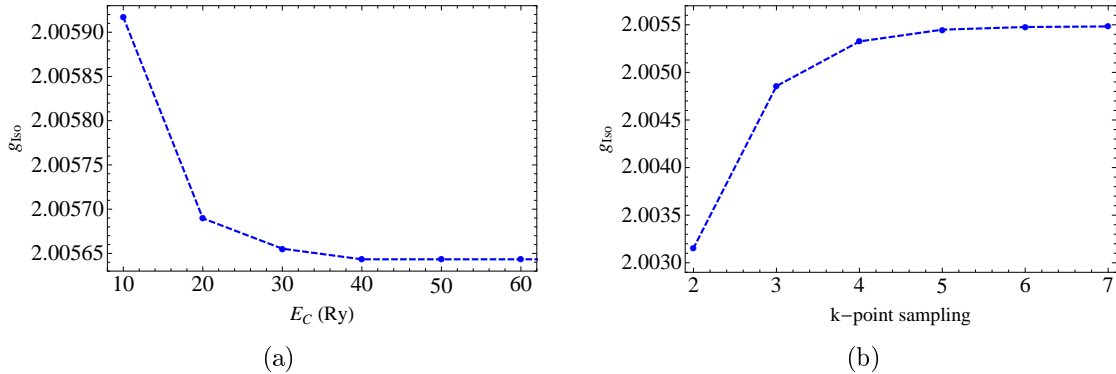


Figure 4.3: Convergence of the isotropic  $g_{Iso}$ -value with respect to the cutoff energy  $E_C$  ( $\text{Si}_4\text{H}_9$  radical) and  $\mathbf{k}$ -point sampling ( $V(\text{SiHO})$  db-model). Note that the  $y$ -scale in (a) is already one magnitude smaller than usually required.

distance between the db-atom and its neighbors.

However, as discussed in Section 3.1.2,  $\mathbf{k}$ -point sampling and cutoff energy  $E_C$  are two key parameters, which always have to be converged. To check for the dependence of the EPR-parameters on these quantities, we have carried out calculations with the QUANTUM ESPRESSO [80] (v4.2.1) DFT-code for the tetrasilyl radical and the  $V(\text{SiHO})$  defect. As always, we take the Perdew-Burke-Ernzerhof (PBE)-functional [60]. The norm-conserving pseudopotentials (including the GIPAW-reconstruction data) have been generated by Ari P. Seitsonen. The potential for silicon also includes a scalar-relativistic correction as described in Chapter 3.3. In order to minimize artifacts due to the defect-band dispersion in small supercells, we constrain the total magnetization, which yields full occupation of the defect band in the spin majority channel and empty occupation in the minority channel, respectively. For the computation of the EPR-parameters we usually increase the convergence threshold for self-consistency from  $10^{-8}$  used for structural relaxation by at least two magnitudes. The calculation of the tetrasilyl radical is done in a cubic cell with a length of  $10.58 \text{ \AA}$  and for the  $\mathbf{k}$ -point  $\mathbf{k} = (1/4, 1/4, 1/4)$ . The  $\mathbf{k}$ -point sampling test for the crystalline db-model is carried out in a  $2 \times 2 \times 2$  supercell at 30 Rydberg and with a  $\mathbf{k}$ -point grid offset.

As illustrated in Figure 4.3(a), the isotropic  $g_{Iso}$ -value shows only a weak dependence on the cutoff energy and it is converged to within  $2 \cdot 10^{-5}$  for 30 Rydberg. On the contrary, there is a strong dependence on the  $\mathbf{k}$ -point mesh. We have to use a  $6 \times 6 \times 6$  mesh to obtain an accuracy on the order of  $10^{-4}$ . For the hyperfine parameters we observe the following trends. In contrast to the single-projector approach, a small cutoff energy of (again) 30 Rydberg already yields reliable results. The corresponding dependence on the  $\mathbf{k}$ -point sampling is not as significant as for the  $g$ -tensor, and one usually obtains converged values for a  $3 \times 3 \times 3$  mesh. Since a coarser grid also decreases the computation time dramatically, we use it in the following whenever we are not interested in the  $g$ -tensor. The hyperfine parameters of hydrogen have similar dependencies on  $E_C$  and

	$V(\text{SiHO})$			$V(\text{SiH})_3$		
	$g_{Iso}$	$a$ (MHz)	$b$ (MHz)	$g_{Iso}$	$a$ (MHz)	$b$ (MHz)
$2 \times 2 \times 2$	2.0064	-374	-51	2.0086	-340	-54
$3 \times 3 \times 3$	2.0071	-367	-51	2.0103	-329	-53
$\Delta$	0.0007	2%	0	0.0017	3%	2%

Table 4.1: Comparison of a  $2 \times 2 \times 2$  (64 Si atoms without the defect) with a  $3 \times 3 \times 3$  (216 Si atoms without the defect) supercell for two db-models. The silicon atoms are kept fixed at the ideal lattice positions, whereas the relaxed positions of oxygen and hydrogen are transferred from one supercell size to the other. This ensures that the overall geometry is the same in both supercells.

	$\text{SiH}_3$			$\text{Si}_4\text{H}_9$		
	$g_{Iso}$	$a$ (MHz)	$b$ (MHz)	$g_{Iso}$	$a$ (MHz)	$b$ (MHz)
G03	2.0044	-633	-85	2.0063	-337	-81
QE (4.2.1)	2.0037	-540	-86	2.0056	-293	-82
$\Delta$	0.0007	19%	1%	0.0007	13%	1%
<i>Experiment</i>						
Ar-matrix [96]	2.0038	665	166	-	-	-
Ar-matrix [107]	2.0036	-	-	-	-	-
Kr-matrix [108]	2.0013	745	-	-	-	-
Kr-matrix [107]	2.0013	-	-	-	-	-
Xe-matrix [95]	2.0030	517	-	-	-	-
Xe-matrix [109]	2.0030	532	-	-	-	-

Table 4.2: EPR-parameters of small radicals computed with Quantum Espresso [80] (v4.2.1) and GAUSSIAN03 [110]. For the PP-calculation, we take the relaxed atomic structure from the all-electron calculation. For the silyl radical we also show experimental results for different host matrices.

the  $\mathbf{k}$ -point sampling. Furthermore, we verified to note that the convergence trends discussed here are representative for all db-models.

Within the supercell approach it is necessary to check for the interaction between the defect and its periodically repeated images. For that purpose we consider the EPR-parameters of the  $V(\text{SiHO})$  and  $V(\text{SiH})_3$  defect for different supercell sizes. In doing so, we keep the overall geometry fixed (Figure 4.1) to decouple electronic from structural effects. We see from Table 4.1 that the difference between the small and the large supercell is only significant for the  $g$ -tensor. Consequently, as for the  $\mathbf{k}$ -point sampling, we will use larger supercells whenever we also need well-converged  $\mathbf{g}$ -eigenvalues.

## 4.2.2 Comparison to an all-electron method

As mentioned in Section 3.1.2, to check for the quality of a pseudopotential, one should carry out test calculations and compare them with corresponding all-electron calculations. For that purpose, we compute the EPR-parameters for the silyl and tetrasilyl radical with GAUSSIAN03 [110] using again a PBE-functional [60]. To ensure convergence with respect to the Gaussian basis set we employ a 6-311+G(d) set for the non-relativistic structural optimization. For the calculation of the EPR-parameters we use an uncontracted WTBS basis set for silicon and the EPR-III basis set for hydrogen, with a Douglas-Kroll-Hess 0-order relativistic Hamiltonian. To disentangle methodological from structural effects, we take the relaxed GAUSSIAN03 structure<sup>2</sup> also for the GIPAW-calculation.

For the comparison of both methods we consider  $g_{Iso}$  as well as the hyperfine parameters (Table 4.2). We obtain reasonable agreement for the isotropic  $g$ -value (within  $10^{-3}$ ), and for the anisotropic hyperfine parameter (about 1%). In contrast, there is a significant deviation for the  $a$ -parameter. It can be partly explained by the neglect of core polarization in our pseudopotential approach. The hyperfine parameters for hydrogen have a similar accuracy, specifically the deviations for  $a$  are only slightly larger (28% [SiH<sub>3</sub>], 15% [Si<sub>4</sub>H<sub>9</sub>]) and for the  $b$ -parameter they are on the same order as for the db-atom.

Furthermore, Table 4.2 illustrates the large scattering in the measured EPR-parameters for SiH<sub>3</sub>. The  $g_{Iso}$ -value depends on the host matrix, since different experiments on the same rare-gas matrix deviate from each other by  $2 \cdot 10^{-4}$  at the most. For  $g_{Iso}$  and  $a$  there is actually acceptable agreement between the experiment in an Ar-matrix [96] and the all-electron calculation. Notably, in both cases the relative sign between  $a$  and  $b$  is also the same. However the discrepancy in the anisotropic parameter is very large ( $b_{Exp} \sim 2b_{Theory}$ ), but a detailed analysis of this deviation requires further experimental confirmation of  $b_{Exp}$ . We also see from the table that the  $a$ -parameter has a considerable variation amongst different measurements. Additionally, to our knowledge, there is no experimental EPR-data available for the Si<sub>4</sub>H<sub>9</sub> radical. Both aspects illustrate that we can use these small radicals only for a theory-theory comparison.

## 4.2.3 Comparison to experiment

As we have just seen, molecular systems cannot be used to validate theory against experiment. However, as mentioned, the EPR-parameters for the  $V(\text{SiHO})$   $c$ -Si db-system have been measured with a sufficient accuracy [41]. Two other defect systems have shown a db-character in experiment [42, 105], namely the  $V(\text{SiH})$  and the  $V(\text{Si}_3\text{P})$  defect. But in these systems the defect geometry should be lowered by a JT-distortion and it is *a priori* unclear whether we can reproduce this effect properly.

In silicon essentially three kinds of JT-systems have been studied so far, namely the monovacancy [30, 97, 98, 99], the  $E$ -center [42, 105, 111], and the divacancy [112, 113,

---

<sup>2</sup>Actually both yield similar relaxed structures. The bond angles deviate only by  $0.2^\circ$  and the bond lengths by  $0.01 \text{ \AA}$ .

		$V(\text{SiHO})$	$V(\text{SiH})_3$	$V(\text{Si}_3\text{H})$	$V(\text{Si}_3\text{P})$
$g_{Iso}$	theory	2.0059	2.0074	2.0060	2.0068
	exp. [41, 42, 105]	2.0061	-	2.0070	2.0071
	$\Delta$	-0.0002	-	-0.0010	-0.0003
$g_X$	theory	2.0082	2.0108	2.0121	2.0128
	exp. [41, 42, 105]	2.0086	-	2.0114	2.0112
	$\Delta$	-0.0004	-	0.0007	0.0016
$g_Y$	theory	2.0081	2.0108	2.0063	2.0079
	exp. [41, 42, 105]	2.0084	-	2.0090	2.0096
	$\Delta$	-0.0003	-	-0.0027	-0.0017
$g_Z$	theory	2.0013	2.0005	1.9995	1.9996
	exp. [41, 42, 105]	2.0013	-	2.0006	2.0005
	$\Delta$	0	-	-0.0011	-0.0009
$\Theta$	theory	39.1°	35.3 °	27.2°	30.6°
	exp. [41, 42, 105]	39.2°	-	32.4°	32°
	$\Delta$	-0.1°	-	-5.2°	-1.4°

Table 4.3: Comparison of *ab initio* calculations with experiment for the  $g$ -tensor for various deep-level defects in crystalline silicon. The isotropic component is denoted by  $g_{Iso}$ , and  $g_X$ ,  $g_Y$ ,  $g_Z$  stand for the eigenvalues associated with the corresponding principle axis.  $\Theta$  is the angle between  $Z$  and the [110]-axis.

114, 115]. For the  $E$ -center and the divacancy, there has been a long debate concerning the true symmetry-lowering relaxation mode of the ground state, which can be either resonant or pairing [99, 116]. In the case of the pairing JT-distortion two defect neighbors form a long Si-Si bond, so that the distance between these atoms  $d_1$  becomes smaller than their common distance to the third neighbor  $d_2$  (i.e.  $d_1 < d_2$ ). The resonant JT-relaxation mode corresponds to the opposite case: two atoms move apart while the third neighbor moves towards both atoms, so that finally there are two shorter distances and a larger one (i.e.  $d_1 > d_2$ ). As *ab initio* calculations have shown, both configurations have a similar formation energy and have consequently a comparable stability [99, 117, 118, 119].

First we have to specify the computational parameters for relaxation. Structural convergence<sup>3</sup> is achieved on a  $3 \times 3 \times 3$   $\mathbf{k}$ -point mesh and for a plane-wave cutoff of 30 Rydberg. The initial structures reflect the perfect  $D_{3d}$  defect symmetry, and in particular, we do not place any symmetry constraints on the expected JT-distortion for the  $V(\text{Si}_3\text{H})$  and  $V(\text{Si}_3\text{P})$  db-model. The maximum force on an atom is below 4 meV/Å which is adequate for getting the characteristics of the db-models.

The relaxation pattern strongly depends on the chemical composition of the defect complex. In the case of  $V(\text{SiHO})$  the two silicon atoms bonded to the oxygen move into the vacancy, while in turn, the db-atom and the neighbor with the attached hydrogen move outwards. The resulting defect symmetry is  $C_{1h}$  in accordance with previous findings [41, 121]. The bond lengths of the db-atom to its next neighbors are shorter in

<sup>3</sup>The  $a$ -parameter is usually a good indicator for the convergence of the defect structure.

		$V(\text{SiHO})$	$V(\text{SiH})_3$	$V(\text{Si}_3\text{H})$	$V(\text{Si}_3\text{P})$
$a$ (MHz)	theory	-292	-314	-337	-350
	exp. [41, 42, 105]	-297	-	-328	-347
	$\Delta$	5 (2%)	-	-9 (3%)	-3 (1%)
	theory [120] (tb)	-	-498	-457, -464	-
$b$ (MHz)	theory	-61	-60	-52	-52
	exp. [41, 42, 105]	-61	-	-53	-52
	$\Delta$	0	-	1 (3%)	0
	theory [120] (tb)	-	-56	-47, -44	-
$A_X$ (MHz)	theory	-230	-253	-285	-300
	exp. [41, 42, 105]	-236	-	-275	-295
$A_Y$ (MHz)	theory	-231	-253	-285	-300
	exp. [41, 42, 105]	-236	-	-275	-295
$A_Z$ (MHz)	theory	-414	-434	-442	-451
	exp. [41, 42, 105]	-418	-	-435	-450
$\Theta$	theory	$34.7^\circ$	$35.3^\circ$	$35.4^\circ$	$35.4^\circ$
	exp. [41, 42, 105]	$35.3^\circ$	-	$35.3^\circ$	$35.3^\circ$
	$\Delta$	$-0.6^\circ$ (2%)	-	$0.1^\circ$ (0%)	$-0.1^\circ$ (0%)
	theory [120] (tb)	-	$35.3^\circ$	$35.3^\circ, 35.5^\circ$	-

Table 4.4: Comparison of *ab initio* calculations with experiment for the  $A$ -tensor for various deep-level defects in crystalline silicon.  $a$  stands for the isotropic and  $b$  for the anisotropic hyperfine parameter. In addition to that, the eigenvalues of the  $A$ -tensor,  $A_X$ ,  $A_Y$ ,  $A_Z$ , are reported.  $\Theta$  is the angle between  $Z$  and the  $[110]$ -axis. The difference between experiment and theory is given by  $\Delta$ . For completeness we also mention the results from a self-consistent, semi-empirical tight-binding (tb) calculation [120] for the hydrogen-vacancy db-defects.

comparison to bulk silicon whereas the corresponding bond angles are larger. Thus the db-atom is essentially pressed into the network. Such a tendency can also be seen for the  $V(\text{SiH})_3$  db-model, for which all defect neighbors actually move away from each other due to the small space in the vacancy. In this case, the relaxed defect symmetry is  $C_{3v}$ , and the db-geometry is again rather planar. For the  $V(\text{Si}_3\text{H})$  and  $V(\text{Si}_3\text{P})$  db-model one obtains the experimentally observed  $C_{1h}$  defect-symmetry [105] as well as the formation of a long Si-Si bond with a length of 3.08 Å and 2.95 Å, respectively. The relaxation corresponds in both cases to a pairing JT-distortion with the larger defect-neighbor distance being 3.67 Å and 3.59 Å, respectively. The db-atom remains essentially at the bulk lattice site. However, whereas the SiH group of  $V(\text{Si}_3\text{H})$  moves outwards, the phosphorus atom of the  $V(\text{Si}_3\text{P})$  db-model relaxes towards the defect center. The db-geometry of both models is not uniform with respect to the backbond neighbors. On average the angles are smaller compared to the  $V(\text{SiHO})$  and  $V(\text{SiH})_3$  model. This is also reflected in the hyperfine parameters as we will discuss below.

We note in passing that the relaxation pattern is rather insensitive to the computational details. At first glance, this is surprising, since the modelling of the monovacancy shows the opposite tendency [97, 98, 99, 122]. Apparently the presence of an impurity stabilizes the JT-distortion.

We compare in Table 4.3 the results of our  $g$ -tensor calculations with experimental data. The overall agreement is on the same order as the above mentioned methodological differences between the GIPAW- and the all-electron calculation for small molecular systems. In general, the theoretical eigenvalues tend to underestimate the experimental ones, and the differences are slightly larger for the systems with a JT-distortion. The angle  $\Theta$  between  $Z$  and the [110]-axis shows a negligible deviation for the  $V(\text{SiHO})$  defect and a large one for the  $V(\text{Si}_3\text{H})$  defect. The  $g_{\text{Iso}}$ -value has a smaller variation among different db-defects compared to surface db-defects [123]. Besides this one can clearly see how the JT-distortion affects the  $g$ -tensor. First, it breaks the uniaxial symmetry observed for the  $V(\text{SiHO})$  and  $V(\text{SiH})_3$  model. This is intuitively clear, since the bonding state lowers the electronic symmetry, which is crucial for the  $g$ -tensor [30, 31]. Secondly, the  $Z$ -axis is oriented differently for the JT-distorted systems, since  $\Theta$  is larger than the ideal value ( $35.3^\circ$ ) for the  $V(\text{SiHO})$  model but smaller for the  $V(\text{Si}_3\text{H})$  and  $V(\text{Si}_3\text{P})$  defect.

The calculated hyperfine tensor agrees very well with experiment (see Table 4.4) with an error on the order of 10 MHz for the isotropic coupling and a practically vanishing one for the anisotropic coupling. The larger discrepancy for the  $a$ -parameter is expected, since this quantity depends on the spin density  $\rho(r)$  close to the nucleus [30], whereas the  $b$ -parameter is an inherently integrated quantity [30, 40]. Consequently, the isotropic parameter should also be more sensitive to differences in  $\rho(r)$ . Interestingly, the agreement between theory and experiment is much better than expected from the pure theoretical error bar derived from our molecular test systems. We attribute this to a less pronounced effect of core polarization in the crystalline environment, since the spin density is able to delocalize into the network and it is consequently smaller in magnitude at the db-atom. The variation in the hyperfine parameters among the considered models is larger than for the surfaces [123], which can be explained by the larger

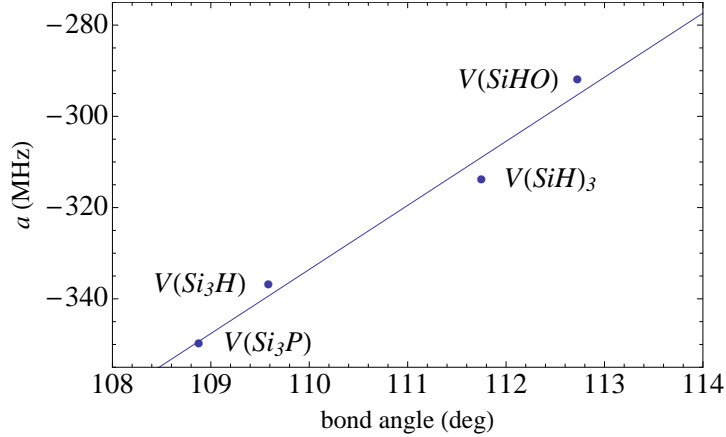
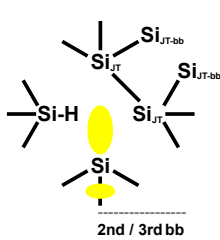


Figure 4.4: The relation between the isotropic hyperfine constant and the mean bond angle between the db-atom and its backbond neighbors. The trend follows the expectation of  $sp$ -hybridization of the db-orbital (as discussed in detail in Section 4.4). The bond lengths among the db-models vary insignificantly (on the order of 0.02 Å).

variations in the db-geometry as well as the effect of the long Si-Si bond in the case of the JT-distorted systems. The  $a$ -parameter indicates the  $s$ -like character of the wavefunction [40], which in turn is related to the bond angle between the db-atom and the backbond atoms (Figure 4.4). As visible, the coupling becomes smaller with increasing bond angle in agreement with the  $sp$ -hybridization picture of the db-orbital. However, one does not observe a corresponding increase of the  $b$ -parameter (which probes for the  $p$ -like character in  $sp$ -bonded systems like silicon), since this quantity is more affected by the long Si-Si bond in the case of the JT-distorted systems (Table 4.4) as expected from its stronger spatial dependence on the defect surrounding compared to  $a$ . It is interesting to note that the JT-distortion has no effect on the symmetry and the orientation of the  $A$ -tensor. Overall these findings clearly show that the  $g$ -tensor is sensitive to the electronic structure beyond the spin-carrying db-orbital, and the hyperfine tensor to the local spin-density distribution.

It is also illuminating to consider the superhyperfine coupling of neighbors because it gives a better understanding of the spin distribution within the network. For that purpose we list the isotropic hyperfine coupling of relevant Si atoms in Table 4.5. First, we recognize that the net coupling between the atoms forming the weak bond is almost the same for the  $V(Si_3H)$  and  $V(Si_3P)$  model. The rather small value agrees well with the expectation of a long Si-Si bond between both atoms. Furthermore, for the  $V(Si_3P)$  defect, there is again excellent agreement with the experimental value  $a_{Exp} = 37$  MHz [42], with the difference thus being only 5 MHz. This again proves that we are able to reproduce the measured defect geometry unambiguously. From the results it is also obvious that some spin leaks out into the local environment of the weak Si-Si bond, since each atom has one neighbor with a significant isotropic coupling. Besides these effects specific to the  $V(Si_3H)$  and  $V(Si_3P)$  model, one obtains in general a strong superhy-



<i>atom</i>	$V(\text{SiHO})$	$V(\text{SiH})_3$	$V(\text{Si}_3\text{H})$	$V(\text{Si}_3\text{P})$
Si (JT)	-	-	-40 (2)	-40, -42
Si (JT-bb)	-	-	-24 (2)	-28 (2)
Si (H)	-25	-11, -12 (2)	-4	-
Si (2nd-bb)	-31, -35 (2)	-35 (3)	-29, -32 (2)	-29, -31 (2)
Si (3rd-bb)	-21 (3)	-17, -18 (2)	-14, -15 (2)	-13, -14 (2)

Table 4.5: On the left side: Illustration of the characteristic defect atoms for the  $V(\text{Si}_3\text{H})$  model. Two vacancy neighbors [Si (JT)] form a long Si-Si bond. Each bond partner has one backbond neighbor with a significant isotropic coupling [Si (JT-bb)]. One vacancy neighbor is passivated by hydrogen [Si (H)]. Further characteristic atoms are located at the backbond side of the dangling bond [Si (2nd-bb), Si (3rd-bb)]. On the right side: Table listing the corresponding isotropic hyperfine couplings for the db-models considered in this section. The number of Si-atoms is given in brackets.

perfine coupling on the second backbond neighbors of the db-atom, which has already been observed in previous studies [123, 124]. For the  $V(\text{Si}_3\text{H})$  model, the deviation from experiment [125] is again rather small (3 MHz). Overall, the isotropic coupling at the backbonds is determined by the bond angle at the db-atoms. The larger the bond angle (see Figure 4.4), the larger the isotropic hyperfine coupling at the backbonds. This observation is in agreement with the expectation that for large bond angles more spin density is pressed into the network.

For completeness we mention that the hyperfine parameters for the hydrogen and phosphorus atom are also close to their experimental counterparts. In the case of hydrogen it is important to use a functional based on the general-gradient approximation [126] to obtain a reasonable isotropic coupling constant. For the  $V(\text{SiHO})$  defect (the only model with a significant  $a$ -coupling) it then differs by 1 MHz compared to the experimental value [41], whereas the  $b$ -parameter shows a discrepancy of about 0.6 MHz. The hyperfine interaction of the phosphorus atom [42] is also reproduced well by theory (the difference is practically vanishing).

Concerning the relative orientation of the  $g$ - and  $A$ -tensor, it is interesting to note that they are perfectly aligned (the angle  $\alpha$  between  $g_Z$  and  $A_Z$  is zero) only for the  $V(\text{SiH})_3$  defect with  $C_{3v}$ -symmetry. For the  $V(\text{SiHO})$  and  $V(\text{Si}_3\text{P})$  defect with  $C_{1h}$ -symmetry, both tensors have slightly different orientations with  $\alpha$  being  $4.45^\circ$  and  $4.80^\circ$  respectively. The  $V(\text{Si}_3\text{H})$  has an even larger angle ( $\alpha = 8.22^\circ$ ). In particular the deviation for the  $V(\text{SiHO})$  db-model is remarkable, since it shows that collinearity is not always fulfilled when both tensors are uniaxial.

In this section we have established the convergence of the input parameters. Additionally we have compared the GIPAW-formalism with an all-electron approach and with experiment. In particular the excellent agreement between our theoretical method and experiment is remarkable ( $\Delta g_{Iso} = 0.001$ ,  $\Delta a = 3\%$ ,  $\Delta b = 3\%$ ), so that we conclude

<i>radical</i>	$g_{Iso}$	$g_X$	$g_Y$	$g_Z$	$A_{X/Y}$ (MHz)	$A_Z$ (MHz)	$a$ (MHz)	$b$ (MHz)
SiH <sub>3</sub>	2.0038	2.0046	2.0046	2.0022	-484	-743	-535	-86
Si <sub>2</sub> H <sub>5</sub>	2.0043	2.0065	2.0044	2.0021	-357	-611	-442	-85
Si <sub>5</sub> H <sub>7</sub>	2.0049	2.0076	2.0052	2.0020	-276	-525	-359	-83
Si <sub>4</sub> H <sub>9</sub>	2.0056	2.0075	2.0075	2.0019	-213	-457	-294	-82
<i>Experiment</i>								
a-Si:H [28]	2.0058	2.0079	2.0061	2.0034	-151	-269	-190	-39
a-Si:H [44]	2.0067	2.0080	2.0080	2.0040	-154	-305	-205	-50
a-Si:H [45]	2.0056	2.0065	2.0065	2.0039	-143	-333	-206	-63

Table 4.6: EPR-tensors for small silicon radicals. From top to bottom, hydrogen at the backbond of the dangling bond is successively replaced by SiH<sub>3</sub>-groups. Furthermore, we compare the values with experimental data on a-Si:H.

that our approach is able to characterize db-defects in crystalline silicon. Additionally we have shown that the EPR-parameters provide new insights into structure-related aspects such as the effect of a pairing JT-distortion.

## 4.3 General characteristics of the db-defect

### 4.3.1 Molecular dangling bonds

In this section we discuss the characteristics of molecular and crystalline dangling bonds. This knowledge is also crucial for understanding the actual effect of the amorphous environment in the case of the a-Si:H dangling bond. Let us start by considering the molecular db-models described in Section 4.1, which correspond to the simple experimental picture [42, 43, 44, 45] of a dangling bond with a localized wavefunction of dominant  $p$ -character.

The trends for the EPR-tensors are reported in Table 4.6. We see that the  $g_{Iso}$ -value increases with the size of the cluster. At the same time, the energy difference  $E_{Gap}$  between the highest unoccupied and the db-orbital becomes smaller (Figure 4.5(a)). This inverse trend between  $g_{Iso}$  and  $E_{Gap}$  reflects the relation between  $\mathbf{g}$  and  $E_{Gap}$  in the second-order perturbation picture (Equation (2.10)). We also recognize that  $g_Z$  successively becomes smaller the more we replace the backbond hydrogen atoms by silicon. The  $a$ -parameter also decreases with the cluster size, and for such simple systems we obtain an almost linear relation between  $a$  and  $g_{Iso}$  (Figure 4.5(b)). Furthermore, the  $b$ -parameter becomes smaller from the silyl to the tetrasilyl radical. Overall this characterizes a spin delocalization, which is related to the polarization of hydrogen. Figure 4.1(b) visualizes this effect for the tetrasilyl radical. In this illustration, only hydrogen atoms oriented along the  $A_Z$ -axis are covered with spin density thus indicating a strong isotropic coupling. To quantify this effect, let us consider Table 4.7, which shows the  $a$ -value of these hydrogen atoms. As we see the net spin polarization of

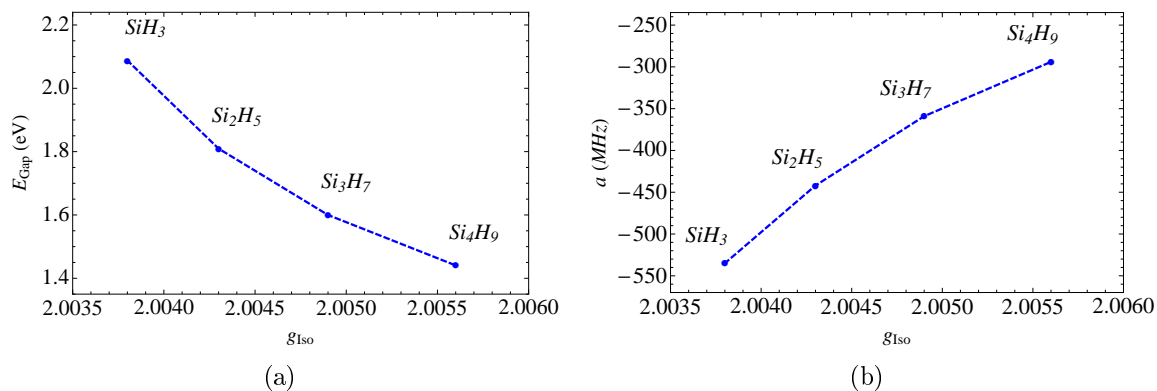


Figure 4.5: Relation between the isotropic value of the  $g$ -tensor and (a) the energy between the highest occupied and the lowest unoccupied orbital, and (b) the  $a$ -parameter respectively. From silyl to tetrasilyl, hydrogen at the backbond is successively replaced by silicon.

	#	$a$ (MHz)	$r$ (Å)	$\beta$
$\text{SiH}_3$	3	18	1.49	$72.3^\circ$
$\text{Si}_2\text{H}_5$	1	72	3.22	$47.7^\circ$
$\text{Si}_5\text{H}_7$	2	67	3.22	$50.4^\circ$
$\text{Si}_4\text{H}_9$	3	63	3.20	$52.4^\circ$ - $52.5^\circ$

Table 4.7: Significant isotropic hyperfine couplings of hydrogens oriented on the backbond side of small db-clusters. The number of atoms is given in the column marked by '#'. The distance between the hydrogen atom and the db-atom is denoted by  $r$ , and  $\beta$  is the angle between the Si-H bond direction and the  $A_Z$ -axis of the db-atom. Note that the sign of the coupling is caused by the positive nuclear  $g_n$ -factor of hydrogen.

these hydrogen atoms increases systematically with cluster size, and their orientation with respect to the db-atom is practically the same. Thus there is a net spin transfer from the db-atom to  $A_Z$ -oriented hydrogen, which becomes more significant with the number of accordingly aligned hydrogen atoms (i.e. the cluster size), and it reduces the  $a$ -parameter on the db-atom.

The silyl and tetrasilyl radical also exemplify the textbook notion of a dangling bond. First, for these radicals both EPR-tensors are uniaxial (Table 4.6) and collinear (Figure 4.1(b)). Secondly, we can describe the db-orbital by a linear combination of atomic orbitals (Equation (2.19)). In particular, as we will discuss later on, this means that the bond-angle trend is characterized by a simple  $sp$ -hybridization picture. However, not all of these characteristics also occur for the other radicals, which have a chemically-mixed backbond configuration. The  $g$ -tensor of the  $\text{Si}_2\text{H}_5$  and  $\text{Si}_5\text{H}_7$  radical is rhombic and there is a small deviation from collinearity for the EPR-tensors (on the order of  $2^\circ$ - $3^\circ$ ).

<i>db-model</i>	$g_{Iso}$	$g_X$	$g_Y$	$g_Z$	$A_X$ (MHz)	$A_Y$ (MHz)	$A_Z$ (MHz)	$a$ (MHz)	$b$ (MHz)
$2 \times 2 \times 2$									
$V_4(\text{SiH})_9$	2.0071	2.0109	2.0109	2.0014	-233	-233	-427	-297	-65
Si(111):H	2.0070	2.0100	2.0100	2.0010	-233	-233	-427	-298	-65
$V(\text{SiHAL}_2)$	2.0156	2.0206	2.0196	2.0066	-139	-140	-262	-180	-41
$V(\text{SiP})_3$	2.0091	2.0130	2.0130	2.0013	-332	-332	-502	-389	-57
$3 \times 3 \times 3$									
$V(\text{SiHO})$	2.0059	2.0082	2.0081	2.0013	-230	-231	-414	-292	-61
$V(\text{SiH}_3)$	2.0074	2.0108	2.0108	2.0005	-253	-253	-434	-314	-60
<i>Experiment</i>									
a-Si:H [28]	2.0058	2.0079	2.0061	2.0034	-151	-151	-269	-190	-39
a-Si:H [44]	2.0067	2.0080	2.0080	2.0040	-154	-154	-305	-205	-50
a-Si:H [45]	2.0056	2.0065	2.0065	2.0039	-143	-143	-333	-206	-63

Table 4.8: EPR-tensors for crystalline db-models in 64-atom supercells (without the defect) and 216-atom supercells (without the defect, taken from Section 4.2.3) in comparison to experimental values for a-Si:H.

Finally, does the tetrasilyl radical indeed describe well the experimental results for a dangling bond in a-Si:H? From our results (Table 4.6) we conclude that the cluster model is able to reproduce the characteristics only in parts. For example, since the structure is symmetric, its  $g$ -tensor does not show the recently observed rhombicity [27, 28]. Despite that, the theoretical hyperfine parameters are too large and indicate a too strong localization of the spin density. This aspect is remarkable since the relaxed geometry of the radical is already close to planar (bond angles are around  $116^\circ$ ). Thus it is not possible to overcome the discrepancy between theory and experiment by changes in the local geometry alone (further details are given in Section 4.4.1). Consequently, a small db-model (such as the tetrasilyl radical) is insufficient for characterizing the a-Si:H dangling bond as assumed in previous studies [44, 45, 127, 128]. The influence of the defect surrounding plays an important role and its effect can only be captured by network models to which we will turn in the next subsection.

### 4.3.2 Crystalline dangling bonds

We use  $2 \times 2 \times 2$  supercells (defect-free: 64 silicon atoms) for the db-models described in Section 4.1. Furthermore, we include the already discussed findings for the  $V(\text{SiHO})$  and  $V(\text{SiH}_3)$  db-model carried out in  $3 \times 3 \times 3$  supercells (defect-free: 216 silicon atoms). The dangling bond at the H-passivated Si(111) surface is modeled by a  $2 \times 2$  slab consisting of 8 layers of silicon atoms, where we only relax the surface atoms. To remove the artificial interaction with periodic images we also include a sufficiently large vacuum layer (9 layers). For the  $g$ -tensor it is important to keep in mind that there is a supercell effect on the order of  $10^{-3}$  (Table 4.1). However, this accuracy is sufficient for our purposes,

in particular, since we are more interested in the less sensitive hyperfine tensor.

Again let us first look at the general trends among the db-models (Table 4.8). We recognize that essentially all of them have uniaxial  $g$ - and  $A$ -tensors. The only exception is the  $V(\text{SiHAL}_2)$  defect with a rhombic  $g$ -tensor. However the corresponding db-state is close to the valence-band maximum as e.g. visible from the  $g_{iso}$ -value [129]. Therefore it should also couple to a larger number of orbitals, and this complex coupling can easily reduce the symmetry of  $\mathbf{g}$ . The isotropic  $g$ -value of the other localized db-models varies by 0.003 but e.g. the defects with only hydrogen are grouped together in a smaller interval. Thus the chemical environment marks an important influence on  $g_{Iso}$ . Furthermore, we note that  $g_Z$  is smaller than the free-electron value 2.0023 for these db-models.

The  $a$ -parameter of the localized db-models is relatively constant at around -300 to -400 MHz, with the  $b$ -parameter in between -57 to -65 MHz. The bond parameters of the db-atom reflect this rather small variation. The bond lengths deviate by only 0.03 Å, and the bond angles by up to 3.4° from the tetrahedral angle. This rather homogeneous picture also holds for the spin distribution in the network. Among the models, the second-nearest neighbors show the strongest isotropic superhyperfine coupling on the order of -30 to -40 MHz (10%). The EPR-tensors for the db-models with only hydrogen are collinear. But for the other db-models ( $V(\text{SiHAL}_2)$ ,  $V(\text{SiHO})$ ,  $V(\text{SiP})_3$ ) deviations occur and they are therefore related to the presence of the corresponding impurities and the lower defect symmetry.

The comparison between the theoretical molecular and crystalline dangling bonds reveals two interesting aspects. The  $g_{Iso}$ -value of the cluster models is in general smaller than for the crystalline db-defects. This can be explained by their larger (HOMO-LUMO) gap, which causes smaller deviations from the free-electron value (Equation (2.10)). Secondly, the tetrasilyl radical has a lower isotropic and a larger anisotropic hyperfine coupling compared to the crystalline models. As we will discuss in Section 4.4.2, this is caused by the defect geometry and can be understood by an  $sp$ -hybridization picture of the db-orbital.

Finally, let us turn to the question of how accurate such db-models can describe the EPR-parameters of the a-Si:H dangling bond. For the  $g$ -tensor we see from Table 4.8 that the crystalline models tend to have larger values. Furthermore, they also do not capture the observed rhombicity. The  $a$ -parameter of the crystalline db-models is by about 100 MHz larger than the experimental finding but as mentioned before more-or-less constant among different theoretical models. On the other hand, the  $b$ -parameter deviates among different measurements too much to be conclusive. However, both hyperfine parameters together show that theory points to a higher degree of spin localization as observed in experiment. In this context it is interesting that the db-atom has sufficiently small hyperfine couplings in the case of  $V(\text{SiHAL}_2)$ . However the  $g$ -values clearly show the different driving forces behind the delocalization. For the  $V(\text{SiHAL}_2)$  defect it is caused by the hybridization of the db-orbital with valence-band states. On the contrary, the delocalization mechanism in a-Si:H preserves the mid-gap character of the defect.

In conclusion, vacancy-based c-Si dangling bonds can be used to study the influence of the further defect surrounding and they have a relatively characteristic EPR-fingerprint.

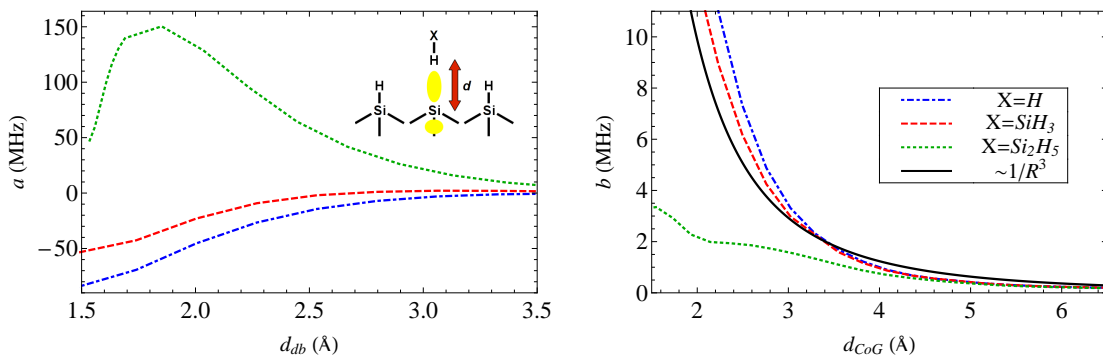


Figure 4.6: Distance dependence of the hyperfine parameters of hydrogen on top of a Si(111)-surface. Three different molecules ( $\text{H}_2$ ,  $\text{SiH}_4$ ,  $\text{Si}_2\text{H}_6$ ) are considered. The disilane molecule is oriented in such a way so that the three hydrogen atoms are actually separated from the db-atom by the same distance  $d$ . The distance  $d_{db}$  is measured from the db-atom, and  $d_{CoG}$  from the center-of-gravity of the spin density. The black line denotes the point-dipole approximation according to Equation (2.18).

However they do not capture all features of the a-Si:H dangling bond and differ most notably by a higher degree of spin localization.

### 4.3.3 Hydrogen

We have seen that backbond hydrogen can have a significant spin polarization. Therefore it is interesting to ask, whether the same effect is also observable on the opposite side. To answer this question we consider H-containing molecules over the dangling bond on a hydrogenated Si(111)-surface (Section 4.3.2). For the molecule we use the dihydrogen-, the silane- (with one Si-H bond aligned to the  $z$ -direction), and the disilane molecule (with three of the hydrogens spanning a plane parallel to the surface). We compute the distance dependence of the hyperfine parameters for a fixed surface geometry to remove structural effects. However, we have also checked the trends for relaxation and they lead to the following intuitive picture. The closer the molecule gets to the dangling bond the more this atom is pressed into the network, thus the db-geometry becomes planar. The influence of such a bond-angle variation will be studied systematically in Section 4.4.2.

Figure 4.6 shows that minority spin density builds up at the hydrogen atom the closer it gets to the dangling bond in the case of the dihydrogen and silane molecule. The upper hydrogen of the  $\text{H}_2$  molecule has a significant majority spin polarization and the corresponding isotropic coupling is on the order of several hundred MHz. Similarly, the  $a$ -parameter of the silicon atom of the  $\text{SiH}_4$  radical increases for  $d_{db} \rightarrow 1.5 \text{ \AA}$ . Only for the disilane molecule, we observe a (majority) spin polarization of the closest hydrogen atoms. Overall the conclusion is that hydrogen can be polarized for small distances from the db-atom. However the results strongly depend on the atoms to which the closest

hydrogen is bound to and there is no unique trend.

Experimentally the point-dipole approximation (Equation (2.18)) is used for estimating the distance  $d_{CoG}$  between the closest hydrogen atom and the center-of-gravity of the spin density [41, 130]. However, the range of applicability is unclear, and our systematic study actually clarifies this open question. As we see from Figure 4.6, the anisotropic coupling of the hydrogen atom agrees well with the classical picture for  $d_{CoG} > 2.8 - 3.5$  Å. In this case, the point-dipole approximation yields a good estimate for the spatial separation between the hydrogen atom and the dangling bond.

## 4.4 Bond-parameter trends of EPR-parameters

### 4.4.1 Bond-parameter dependence of the tetrasilyl radical

So far we have only discussed the phenomenology of our molecular and crystalline models. However, their true value consists in providing a homogeneous environment for studying systematically the effect of changes in the local db-geometry on the EPR-parameters. Such conceptual investigations are particularly useful for the interpretation of the EPR-parameters in a-Si:H, where the defect geometry is far more complex.

Let us start by considering the tetrasilyl radical, which is the simplest db-system with a Si<sub>3</sub> backbond configuration. For the study of the bond-length dependence of the EPR-parameters, we systematically vary the distance between the db-atom and its three neighbors for three different, fixed bond angles (as depicted in Figure 4.7). For the bond-angle dependence, we carry out the following procedure to minimize the accompanied change in the bond lengths. First we move the db-atom perpendicular to the plane spanned by its neighbors. In a second step we relax the system with S/PHI/nX (with a PBE XC-Functional, Troullier-Martin pseudopotential) with the constraint that all atoms can change their positions only along the bond lengths  $l$ . Thanks to this procedure,  $l$  only varies by 0.06 Å from the tetrahedral to the planar configuration.

Figure 4.7 shows the bond-length dependence of the  $g$ -tensor. We see that the normal  $g$ -tensor component linearly decreases the more we stretch the radical. This trend becomes more pronounced the larger the bond angle. In an interval of about 10% of the relaxed bond length  $l_0$ , we can describe this by

$$g_{\perp}(l) = k_g(l_0 - l) + g_0$$

where  $k_g = 0.0038, 0.0047, 0.0054$  (1/Å) and  $g_0 = 2.0083, 2.0074, 2.0073$  for  $\alpha = 109.5^\circ, 115.9^\circ, 120^\circ$  respectively. Notably, this trend cannot be related directly to the energy gap between the db-orbital and the lowest unoccupied orbital (or the other orbitals). A linear  $l$ -dependence is also found for the isotropic hyperfine coupling (Figure 4.8) in the range of 1.8 and 2.3 Å, i.e.

$$a(l) = k_a(l_0 - l) + a_0$$

with  $k_a = -272, -284, -149$  (MHz/Å) and  $a_0 = -477, -294, -135$  MHz for  $\alpha = 109.5^\circ, 115.9^\circ, 120^\circ$  respectively. Thus the gradient is stronger for a non-planar db-geometry. Overall

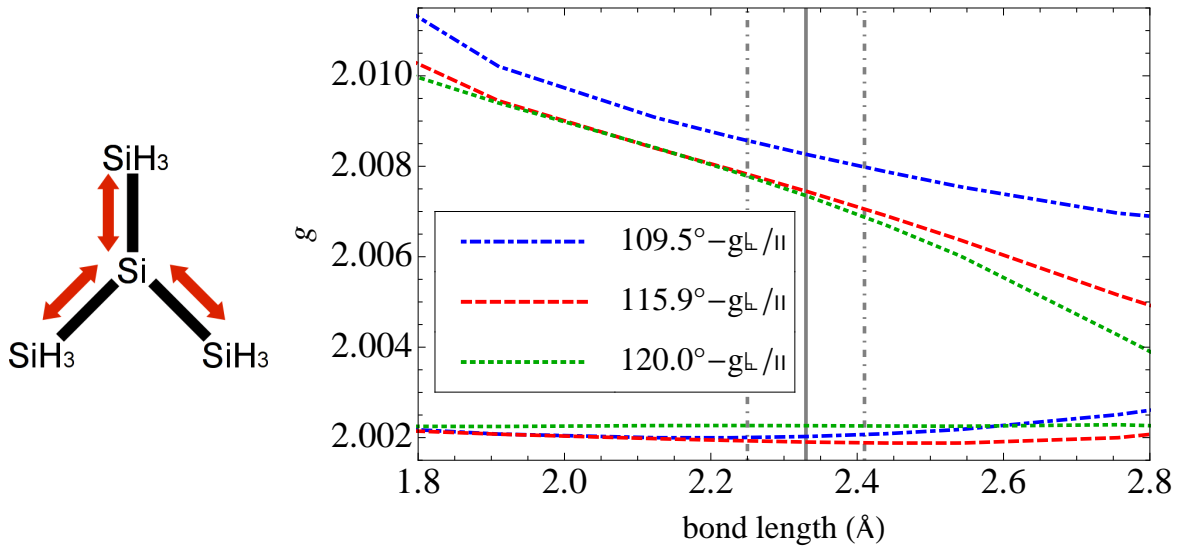


Figure 4.7: Relation between the bond length  $l$  and the eigenvalues of the  $g$ -tensor for the tetrasilyl radical for three different bond angles. The gray line indicates the relaxed bond length  $l_r$ , and the dot-dashed lines a variation of about 4% with respect to  $l_r$ .

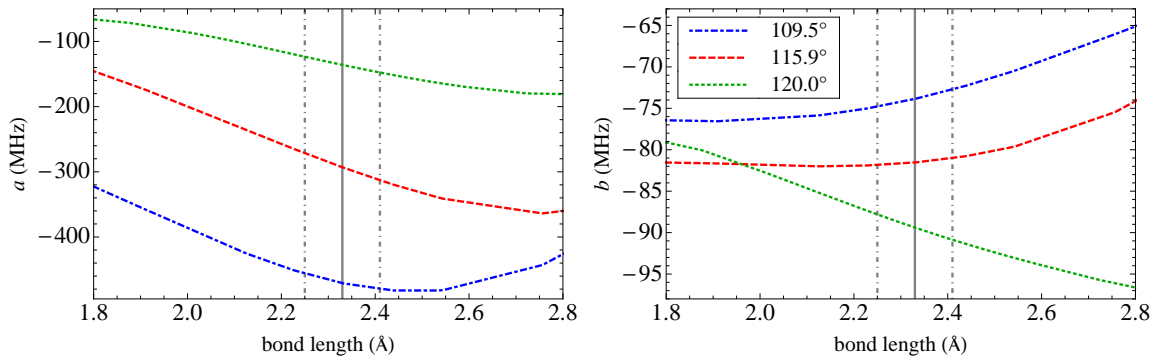


Figure 4.8: Relation between the bond length  $l$  and the hyperfine parameters for the tetrasilyl radical for three different bond angles. The gray line indicates the relaxed bond length  $l_r$ , and the dot-dashed lines a variation of about 4% with respect to  $l_r$ .

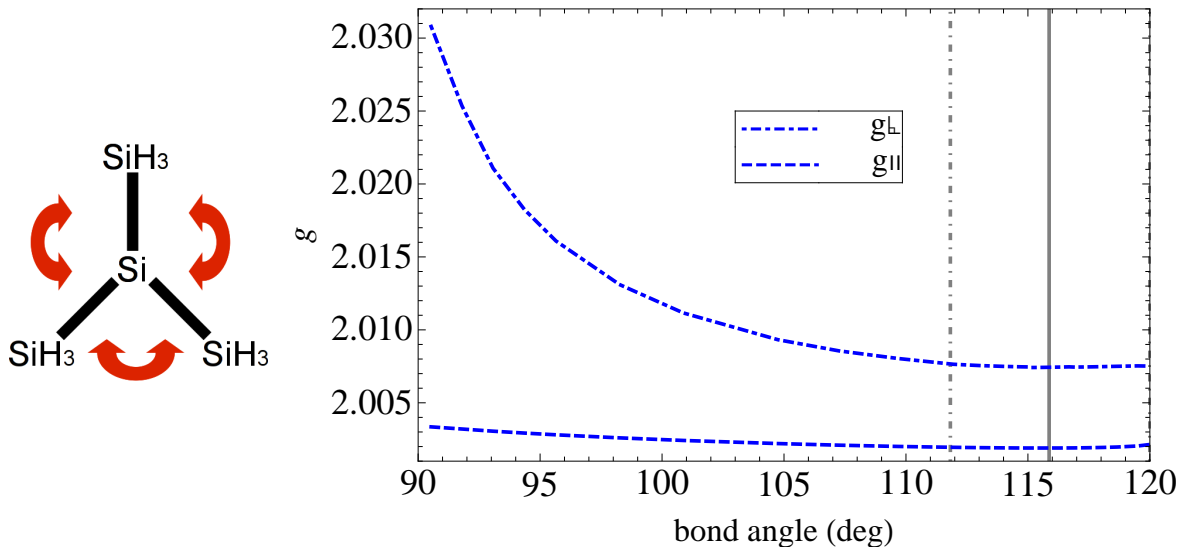


Figure 4.9: Relation between the bond angle  $\alpha$  and the eigenvalues of the  $g$ -tensor for the tetrasilyl radical. The gray line indicates the relaxed bond angle  $\alpha_r$ , and the dot-dashed lines a variation of about 4% with respect to  $\alpha_r$ .

the trends for the hyperfine parameters depend on the db-orbital character and the already discussed spin-polarization effect of hydrogen oriented along  $A_Z$ . The db-orbital for the non-planar geometry becomes more  $s$ -like with increasing bond length for  $l$ -values not larger than 7-18% whereas the  $b$ -parameter decreases at the same time. For hydrogen aligned to  $A_Z$ , the stretching of the radical has the effect that the spin polarization becomes smaller due to the movement away from the spin density. Consequently the coupling between these hydrogen atoms and the dangling bond reduces with increasing  $l$  and this explains the trends at the db-atom. The db-orbital is purely  $p$ -like<sup>4</sup> in the planar configuration and thus there is essentially an increase in the  $b$ -parameter for tensile strain. The coupling to the  $A_Z$ -oriented hydrogen is overall smaller due to the large bond angle. In this case one observes a rather small spin redistribution to the other hydrogen atoms for larger  $l$ -values. For all bond angles, we essentially obtain a build-up of majority spin density on the silicon db-neighbors the more we stretch the radical and this is caused by the breaking of the Si-Si bond.

The bond-angle dependence of the  $g$ -tensor is illustrated in Figure 4.9. It shows that the parallel component of  $\mathbf{g}$  falls off gradually with bond angle  $\alpha$ . Quantitatively the  $g$ -tensor is more sensitive to changes in  $\alpha$  than  $l$ . The trend can be explained by the energy difference between the LUMO and HOMO, which increases with bond angle thus causing smaller  $g$ -values (Equation (2.10)). The admixture of  $s$ -character to the db-orbital lowers the energy of the corresponding state and therefore the difference to the

<sup>4</sup>In a planar configuration ( $\alpha = 120^\circ$ ), the Si-Si bond orbitals are  $sp^2$ -hybrids [9, 39, 131] while the db-orbital is a pure  $p$ -state. At the tetrahedral angle ( $\alpha = 109.5^\circ$ ) the backbond orbitals and the db-orbital are equivalent  $sp^3$ -hybrids (25%  $s$ , 75%  $p$ ).

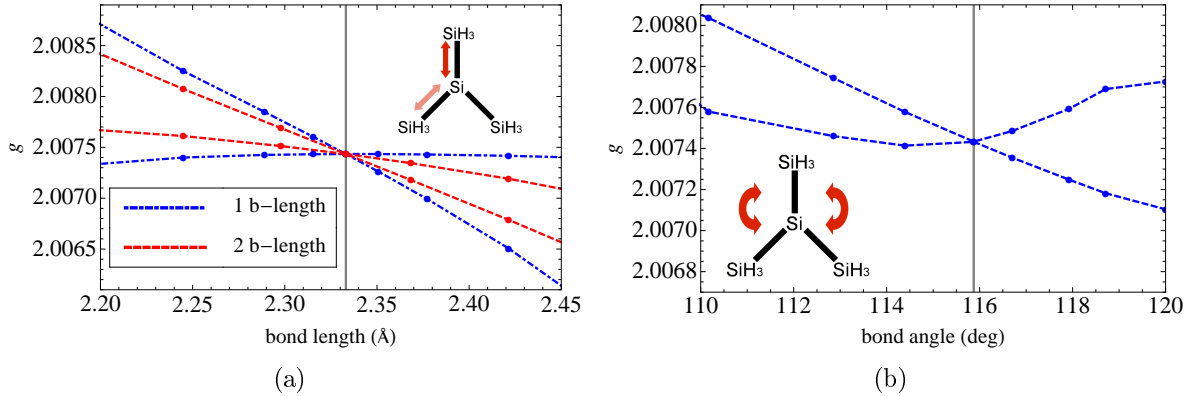


Figure 4.10: Rhombicity of the  $g$ -tensor for the tetrasilyl radical. In (a) one and two bond lengths are changed and in (b) two angles are changed by the same magnitude ( $\alpha_1 = \alpha_2$ ). The lines indicate  $g_X$ ,  $g_Y$ , and the gray line the relaxed bond parameters.

bonding states. This simple energetic picture is completed by the hyperfine parameters, which we will discuss and compare in the next subsection with the crystalline db-models. For completeness, we mention that a comparable dependence of the  $g$ -tensor has also been obtained with a tight-binding approach [132]. However this study predicts a larger deviation of  $g_Z$  from the free-electron  $g$ -value with  $\alpha$ .

As mentioned, a recent a-Si:H multifrequency EPR-study [27, 28] indicated a rhombic  $g$ -tensor, whereas it is uniaxial for our localized crystalline db-models (Table 4.8). The tetrasilyl radical is an ideal test system to investigate how changes in the bond parameters can lower the symmetry of the  $g$ -tensor. For that purpose, we elongate the molecule either by varying one or two bond lengths or two bond angles (so that these two angles remain the same) respectively. The results are reported in Figure 4.10, and they essentially illustrate that fluctuations in the bond parameters can indeed cause a rhombic  $g$ -tensor. Quantitatively, the corresponding deviation between  $g_X$  and  $g_Y$  is on the order of a few 1/1000ths. The trend is slightly stronger when we only change one of the lengths instead of two simultaneously. In principle it would also be possible to study the effect of more complicated bond-parameter distortions systematically. However this would not add further insights into the rhombicity of the  $g$ -tensor. The important message here is that such fluctuations in the local bond parameters reduce the symmetry of the  $g$ -tensor.

#### 4.4.2 Bond-angle dependence of c-Si models

Small clusters are ideal to study the effect of the local bond geometry on the EPR-parameters [46, 128, 133]. However they cannot capture the effect of the further defect surrounding. For that reason we now turn to a conceptually similar study for selected crystalline db-models. Here we focus on the hyperfine parameters, which yield the relevant information on the spin distribution in the network.

To study the influence of the bond angle on the hyperfine parameters, we again consider  $2 \times 2 \times 2$  supercells using the following relaxation scheme. First we displace the db-atom from its lattice position. We then relax only the backbond atoms so that the bond length fluctuates only by  $0.06 \text{ \AA}$  at the most. This scheme is carried out for all models at the ideal lattice structure to make the comparison independent of other geometrical effects. Only the hydrogen atoms are relaxed to recover the correct Si-H bond length to ensure that the corresponding bonding states are well below the valence-band edge. To reduce the erroneous occupation of defect resonances below the topmost valence band, we use a  $7 \times 7 \times 7$   $\mathbf{k}$ -point grid. An alternative strategy to circumvent this problem consists in using a smearing function [87].

The bond angle  $\alpha$  determines the  $sp$ -hybridization at the db-center. As discussed in the previous section, the db-orbital becomes purely  $p$ -like for  $120^\circ$ . For the hyperfine parameters this implies that the dipolar coupling increases with  $\alpha$  whereas the  $a$ -parameter decreases at the same time. Indeed, such trends are obtained for the tetrasilyl radical (Figure 4.11) but significant deviations occur for some of the crystalline db-models. For small bond angles, both hyperfine parameters decrease, indicating a delocalization of the spin away from the db-atom. This effect can be rationalized as follows. The variation of the bond angle does not just influence the  $sp$ -hybridization but it also affects the energetic position of the db-level. With respect to a pure  $p$ -orbital, an admixture of  $s$ -character implies a lower energy. However, as the db-level approaches the valence-band edge, it starts to hybridize with the network states and to delocalize. At which angle this occurs depends on the original position of the state in the relaxed configuration and thus on the chemical environment of our models. Electronegative elements such as phosphorus raise the db-level due to Coulombic repulsion, and thus delocalization comes into play only at small bond angles. Electropositive elements like aluminum, on the other hand, pull the level close to the valence band. Therefore, the singly occupied level is delocalized already for bond angles slightly below  $120^\circ$ . Note that this effect is largely absent in small cluster models, since quantum confinement increases the gap between the occupied and unoccupied states.

For further illustration let us look at the partial density-of-states defined by

$$D(E) = \int \sum_n \delta(E - \epsilon_n(\mathbf{k})) \sum_{i=s,p} |\langle \psi_n(\mathbf{k}) | \phi_i \rangle|^2 d\mathbf{k} \quad (4.1)$$

where  $\psi_n(\mathbf{k})$  and  $\epsilon_n(\mathbf{k})$  correspond to the wavefunctions and eigenvalues obtained from the pseudopotential calculation, and  $\phi_i$  to projector functions constructed from the atomic partial waves [40].

For the actual implementation into S/PHI/nX, we replace the integral in Equation (4.1) by a sum and the  $\delta$ -function by a Gaussian (broadening  $0.1 \text{ eV}$ ). Figure 4.12 shows the spin-resolved density-of-states  $D^\uparrow$  (majority spin) and  $-D^\downarrow$  (minority spin) for three characteristic models and three bond angles respectively. One can clearly see the downshift of the defect levels with decreasing bond angle for the  $V(\text{P}_3)$  and  $V_4(\text{SiH})_9$  db-model. If the level falls below the valence-band maximum due to the chemical environment, i.e. for the  $V(\text{Al}_2\text{SiH})$  model, the features are broadened and ultimately disappear.

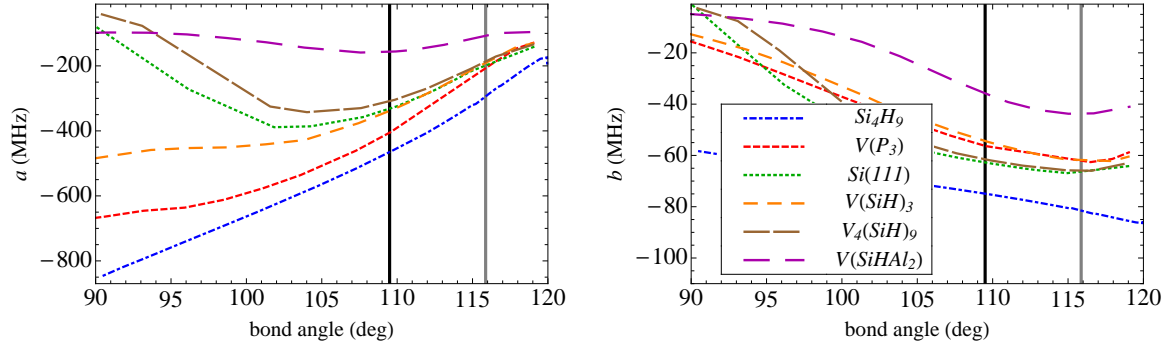


Figure 4.11: Dependence of the hyperfine parameters on the variation of the bond angle for the  $\text{Si}_4\text{H}_9$  molecule and the c-Si db-models. The black line marks the relaxed bond angle of the c-Si db-models and the gray line of the  $\text{Si}_4\text{H}_9$  molecule.

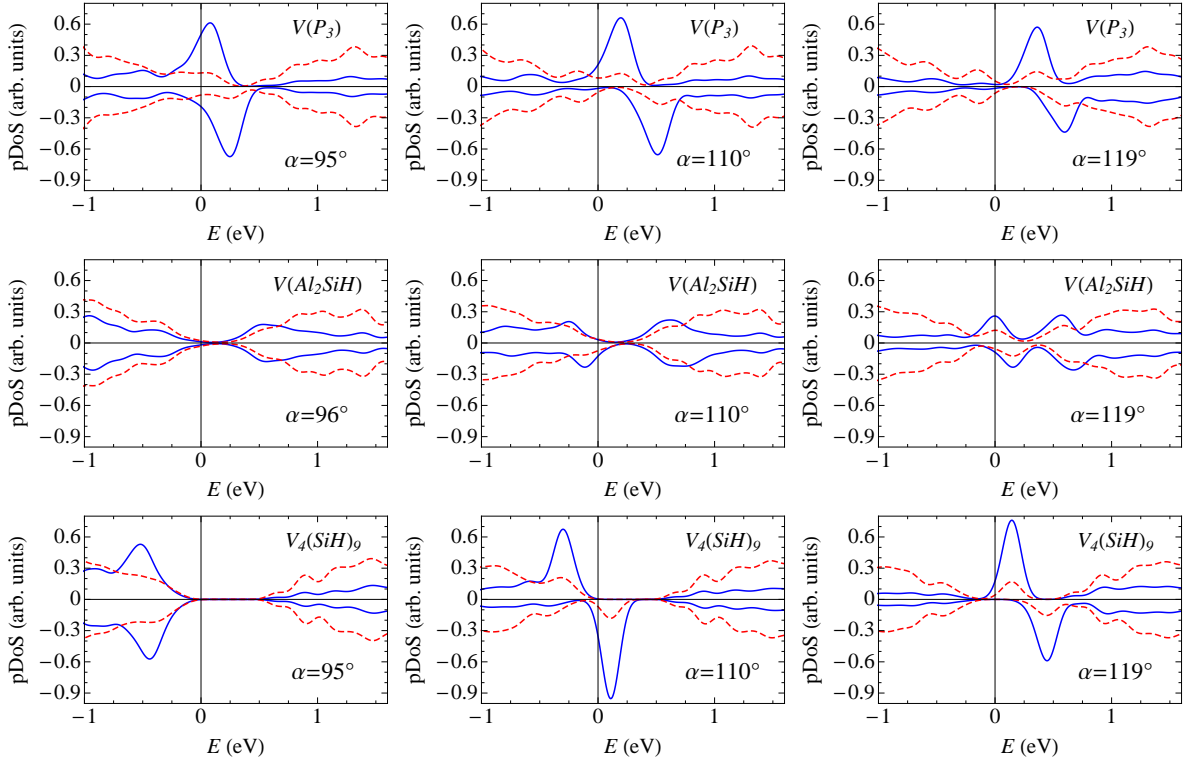


Figure 4.12: Illustration of the delocalization mechanism. Calculation of the projected density-of-states  $D(E)$  as implemented in S/PHI/nX for three different bond angles  $\alpha$  and for three different db-models. For clarity, we plot  $D^\dagger(E)$  and  $-D^\downarrow(E)$  separately. The dashed line indicates the scaled total density-of-states (scaling factor 0.035). The energies are aligned to the valence-band maximum of c-Si.

An *ab initio* study on small clusters [46] has shown that the empirical LCAO-picture is not accurate enough to distill the bond-angle range [45] from the hyperfine parameters alone. However, these models cannot capture the effect of delocalization due to the width of the band gap and the small number of neighbors. The crystalline db-models do not have these limitations and it is therefore elucidating to consider the relation between the hyperfine parameters and the bond-angle range with respect to this question. For this we consider again amorphous silicon, for which theory [134, 135] and experiment [136, 137, 138] estimate bond-angle variations of up to  $15^\circ$ . Considering an interval of  $\pm 8\%$  around the tetrahedral bond angle, one obtains the following characteristics for the change of  $a$  and  $b$ . Within a non-self-consistent, single-site LCAO-model [45], where the dangling bond is restricted to the under-coordinated Si atom only, the isotropic parameter varies by 55–80% and the anisotropic parameter by 18–27%. In comparison to that, we get from our DFT-calculations for a delocalized defect, i.e. the  $V(\text{Al}_2\text{SiH})$  db-model, a variation on the order of 21–41% for the  $a$ -parameter and 18–59% for the  $b$ -parameter. For a localized model, i.e.  $V(\text{P}_3)$ , there are dramatical fluctuations of the isotropic hyperfine parameter with bond angle (by 44–66%) whereas the  $b$ -parameter varies by 8–31%. This quantitatively illustrates that the isotropic hyperfine parameter is more sensitive to changes in the local structure for deep-level defects. Furthermore, it shows that the single-site LCAO-model overestimates in particular the change of the isotropic hyperfine coupling and therefore predicts a smaller bond-angle range for a given  $\Delta a$ -interval compared to self-consistent calculations.

The analysis of the superhyperfine interaction yields additional information about the defect (such as its coordination in the case of the disordered a-Si structure [139, 140]). For that reason, we consider the bond-angle dependence of the first- and second-nearest neighbors of the c-Si models (Figure 4.13). Here we focus on the isotropic coupling, which measures the spin distribution within the network. The first-nearest neighbors show the following trends. For the localized defects, a large coupling is obtained for small bond angles. With increasing bond angle one observes a change from majority to minority spin density, which is almost independent of the model. This has been observed before in the context of small molecular radicals [124] (and references therein) and can be explained by spin-polarization effects. On the other hand, the second-nearest neighbors show a continuous increase of  $a$  for larger bond angles. Pictorially speaking this corresponds to the situation that the spin density is pressed more and more into the network. Consequently, the isotropic hyperfine coupling of these atoms is mainly influenced by the db-geometry. However, the magnitude depends on the chemical environment, and it is the largest for the hydrogen-saturated vacancies. With the exception of the  $V(\text{P}_3)$  db-model, the second-nearest neighbor hyperfine coupling is in general larger than the first-neighbor one. This is in good agreement with previous findings [123, 124].

In conclusion, we have seen that the bond-angle dependence of the hyperfine parameters can be explained by two effects, namely the  $sp$ -hybridization of the db-orbital (in particular important for deep-level defects) and spin delocalization. The latter occurs for small bond angles and depends on the relative electronic position of the db-orbital with respect to the band edges.

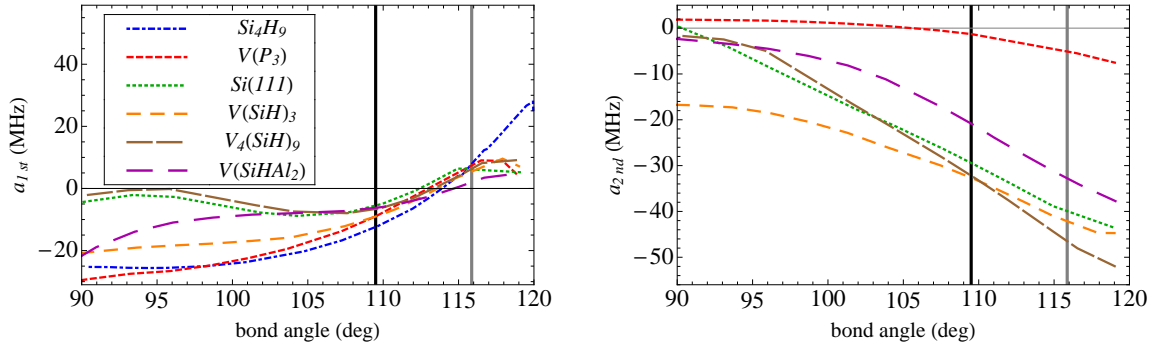


Figure 4.13: Dependence of the hyperfine parameters on the variation of the bond angle for the backbond neighbors of the  $\text{Si}_4\text{H}_9$  molecule as well as for the c-Si db-models. The black line marks the bond angle of the c-Si db-models and the gray line of the  $\text{Si}_4\text{H}_9$  molecule.

#### 4.4.3 Strain dependence of c-Si models

The systematic study of the influence of the bond angle on the hyperfine parameters gives us the possibility of tackling the more complex situation, in which both bond length and bond angle change and are correlated with each other. This investigation of the dependence of the hyperfine parameters on hydrostatic strain is also of practical relevance, since it is in principle also accessible by experiment.

We compute the hyperfine parameters for  $2 \times 2 \times 2$  supercells with the parameters as used previously. The effect of strain is modeled by rescaling the supercell with the relaxed geometry (lattice constant  $x_0$ ) at a slightly different lattice constant  $x$  and then relaxing the structure again, so that the overall force per atom is not larger than  $4 \text{ meV}/\text{\AA}$ . The strain is then given by  $(x - x_0)/x_0$ . For compressive strain we expect that at some point the band gap closes and the system becomes metallic. In this situation we could in principle apply a similar strategy as for the bond-angle dependence, i.e. use a significantly denser  $\mathbf{k}$ -point mesh. However, the notion of a localized dangling bond is no longer applicable for such strains. For that reason, we consider only an amount of strain for which we can clearly identify the db-character from the hyperfine parameters.

Typically the transition from the db- to the metallic character of the system is rather sharp, which means that a slight decrease of the lattice constant causes a dramatic drop of  $a$  and  $b$  to zero. But as visible from Figure 4.14, this happens for every model for a different amount of strain. It is clear that this result is correlated to the band gap of the corresponding db-model, since we can compress the  $V(\text{P}_3)$  much more than e.g. the  $V(\text{Al}_2\text{SiH})$  db-defect. Thus a larger band gap results in a larger stability of the db-orbital under compression. When we now increase the lattice constant, the localized db-models gradually change from a large  $s$ - to a large  $p$ -character. On the contrary, the rather delocalized  $V(\text{Al}_2\text{SiH})$  model shows a small decrease of the isotropic parameter for less than 5% deviation strain. Quantitatively, we see that for tensile strain on the

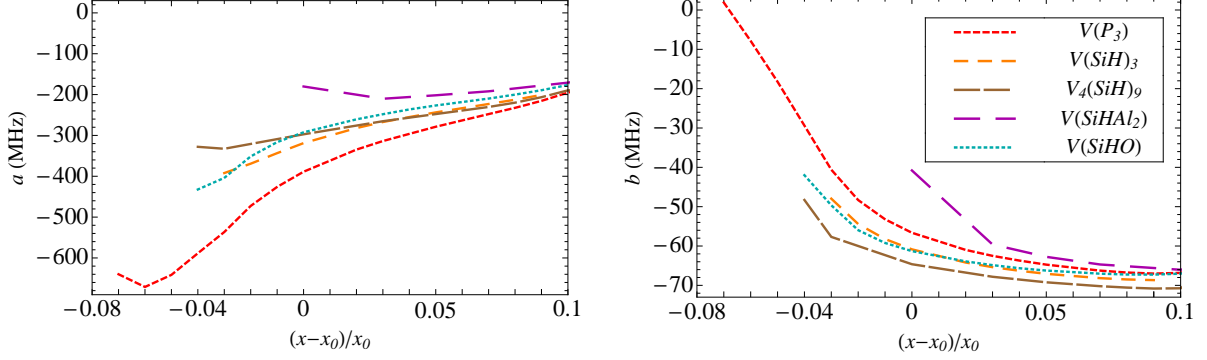


Figure 4.14: Dependence of the hyperfine parameters on strain.

order of 10%, the  $a$ -parameter of all models reaches the experimental value of a-Si:H. But the theoretically obtained hybridization picture implies a large anisotropic coupling (65-70 MHz), whereas a recent study yielded a significantly smaller one ( $b = -39$  MHz) [27, 28]. However, it should be noted that it is difficult to distill the  $b$ -coupling from the measured EPR-spectrum unambiguously due to the wide statistical variation of  $A$ -tensors (as indicated by the experimental results in Table 4.14).

To explain the hyperfine parameters in terms of the local db-geometry, let us look at the dependence of the bond parameters on strain (Figure 4.15). The bond length becomes larger the more we stretch the lattice and the bond angle becomes planar at the same time. In particular for tensile strain, the trends for the hyperfine parameters result from the bond-angle variation (Figure 4.11). However, from the latter study we have also obtained a significantly smaller  $p$ -character in case of the delocalized  $V(\text{Al}_2\text{SiH})$  defect. Therefore for this model, the significantly larger  $b$ -parameter for tensile strain has to originate from spin-localization effects due to the increase in bond length.

The  $a$ -parameter shows a rather small variation among the localized c-Si db-models (Table 4.8), which also implies that quite different db-environments result in a similar local db-geometry. However, consequently they cannot explain the lower isotropic coupling observed in a-Si:H. With respect to this open question, our results suggests strain as a possible mechanism for the down-shift of  $a$ . Indeed, such a picture has been already proposed in the context of a-Si:H previously [44, 127]. In this model, the discrepancy between the  $P_b$ -center at the Si/SiO<sub>2</sub> interface ( $a \sim -300$  MHz) and the a-Si:H dangling bond is caused by the relaxation to a more planar geometry in the latter case [28]. As is visible from our findings such a mechanism enhances the  $p$ - over the  $s$ -character. Furthermore we can quantify the necessary amount of tensile strain, which has to be on the order of 10% independent of the specific db-model. But here we have to point out that the crystalline models do not capture the asymmetry in the db-geometry [127] and therefore only represent the ideal situation. We will consider a more realistic case in the next chapter, where we will carry out an analogous study for our a-Si:H db-models.

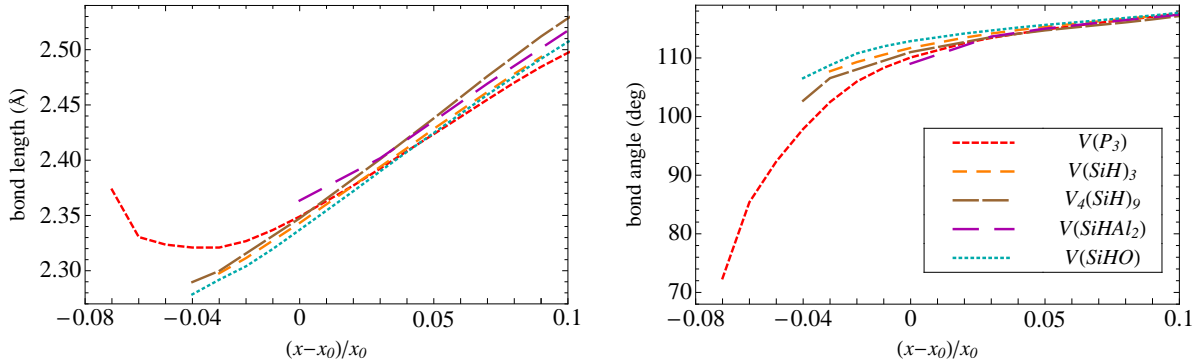


Figure 4.15: Dependence of the bond parameters on strain.

## 4.5 Summary

In this chapter we have elucidated the characteristic features of the silicon dangling bond in a well-defined (and thus controllable) environment, namely in small molecules and in decorated vacancy defects in c-Si. We have determined how critical parameters of the DFT-calculations must be set to ensure numerical convergence. Then we have validated our approach to an all-electron method and experiment. Most notably, we were able to relate the experimental findings to specific atomistic defect models, and we showed explicitly how a symmetry-lowering Jahn-Teller distortion affects the EPR-parameters.

Systematic studies of the influence of the local geometry on the EPR-parameters were presented and used to reason recently found experimental results. The  $g$ -tensor reacts sensitively to energy differences of the local electronic structure, which cannot be always interpreted intuitively. In contrast to this, the hyperfine interaction is characterized by the interplay between the expected  $sp$ -hybridization of the db-orbital as well as the spin delocalization, which can be only captured by our network models.

We then used these findings to interpret the more complex but also more experimentally relevant situation of hydrostatic strain. All crystalline db-models essentially follow the same systematic trend, which is dominated by electronic effects for compressive strain and  $sp$ -hybridization for tensile strain.

It is also important to note that the hyperfine values of the crystalline dangling bonds fall in a narrow range around 300 MHz (isotropic) and 60-70 MHz (anisotropic). The experimental results for the a-Si:H dangling bond indicate a larger degree of spin delocalization. We therefore conclude that the c-Si dangling bond cannot capture all features that are crucial for the understanding of the db-defect in the amorphous matrix.

# 5 Dangling bonds in hydrogenated amorphous silicon

## 5.1 Modelling

Crystalline dangling bonds are local structural distortions in an otherwise homogeneous network. Consequently, it is rather easy to set up the models and obtain a reliable atomic structure. The existence of a unique reference structure guarantees that the defect and its properties are well-defined. The situation becomes dramatically more complex in the amorphous case. Not only do the properties of defects strongly vary between different positions within the heterogeneous matrix, but also the structure of the defect-free matrix is only known in terms of structural 'features' (such as a four-fold coordination of silicon atoms, monohydride or dihydride saturation of other silicon atoms, bond-length and bond-angle ranges). These structural motifs then form a continuous random network. The usage of periodic-boundary conditions yields in comparison to cluster models a more accurate description of the overall electronic and structural characteristics, but it also introduces the problem of matching the structurally disordered models to their periodic images. Besides that, many facets (e.g. the accurate description of forces, criteria for the quality of the structural model) have to be taken into account, which all together make the generation of realistic a-Si:H models very challenging. Since the mastering of these aspects is beyond the scope of our study, we have searched for collaborations with experts in this field instead. We are very grateful that F. Inam, D. Drabold, and K. Jarolimek have offered help and provided us with a-Si:H models and dangling bonds within. To provide some insights into the challenges, strategies and possible limitations, we start this chapter with a brief overview on the generation of theoretical a-Si:H models.

There are essentially two approaches to obtain amorphous models: the direct and indirect approaches [141]. The direct methods use an interatomic potential (either empirical or *ab initio*) and then perform a molecular dynamics, Monte-Carlo (or variants thereof) simulation to find a non-crystalline configuration that is a local minimum of the energy functional. On the other hand, inverse methods build upon experimental data. The key idea of this approach is to start with a configuration that satisfies a set of suitable constraints. Then the atoms are displaced randomly until the input experimental data (such as x-ray diffraction, neutron scattering and extended x-ray absorption) as well as further constraints match with the data obtained from the generated configuration. Thus the overall concept consists in solving a minimization problem by Monte-Carlo techniques ('reverse Monte Carlo'). The additional constraints can be both geometrical or topological and are used to reduce the number of unphysical configurations that are

mathematically correct solutions.

The advantage of the direct methods is that they are completely unbiased [141, 142], which however can also mean that they disagree completely with experimental data. For this approach, the choice of the interaction potential is crucial. Whereas *ab initio* potentials are accurate but computationally expensive, empirical potentials are, as mentioned before, limited by the structural database used to fit the potential. Thus for an amorphous material with its wide range of bonding environments, the transferability of these potentials to different local structural characteristics becomes an important aspect. For silicon, many interatomic potentials have been developed, that are accurate for a single topology (and small variations around it), since it has a clear tendency to  $sp^3$ -bonds and therefore also to tetrahedral geometries. The tight-binding method is a compromise between the empirical potentials and the *ab initio* methods, even though it is in this case challenging to obtain a transferable tight-binding Hamiltonian [141].

The reverse Monte-Carlo approach does not require an interatomic potential [141, 142], and it allows the comparison of structural information obtained by different experiments (by using it as input in separate calculations). However, this method relies on the availability of useful structural, electronic and spectroscopic data as well as on some known topological properties of the material under study. Furthermore, the data needs to be included effectively, since too little information results in unrealistic configurations, whereas on the other hand, the inclusion of too much information makes it difficult to solve the optimization problem. These obstacles can be partly overcome by the 'Experimentally Constrained Molecular Relaxation' (ECMR) method [141], in which one employs additionally an approximate energy functional to reduce the number of unphysical configurations. This technique improves the convergence towards realistic structures. The procedure works self-consistently by minimizing first the configuration according to the experimental information, and then in a second step according to a total-energy minimization (either *ab initio* or otherwise). The scheme is repeated until the models obtained from both steps converge towards the same configuration. One of the first applications of this method has been pure a-Si [143] as well as a-Si:H [144], in which good agreement with a more elaborated construction scheme as well as experiment was found. An alternative to the ECMR-method is the 'Hybrid reverse Monte Carlo' (HRMC) method, which is based on the minimization of the total energy while keeping consistency with diffraction data [145].

Within the direct method, several strategies exist to obtain amorphous structures [141, 142, 146], most notably the 'cook and quench' molecular-dynamics simulation, the 'Wooten-Winer-Wearie' (WWW) approach, and the 'activation-relaxation technique' (ART). The idea of the melt-quench method is to simulate a liquid phase of the desired stoichiometry, and then gradually decrease the temperature below the melting point, thus quenching the system to some disordered state. Evidently, this works best for systems where the structure of the amorphous phase is similar to the liquid one, and when the ordering is quite local, i.e. both phases have small building blocks. For example, this technique works well for  $\text{SiO}_2$ , but it fails for a-Si, since in this case the liquid is a 6-fold coordinated metal, whereas the amorphous phase is a 4-fold coordinated insulator [141]. Also experimentally, a-Si cannot be produced by a melt-quench approach, but

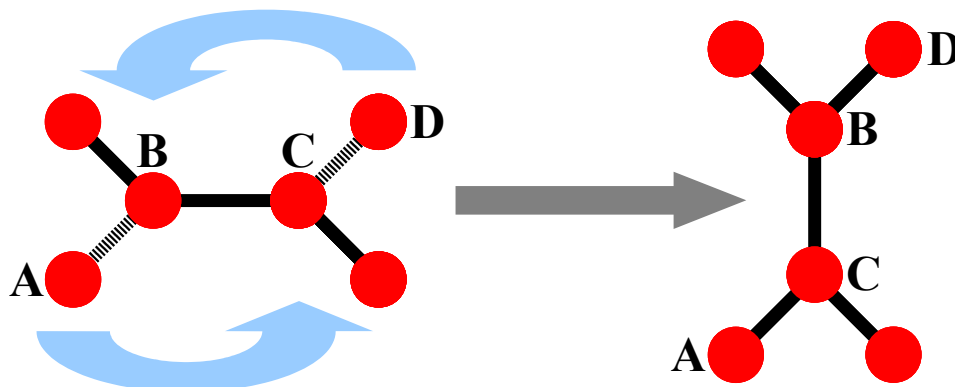


Figure 5.1: Illustration of the basic principle of the Wooten-Weaire-Winer method for the construction of amorphous structures.

rather with ion bombardment or chemical-vapor deposition techniques (see Chapter 1). A severe problem of the melt-quench method is that one can usually simulate only for an unphysical quench rate and an inadequate length of simulation time. This can result in structures which do not compare well with experimental findings (e.g. the structure factor) or which contain too many defects. However, in the case of hydrogenated a-Si, two strategies have been proposed to overcome this deficiency. One possibility involves of heating the crystalline sample just below the melting point and then cooling it down to 0 K with subsequent annealing and quenching cycles [147]. The temperatures in this procedure are chosen to correspond to the experimental conditions. A second approach uses a sufficiently slow cooling rate and a three time-steps procedure [135]. With this method, good agreement with experiment (structure factor, radial distribution functions) is found already for small supercells ( $\text{Si}_{64}\text{H}_8$ ).

An important alternative to the 'cook and quench' technique is the 'Wooten-Weaire-Winer' (WWW) procedure, which generates a 'continuous random network' (CRN) with periodic boundary conditions [142, 146, 148]. A CRN-model is a random arrangement of atoms, with the only condition that they are perfectly coordinated. Furthermore, one can characterize the quality of a CRN-model by the amount of strain as measured by the local deviations from the crystalline environment. Thereby, the ideal CRN is typically defined by having the lowest spread in the bond-parameter distributions. The WWW-method works by switching bonds among four neighbors as illustrated in Figure 5.1. For a bonded pair of atoms BC, a pair of nearest neighbors A and D is chosen, so that A is the neighbor of B and not the neighbor of C, and D is the neighbor of C and not the neighbor of B. Then bonds AB and CD are broken and new bonds AC and BD are created, thus B and C exchange neighbors. After such a randomization of the network by a large number of bond transpositions without relaxation, the network is relaxed through a sequence of bond transpositions using a Metropolis annealing and a Keating interatomic potential. The great advantage of this approach is that there are per definition no coordination-related defects, and the bond angles are constraint to be close to the tetrahedral angle.

A third important technique to generate amorphous structures is called 'activation-relaxation' technique (ART) [142, 146], and it focuses on the jumps of a system from one to the other metastable state. These events can be characterized by the activation energy, which is the energy needed to bring a configuration from a local configurational minimum to a nearby saddle-point. Within this scheme, moving from one to the other local minimum is considered as a two-step process:

1. The activation, during which a configuration is pushed from a local minimum to a nearby saddle-point.
2. The relaxation of the configuration from this saddle-point to a new local minimum.

The advantage of this method is that it defines moves directly in the configurational energy landscape, and it is independent of the interaction potential and material-specific properties. Another appealing aspect is that it requires only the calculation of the force, which makes it scalable with the size of the system. In general, this method is useful for studying rare events in disordered media such as diffusion and relaxation mechanisms. In the case of a-Si, it provided new insights into the cause of the liquid-like nature of structures obtained from empirical-potential based molecular dynamics [149].

Besides the general obstacles of creating an amorphous structure, another question arises in the case of a-Si:H, namely the incorporation of hydrogen. This is also non-trivial, since it broadens the configurational space by parameters such as the hydrogen concentration and the local hydrogen environment. In NMR experiments on a-Si:H [150, 151], the H-concentration can vary between 8-32%, and there is consequently also a certain flexibility for this parameter in theoretical simulations. Furthermore, hydrogen can be incorporated into the network in several ways. In silicon monohydride it favorably passivates 'dangling bonds' (isolated Si-H), but it can also occur as bond-centered hydrogen or it forms platelet-like structures [152]. Additionally, hydrogen can also appear in its molecular form [153]. The spectrum is further enriched by the presence of di- and tri-hydrides as well as  $(\text{SiH}_2)_n$  chains [154, 155]. This broad range of possible hydrogen microstructures emphasizes the complexity of the material, which in turn makes theoretical modelling very difficult. One possibility of H-incorporation is to start from a pure a-Si network and then add an appropriate amount of hydrogen atoms at random positions [142]. In a second step one simulates the molecular dynamics at a given temperature, which leads to a reorganization of the structure. A similar idea exploits the annealing of an a-Si sample [147], to which hydrogen has been added in an evenly distributed manner. For the ECMR-approach [144], hydrogen is used to passivate naturally occurring dangling and floating bonds respectively. Then the model is relaxed again, and this 'relax and clean' procedure is carried out until the defect concentration is sufficiently low. In contrast to this, within the step-wise 'cook-and-quench' molecular dynamics [135], hydrogen is already included in the initial structure, and thus it is not necessary to insert it artificially.

The dangling-bond models used in the following are created from a-Si:H supercells by removing one hydrogen atom, and then relaxing the structure again [135, 141, 156].

As mentioned, for our study we use db-models created by our collaborators F. Inam, D. Drabold and K. Jarolimek. One important question of the modelling process is related to the defect concentration. Experimentally, the dangling-bond defect density is of the order of  $10^{15}$ - $10^{19}$  defects/cm<sup>3</sup> [11]. The actual magnitude depends in particular on the temperature during film-growth with the minimum being reached for around 250°C. From the measured defect concentration, we can deduce an estimate for the average spatial separation between two dangling bonds by assuming a homogeneous db-distribution. If we further consider the volume of one single dangling bond to be spherical, we get for the db-db distance the value 60-140 Å. However the largest computationally feasible supercells in our calculations have a lattice constant of about 16 Å, and thus we have a significantly stronger interaction between dangling bonds. Despite this deficiency, recent studies [135, 156] have not observed supercell-size effects for key properties such as the radial distribution function, the band gap and tail states.

What we have learned here is that it is nontrivial to generate amorphous structures. In particular, there is no straightforward 'cooking recipe', and the method of choice depends on the problem at hand. The inclusion of hydrogen makes the situation even worse, since it couples to the network in a large variety of ways. Furthermore, present-day simulations overestimate the coupling between dangling bonds due to limitations of the supercell size.

## 5.2 Statistical analysis of EPR-parameters

In the crystalline environment we can unambiguously assign the dangling bond to a specific atom. The situation changes dramatically for an amorphous material, in which the defect structure is much more complex. In this case, only a spin-polarized calculation yields the necessary information to identify the actual db-atom. Furthermore, to take the element of structural randomness into account, we need to consider a large db-ensemble. However, the mentioned complexity in the generation of the models means that one can create only a small set of possible configurations. Consequently we have to work with a limited number of db-models and the basic challenge in the analysis consists in making conclusions which are not so dependent on the statistics.

For our investigation we use 26 small (64Si-7H) as well as 28 large db-models (216Si-29H). These ratios between silicon and hydrogen atoms yield a hydrogen concentration on the order of 11-13%. Experimentally it can have a much larger fluctuation in between 7-30% [28, 45]. The computational parameters are chosen according to the established dependencies on convergence and accuracy (Section 4.2.1). The dense  $\mathbf{k}$ -point mesh required for the  $g$ -tensor has the effect that the calculations are very resource-demanding. The large supercells have been therefore computed on a powerful IBM Power6 575 cluster at the Rechenzentrum Garching. The processor clock is 4.7 GHz and the peak performance/processor is 18.8 GFlops/s. For the hyperfine parameters, the limiting factors are the time of the self-consistent calculation (on the order of 12 hours for 20 processors) and the memory demand for the post-processing step to obtain the parameters (4 GB/processor). In contrast to that, the  $g$ -tensor calculation itself has a computation

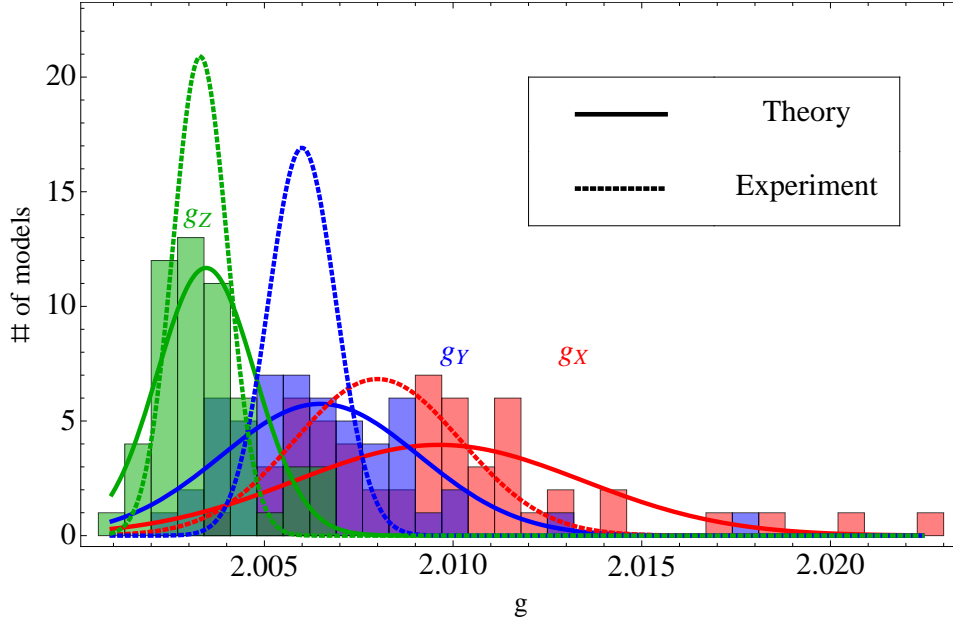


Figure 5.2: Statistical distribution of the theoretical  $g$ -values, which are sorted according to their magnitude. For the comparison to a recent multi-frequency experiment [28], we fit the histogram by a normal distribution (solid line).

time of 1.5 days on 112 processors with a similar memory requirement as for the hyperfine parameters. Overall we see that the calculation of the EPR-parameters itself is quite demanding. As mentioned, in this context it is an important observation that the hyperfine parameters need much less CPU-time than the  $g$ -tensor.

For the basic statistical analysis, it is the best strategy to start with the assumption that the removal of one hydrogen atom from an ideal a-Si:H supercell with a subsequent relaxation step creates a db-defect. Within this unbiased approach, we obtain from our db-ensemble a distribution for the principal values of the  $g$ -tensor (Figure 5.2) and the  $A$ -tensor (Figure 5.3). In these figures we compare our results with a recent multi-frequency EPR-experiment [28], which was most notably able to resolve the principal values of the  $g$ -tensor with a higher accuracy. This was achieved by resolving the spectrum at higher microwave frequencies. As discussed in Chapter 2, only the  $g$ -tensor is field-dependent. Due to the presence of  $g$ -strain, i.e. a statistical distribution of  $g$ -tensors, it is advantageous to measure the principal values of the  $A$ -tensor at low magnetic fields and corresponding frequencies (S-band, X-band), and the ones of the  $g$ -tensor at high frequencies (Q-band, W-band). To compare these results with our statistical approach, we fit a normal (Gaussian) distribution to our data. This approach is motivated by the procedure to extract the EPR-parameters experimentally. It requires spectrum simulations, in which one fits model parameter distributions to best reproduce the measured data. In doing so, one has to assume that the statistics of the principal values can be described by a Gaussian distribution, which is however not based on a fundamental reason and thus might not be justified.

<i>db-model</i>	$g_{Iso}$	$g_X$	$g_Y$	$g_Z$	$A_X$ (MHz)	$A_Y$ (MHz)	$A_Z$ (MHz)	$a$ (MHz)	$b$ (MHz)
<i>Theory</i>									
Si <sub>4</sub> H <sub>9</sub>	2.0056	2.0075	2.0075	2.0019	-213	-213	-457	-294	-82
c-Si	2.0073	2.0106	2.0106	2.0011	-256	-256	-441	-318	-62
a-Si:H	2.0065	2.0096	2.0065	2.0035	-214	-216	-338	-256	-41
	-	(0.0090)	(0.0062)	(0.0030)	(156)	(157)	(190)	-	-
	[0.0006]	[0.0010]	[0.0007]	[0.0004]	[18]	[18]	[22]	[19]	[4]
<i>Theory - a-Si:H (supercell size)</i>									
64Si-7H	2.0064	2.0093	2.0064	2.0035	-214	-216	-327	-252	-37
216Si-29H	2.0066	2.0099	2.0066	2.0034	-214	-216	-348	-260	-44
<i>Theory - (localized db-models)</i>									
	2.0067	2.0100	2.0067	2.0034	-216	-218	-360	-265	-48
	[0.0009]	[0.0015]	[0.0011]	[0.0004]	[24]	[24]	[26]	[24]	[3]
<i>Theory - (not-triply coordinated db-models)</i>									
	2.0057	2.0082	2.0058	2.0030	-218	-221	-326	-255	-35
	[0.0010]	[0.0015]	[0.0013]	[0.0007]	[55]	[54]	[54]	[63]	[11]
<i>Theory - (delocalized db-models)</i>									
	2.0065	2.0095	2.0062	2.0039	-216	-219	-293	-243	-25
	[0.0009]	[0.0016]	[0.0009]	[0.0007]	[34]	[34]	[44]	[37]	[7]
<i>Experiment - a-Si:H</i>									
rhombic [28]	2.0058	2.0079	2.0061	2.0034	-151	-151	-269	-190	-39
	-	(0.0054)	(0.0022)	(0.0018)	(46)	(46)	(118)	-	-
axial [28]	2.0057	2.0065	2.0065	2.0042	-149	-149	-265	-188	-39
	-	(0.0047)	(0.0047)	(0.0019)	(47)	(47)	(113)	-	-
axial [44]	2.0067	2.0080	2.0080	2.0040	-154	-154	-305	-205	-50
	-	(0.0029)	(0.0029)	(0.0022)	(28)	(28)	(56)	-	-
axial [45]	2.0056	2.0065	2.0065	2.0039	-143	-143	-333	-206	-63
	-	-	-	-	(56)	(56)	(73)	-	-

Table 5.1: Comparison of theoretical and experimental results for the EPR-tensors (principal values and hyperfine parameters). The values for the crystalline models corresponds to the average over the localized db-models in Figure 4.8. In the case of a-Si:H, the statistics includes 54 db-models. The value in round brackets indicates the full-width half maximum (FWHM), and the value in rectangular brackets the confidence interval (95% probability). For the experimental determination of the  $g$ -tensor either uniaxial or no symmetry (i.e. rhombicity) is assumed. The resulting principle values have an accuracy on the order of two ten-thousandths [28]. The principal values of the  $A$ -tensor have an experimental uncertainty of up to 30 MHz, the isotropic coupling of about 10 MHz, and the anisotropic coupling of about 10 MHz. Localized, not-triply coordinated and delocalized db-models refer to subsets of 33, 11 and 16 db-models according to the criteria discussed in Section 5.3.1.

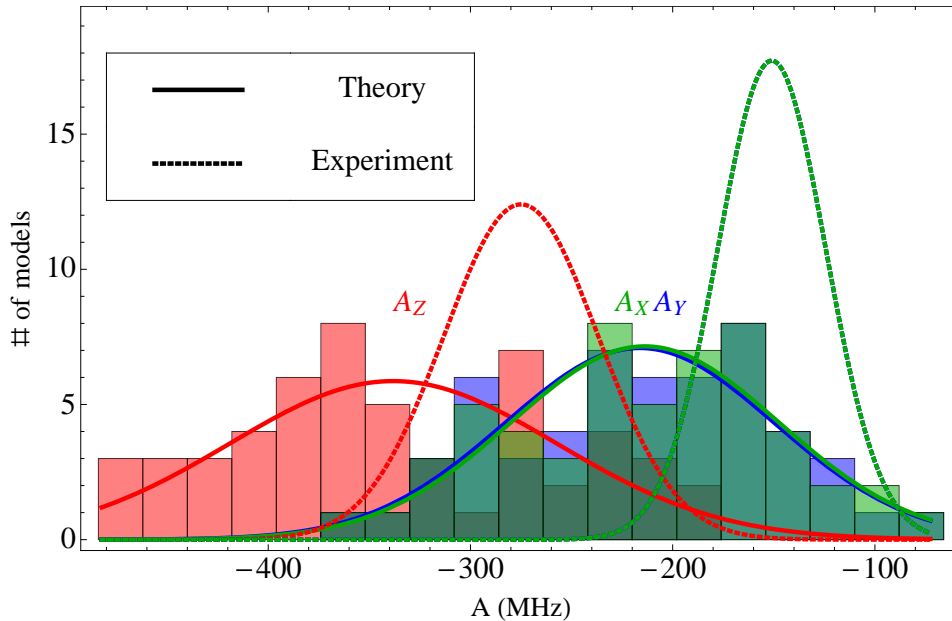


Figure 5.3: Statistical distribution of the theoretical  $A$ -values, which are sorted according to their magnitude. For the comparison to a recent multi-frequency experiment [28], we fit the histogram by a normal distribution (solid line).

Figure 5.2 shows the  $g$ -value distribution. As visible, for  $g_X$  and  $g_Y$ , the scattering of the values is rather large. The fitted curve is a rather crude estimate and disguises an actual two-peak structure in the histogram. But from the statistics it is not clear whether the inclusion of more models would enhance this double-peak shape or lead to a single peak right in the middle of the maximum of the fit. In contrast to this, the  $g_Z$ -distribution is rather narrow. Despite the statistical deficiencies, there is surprisingly good agreement between the theoretical and experimental  $g$ -values (Table 5.1). For example, the discrepancy for the isotropic  $g$ -value is on the order of  $2.9 \cdot 10^{-4}$ , which is on the same order as the scatter among different experiments. Quantitatively, it seems as if the tetrasilyl radical fits the best to the experimental value. But it fails to reproduce the rhombicity of the  $g$ -tensor, which one obtains from symmetry-unconstrained simulations of the measured spectrum [28]. In contrast to that, we see that our findings for the amorphous models support this recent experimental outcome, since the corresponding  $g_X$ - and  $g_Y$ -values do clearly not coincide.

The  $g$ -tensor rhombicity can be reasoned by second-order perturbation theory [28]. For the sake of simplicity, let us assume that the singly-occupied db-orbital  $\psi_p$  is given by a pure  $|p_z\rangle$  orbital and the other orbitals  $|p_{x,y}\rangle$  are also of atomic type. We define the Cartesian coordinate system such that the  $z$ -axis coincides with the axis of the db-orbital. By this we can show that the paramagnetic contribution vanishes for  $\alpha\beta = zz$ , since  $L_z |p_z\rangle = 0$ . Significant deviations from  $g_e$  (Equation 2.10) are therefore only expected for  $g_X \equiv g_{xx}$  and  $g_Y \equiv g_{yy}$  given by

$$\Delta g_X = 2 \frac{\langle p_z | \lambda L_x | p_y \rangle \langle p_y | L_x | p_z \rangle}{\varepsilon_{p_z} - \varepsilon_{p_y}} = 2 \frac{\lambda}{\varepsilon_{p_z} - \varepsilon_{p_y}}$$

$$\Delta g_Y = 2 \frac{\langle p_z | \lambda L_y | p_y \rangle \langle p_x | L_y | p_z \rangle}{\varepsilon_{p_z} - \varepsilon_{p_x}} = 2 \frac{\lambda}{\varepsilon_{p_z} - \varepsilon_{p_x}}$$

From these expressions it is clear that if the degeneracy of the  $p_x$ - and  $p_y$ -orbitals is lifted, the  $g_X$  and  $g_Y$ -values will deviate from each other too. This can be caused e.g. by fluctuations in the bond parameters as observed e.g. for the tetrasilyl radical (Figure 4.10). To conclude, the rhombicity of the  $g$ -tensor in a-Si:H is an important new insight, which can be motivated by fluctuations in the local defect structure.

The comparison of the theoretical and experimental hyperfine tensor is included in Table 5.1. First, it is obvious that there is a significant discrepancy between theory and experiment for the isotropic hyperfine interaction on the order of 50-66 MHz (24-35%). This is much larger than the deviation for the crystalline models (on the order of 3%, Table 4.4). However we do not see a similar discrepancy for the anisotropic coupling. Thus we do not expect that the larger theoretical  $a$ -value is caused by a fundamental conceptual problem of our approach. Indeed, from our findings we would tend to attribute it rather to a physical effect.

Despite this open problem, theory is able to reproduce the correct symmetry of the  $A$ -tensor. In both theory and experiment, the tensor is uniaxial. This is an interesting finding, since it is in principle not intuitive, how such a symmetry can be related to a rhombic  $g$ -tensor. In the crystalline environment we have found this constellation only for JT-distorted systems (Table 4.4). To rationalize the symmetry of the  $A$ -tensor, we have to consider that it depends directly on the ground-state spin density. Therefore it is strongly dominated by the local orbital character ( $sp^x$ -hybrid) of the db-state at the site of the trivalent Si atom. Structural variations due to the amorphous matrix affects its orientation and possibly the degree of  $sp$ -hybridization, but do not alter the fundamental  $sp^x$ -character of the db-orbital. Consequently, its axial symmetry is maintained even in the presence of large disorder-induced fluctuations of bond lengths and bond angles (as is the case in a-Si:H).

At this point, let us discuss further aspects of the statistics (Table 5.1). First, we see that there is no significant difference between the small and large supercells. This result confirms the observation made for other properties such as the radial distribution function [135, 156]. Secondly, the width for the mean values is smaller in experiment than in theory. Thus a larger number of theoretical db-models would be preferable. However, there are no clear indications that this is the main reason for the discrepancy between theory and experiment.

In conclusion, within the realms of our limited statistics, we can deduce the following properties of a-Si:H dangling bonds. First, theory and experiment agree on the symmetry of the EPR-tensors. It is found that the  $g$ -tensor is rhombic and the  $A$ -tensor uniaxial. This characteristics can be related to the different underlying physical mechanisms behind the tensors. The hyperfine tensor depends on the spin density, and is

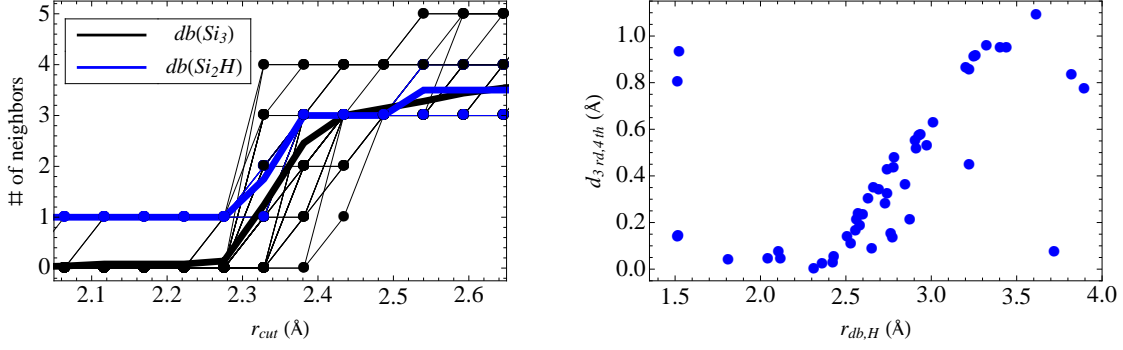


Figure 5.4: Coordination at the db-site. The figure on the left side shows the number of db-neighbors at a certain distance  $r_{cut}$  from the db-atom. The black color indicates the trends for a  $Si_3$  backbond configuration, and the blue color for a  $Si_2H$  configuration. The thick lines stand for the corresponding mean-values. The figure on the right side characterizes the bonding situation of hydrogen to the db-atom. It shows the distance  $r_{db,H}$  between the db-atom and the closest hydrogen versus the distance  $d_{3rd,4th}$  between the third and fourth db-neighbor. Hydrogen is only bonded to the db ( $Si_2H$  configuration), if  $d_{3rd,4th}$  is sufficiently large for a correspondingly small distance  $r_{db,H}$ .

thus basically dictated by the  $sp$ -hybrid character of the db-orbital. The  $g$ -tensor, on the other hand, depends on all orbitals contributing to the  $g$ -shift (Equation (2.10)) and these orbitals (in particular their energies) do sensitively react to fluctuations in the backbond geometry. Secondly, the hyperfine parameters of the db-atom are lower in a-Si:H than in c-Si, which means that the spin is more delocalized. However, theory is only partly able to reproduce this down-shift of the isotropic parameter.

## 5.3 Structural aspects of dangling bonds in a-Si:H

### 5.3.1 Categorization

The statistical analysis yields only a basic understanding of the EPR-parameters and their correlation to structural features. Going beyond this picture, it is important to find ways to classify the db-models. For that we emphasize again that the db-atom in an amorphous model is characterized by having the largest isotropic hyperfine interaction. Further aspects are a priori unknown, which means that one has to check for the coordination, i.e. that the defect has indeed only three neighbors. Besides that, we will consider the overall spin distribution in the models (to clarify the degree of localization) as well as the backbond configuration, which might include hydrogen atoms.

First let us consider the defect coordination. It is characterized by the number of atoms at a specific distance  $r_{cut}$  from the db-atom. Here we distinguish between db-

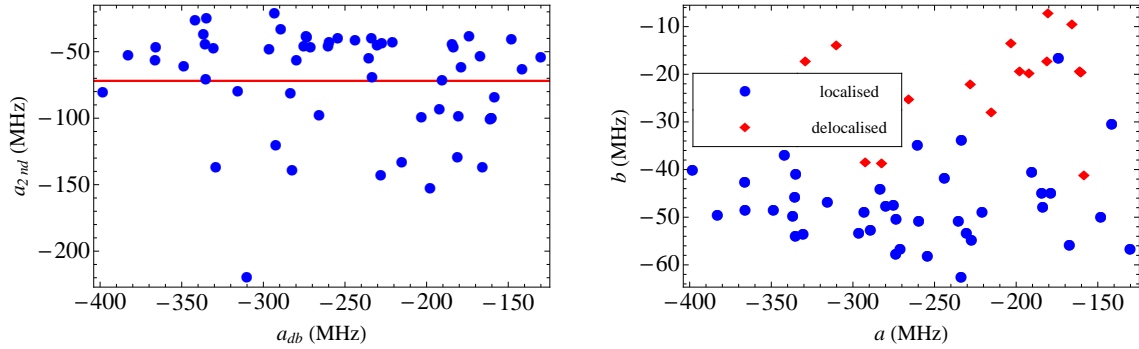


Figure 5.5: The effect of delocalization in the db-models. The figure on the left side shows the relation between the largest ( $a_{db}$ ) and the second-largest ( $a_{2nd}$ ) isotropic hyperfine interaction. The red line marks the mean value for  $a_{2nd}$ . The right side shows the relation between the hyperfine parameters at the db-atom. Here we distinguish between localized and delocalized models by their  $a_{2nd}$ . For localized db-models  $a_{2nd}$  is not larger than -80 MHz.

models, which have a hydrogen atom among its three nearest neighbors, and the rest. For that matter, we have to consider two parameters, namely the distance  $r_{db,H}$  between the db-atom and the closest hydrogen atom, as well as the distance between the third and fourth db-neighbor. As shown on the right side of Figure 5.4, in only 4 cases,  $d_{3rd,4th}$  is large enough so that the db-atom is indeed bonded to hydrogen. For  $r_{db,H} > 1.5 \text{ \AA}$ , there are a number of models with a four-fold configuration (3 silicon, 1 hydrogen) at the db-atom, and for  $r_{db,H} > 2.5 \text{ \AA}$  with a three-fold configuration (3 silicon) respectively. Interestingly, for such  $r_{db,H}$ -values, there is a gradual increase of the distance between the third and fourth neighbor. In that sense, the dangling bond gains its true 3-fold coordinated character the further the closest hydrogen.

The left side of Figure 5.4 illustrates the dependence of the coordination number  $N$  on the cutoff distance  $r_{db,H}$ . We recognize from the trend for the mean coordination that  $N$  increases drastically for distances in the range 2.3-2.4  $\text{\AA}$ , whereas the slope becomes smaller for larger values of  $r_{db,H}$ . This implies that most db-models are truly three-fold coordinated with a bond length around 2.43  $\text{\AA}$ . However, some models show significant deviations, and e.g. have four neighbors at comparative distances. Since these bonding situations do not correspond to a db-defect, we introduce the following criteria: a db-defect is characterized by having exactly 3 neighbors within a cutoff-radius of 2.42  $\text{\AA}$ .

To quantify the degree of localization, let us look at the relation between the largest and the second-largest  $a$ -coupling. For the crystalline models, it was relatively constant at around -30 MHz (Table 4.5, Figure 4.13), and it could be unambiguously assigned to the second backbond neighbor. Even though the situation in a-Si:H is far more complex, one would expect that for a truly localized dangling bond, the second-largest value  $a_{2nd}$  should be significantly smaller than  $a_{db}$ . To analyze the relation between both in detail, we plot their correlation in Figure 5.5. One can see that for the majority of the models,

$a_{2nd}$  is not larger than -70 MHz. However some models have  $a_{2nd} > -100$  MHz, and we would thus consider these cases to be too delocalized to be a db-defect. Overall, to draw a line between both situations, -80 MHz is a reasonable cutoff value. When applying this criteria to the hyperfine values of the db-atom, we see that the delocalized db-models are also characterized by an  $a$ -parameter usually smaller as -250 MHz and a  $b$ -parameter, which is generally not larger than -30 MHz. On the other hand, there is no clear correlation between the parameters sets ( $\{a_{db}, a_{2nd}\}$ ,  $\{a, b\}$ ), since they are distributed rather homogeneously among the range of values.

When applying the established criteria to our db-models, we find that 4 models (7%) have backbond hydrogen, 11 models (20%) are not-triply coordinated, and 16 models (30%) are delocalized. Thus in total 33 models (61%) correspond to a localized, 3-fold coordinated db-defect either bonded to three silicon neighbors or to two silicon and one hydrogen atom respectively. Most importantly, we learn from this categorization that the amorphous host matrix gives rise to a much broader spectrum of db-like defects than observed in crystalline silicon. On the one hand, the removal of one hydrogen from the system does not necessarily lead to the creation of a true db-defect. Furthermore, the spin density is rather delocalized in a significant number of cases. Correspondingly, the actual coordination as well as spin delocalization are important features of the a-Si:H db-defect.

It is also interesting to note how the categorization affects the statistics (Table 5.1). First, we see that there is no significant change in the  $g$ -tensor for the localized db-models. However for the hyperfine parameters we obtain a slight trend to a larger spin localization at the db-atom. The not-triply coordinated db-models are characterized by a smaller  $g_{Iso}$ -value, which indicates that the db-level is shifted towards the conduction-band tail [129]. Furthermore, their hyperfine parameters imply that the db-orbital of these models has a smaller  $p$ -like character. A similar characteristic is also observed for the delocalized models, in which case the shift in the  $b$ -parameter is even larger. However, neither kind of db-models has a substantially smaller isotropic coupling.

### 5.3.2 Localized db-defects

The localized db-models show a great diversity in spite of their small number. In this context, it is important to characterize the bond parameters of the db-atom. For that purpose we plot the statistical distribution of bond lengths (Figure 5.6) and bond angles (Figure 5.7) along with their deviation from the symmetric case, in which all bond lengths and bond angles are the same (i.e  $l_1 = l_2 = l_3$ ,  $\alpha_1 = \alpha_2 = \alpha_3$ ). As we see, most db-models have rather homogeneous bond lengths, fluctuating by only 0.08 Å at the most. It is interesting that the dangling-bond bond length deviates by only 0.05 Å from the overall bond length obtained in other theoretical studies [134, 135]. Similarly, it is rather close to the experimental finding  $l = 2.35 - 2.37$  Å (summarized in [135]). This illustrates that the lengths of the bonds at the db-atom are not distinguishable from the rest of the network. In other words, they are not characteristic for a local defect environment.

The mean bond angle is given by  $109.72^\circ$ , and thus deviates insignificantly from the

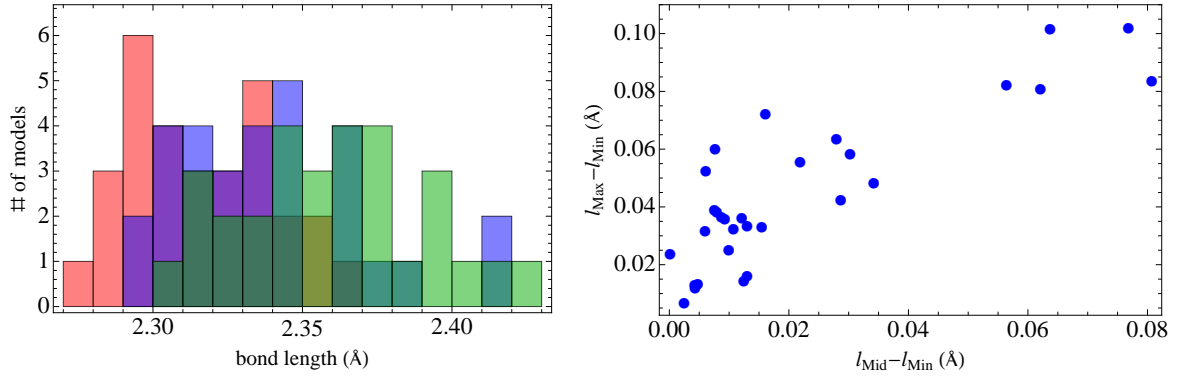


Figure 5.6: Bond-length statistics for localized dangling bonds. On the left side we plot the statistical distribution of the three bond lengths. The figure on the right side shows the correlation between the shortest bond length  $l_{Min}$  and the other two lengths ( $l_{Mid}$ ,  $l_{Max}$ ).

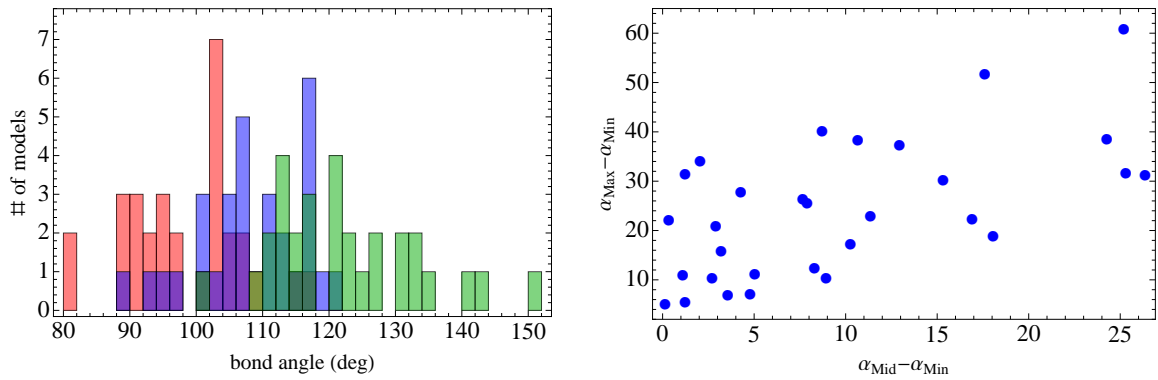


Figure 5.7: Bond-angle statistics for localized dangling bonds. On the left side, we plot the statistical distribution of the bond angles. The figure on the right side shows the correlation between the shortest bond angle  $\alpha_{Min}$  and the other two angles ( $\alpha_{Mid}$ ,  $\alpha_{Max}$ ).

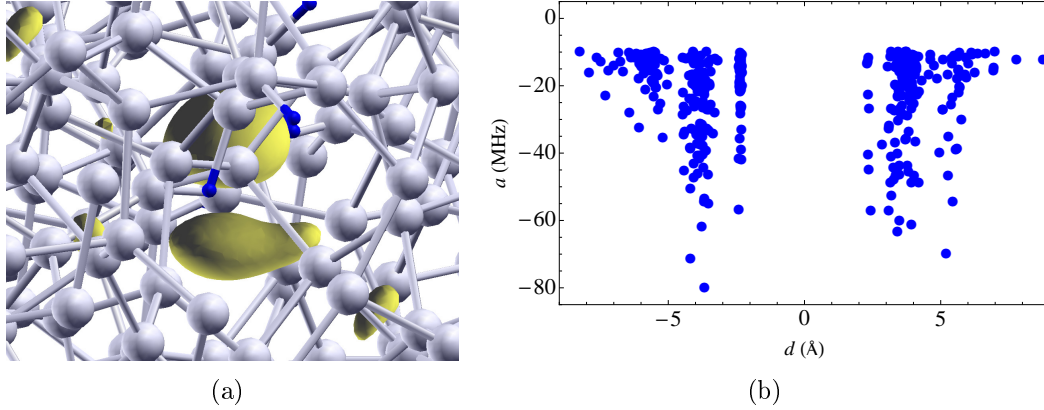


Figure 5.8: (a): Example of a localized dangling bond with a strong isotropic hyperfine interaction on the first neighbor. (b): The dependence of the isotropic hyperfine coupling  $a_{bb}$  on the distance  $d$  from the db-atom. We only consider couplings, which are larger than -10 MHz, and we distinguish between opposite (positive parameter-range) and backbond (negative parameter-range) atoms. Details of this classification scheme are described in the text.

tetrahedral angle. First let us mention that the overall bond angle averaged over ideal a-Si:H models [135] corresponds to  $108.89^\circ$  with a standard deviation of  $\sigma = 13.57^\circ$ . Thus the db bond-angle distribution appears to have the same geometric properties as the rest of the network. But this is only a heuristic argument, since for a true comparison, one would have to compute the angle distribution function for the db-models. We note for completeness that the experimental standard deviation typically obtained from high-energy X-ray diffraction (tabulated in [135]) is significantly smaller ( $\sigma = 7.9 - 9.63^\circ$ ), which means that theory tends to overestimate this parameter.

Within our context, it is more important that the local bond-angle geometry is rather inhomogeneous (Figure 5.7). For example, the deviation between the shortest and the largest bond angle is more than  $10^\circ$ . When we now compare this with the angular dependence of the hyperfine parameters for our crystalline db-models (Figure 4.11), we recognize that fluctuations of that order can have a drastic effect. Consequently, it becomes quite complex to relate  $a$  and  $b$  to the bond parameters. Indeed, as closer inspection reveals, there is no clear trend in between the hyperfine- and structural parameters.

In a similar way, there is also a greater variety in the hyperfine couplings of backbond atoms. The most important aspect for the a-Si:H db-models is that, in contrast to their crystalline counterparts, one also observes strong isotropic couplings for atoms, which are not second-nearest neighbors. This is illustrated in Figure 5.8(a), which shows a dangling bond with a significant spin density at the first backbond neighbor. To quantify the complexity of the spin distribution in the network, we depict in Figure 5.8(b) the dependence of the isotropic superhyperfine coupling on the distance from the db-atom. In doing so, we also apply a criteria to distinguish between the backbond and the opposite

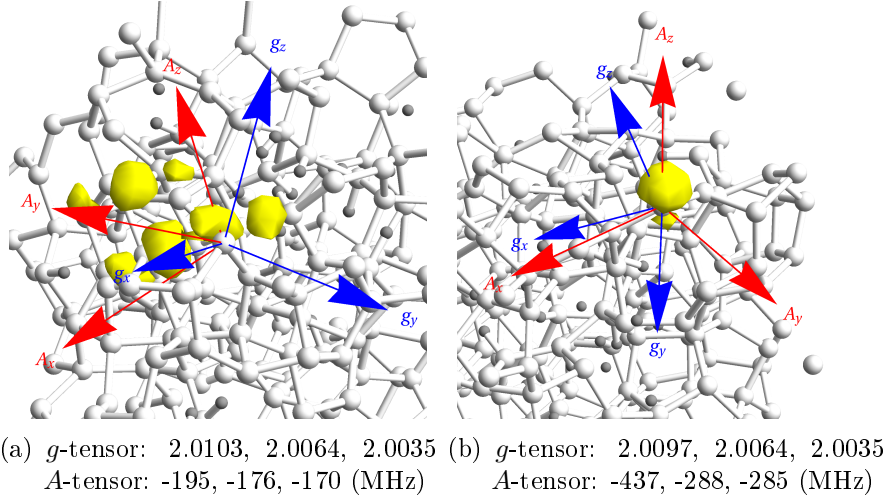


Figure 5.9: Example of a delocalized and a localized db-model with similar  $g$ -values.

db-side. For that reason, we first compute the centroid of the triangle spanned by the three nearest neighbors, the 'backbond'-atoms. Then we compare the distance  $d_{db,n}$  between an atom (with  $a > 10$  MHz) and the db-atom with the distance  $d_{c,n}$  between the centroid and the atom. If the atom is closer to the centroid,  $d_{c,n} < d_{db,n}$ , we consider it as on the 'backbond'-site, and as opposite otherwise. In the former case we assign a minus to the distance, and in the latter case a plus respectively. Overall this gives us the following basic notion of the spatial spin distribution in the supercell. The most significant trend characterizes the shell-structure of the network. It manifests itself by a clustering of large  $a$ -values at certain distances. As expected, the strongest couplings occur around the second-nearest neighbor distance, even though there is no difference between 'opposite' and 'backbond', since for both cases the superhyperfine interaction is similar in magnitude. This again indicates that in our simulations dangling bonds appear rather randomly at sites with an appropriate geometric distortion in the network with a consequently rather homogeneous distribution of neighbors. They differ in this aspect from their crystalline counterparts, which are typically related to the presence of a vacancy (Chapter 4). In this context, it is reasonable but still interesting, that the superhyperfine coupling is on average larger than in the crystalline environment. Apparently, this is another manifestation of the delocalization, which is -as we have seen- a characteristic feature of a-Si:H dangling bonds.

So far we have only looked at the hyperfine parameters, since the spin density is related in a -more or less- complex way to the local defect structure. To illustrate that one cannot get such kind of information from the  $g$ -tensor, let us consider the db-models depicted in Figure 5.9. As we see, the  $g$ -tensor is similar in both cases, even though both have completely different spin distributions with correspondingly different principal values for the  $A$ -tensor. We can deduce from this that the  $g$ -tensor can be similar for quite different degrees of spin localization. A related point is that in the delocalized case, the  $g$ -tensor is closer to the experimental value [129] of a db-defect ( $g = 2.0055$ ) than the

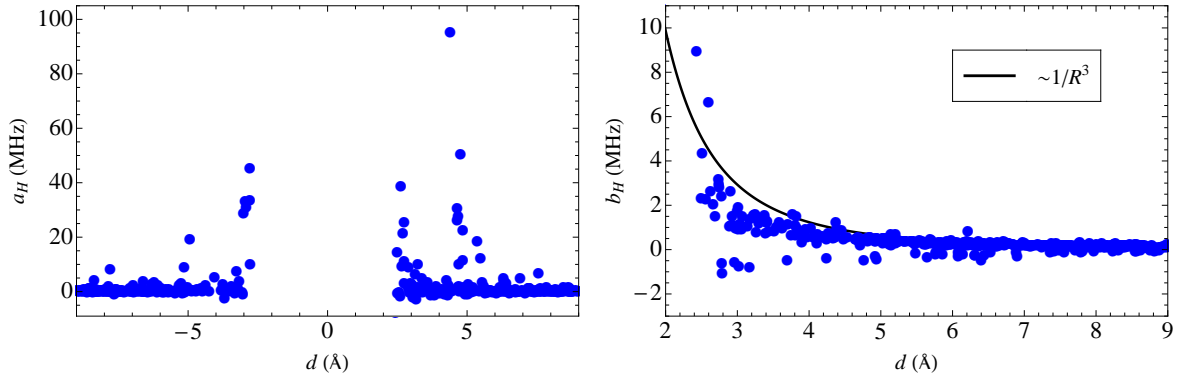


Figure 5.10: Distance dependence of the hyperfine parameters of hydrogen for 33 localized db-models. The black line denotes the point-dipole approximation (Equation 2.18). We distinguish between opposite (positive parameter range) and backbond (negative parameter range) atoms according to the categorization established in the previous subsection.

valence-band tail ( $g = 2.012$ ). That shows that here again, spin delocalization is not only triggered by electronic effects but also by the local geometry. Both findings imply that, in the presence of  $g$ -strain, the  $g$ -tensor provides no additional information on the local defect structure. It is therefore convenient to focus on the hyperfine parameters, which are also far less expensive to compute.

The orientation of the  $g$ - and  $A$ -tensor gives further information on the correlation between both quantities. One characteristic of the db-models is that in some cases both axes are not aligned at all (e.g. as in Figure 5.9(a)). In other words,  $g_Z$  does not enclose the smallest angle with  $A_Z$ . However, for 17 (52%) db-models, the angle between  $g_Z$  and  $A_Z$  is smaller than  $20^\circ$ , and a further 9 (27%) db-models have an angle in between  $20^\circ - 30^\circ$ . This implies that in general collinearity between  $g_Z$  and  $A_Z$  is preserved for localized db-models.

### 5.3.3 Hydrogen

To complete our structural picture, we now look at the distance dependence of the hyperfine parameters of the hydrogen atoms. This is in particular important, since it has been suggested that hydrogen actively participates in the creation of light-induced dangling bonds [157]. As mentioned in Chapter 1, the idea is that hydrogen is bound to a silicon atom with a weak Si-Si bond. Under steady-state illumination, holes will be trapped, breaking this bond. In a second step, the hydrogen atom stabilizes the bond, so that the system ends up in a configuration of either two separate dangling bonds or one dangling bond + one Si-H-Si complex. It is clear that this mechanism requires hydrogen to be close by.

In this context, one general observation is that only 3 (9%) db-models have a hydrogen atom as backbond neighbor. Therefore, in our simulations, it is not the most

likely occurring db-configuration, and it supports the findings of recent experimental studies [130, 158]. However, even this small number of models shows a great diversity in the EPR-parameters. The isotropic  $g$ -value is in between 2.0038-2.010, the  $a$ -value in between -233 MHz to -342 MHz, and the  $b$ -parameter in between -37 to -63 MHz. Thus there is no distinction of db-atoms with a  $\text{Si}_2\text{H}$  configuration and those with  $\text{Si}_3$  neighbors respectively, and the EPR-parameters of both are essentially determined by the same geometrical and electronic effects. The isotropic coupling of the backbond hydrogen is comparable to the tetrasilyl radical (Table 4.7).

From the overall isotropic couplings plotted in Figure 5.10 we see the same features as for neighboring silicon atoms. First, hydrogen can have a significant spin polarization. Furthermore, it is distributed homogeneously with respect to the distance from the db-atom, which is again in agreement with a recent experimental observation [130]. For distilling the distance dependence of hydrogen from the measured EPR-spectrum, it is crucial to know the range of applicability of the point-dipole approximation. With respect to this question, our studies of the anisotropic coupling for the molecule over the Si(111)-surface as well as the a-Si:H-db-models can give a corresponding estimate. For the former we have found in Section 4.3.3 a minimum distance of 2.8-3.5 Å, and as obvious from the right-hand side of Figure 5.10, this is also a reasonable estimate for the a-Si:H db-models.

Even though our db-set is small, it still characterizes a variety of geometrical and electronic constellations, which in turn cause a corresponding broad distribution in the EPR-parameters. This also implies that there is no unique structural model of a dangling bond in amorphous silicon, and the measured trends have to be interpreted in terms of a defect ensemble capturing the relevant characteristics. With respect to this, the most striking feature of the theory-experiment comparison is the discrepancy in the isotropic hyperfine coupling by 50-70 MHz to which we will turn to in the following.

## 5.4 The discrepancy between theory and experiment

### 5.4.1 Methodological aspects

Our statistical approach for the db-defect in a-Si:H is able to explain many of the experimentally observed features. However, measurements indicate a larger spin delocalization as obtained for the theoretical db-models. In this section we will address the question of possible influences, which also gives a perspective for future work.

For that reason we start by clarifying the significance of the deviation of the discrepancy between theory and experiment. For the crystalline models we have obtained an accuracy on the order of 10 MHz (Table 4.4). This remarkable agreement originates at least partly from the deep-level character of the considered db-defects and the corresponding high degree of localization. The hyperfine parameters are consequently determined by the local defect geometry, which was comparatively easy to obtain due to the comparable stable electronic structure. In contrast to that, the appearance of spin delocalization requires an accurate modeling of a much larger defect surrounding

and this makes it intrinsically more difficult to reproduce the experimental values well. On the other hand, the theoretical values for our a-Si:H db-models are almost halfway in-between the experimental findings for c-Si and a-Si:H. Overall, we get the impression that we are able to characterize some features of this  $\alpha$ -shift but we are also missing some important aspects.

At this point, it is most natural to question the choice of the theoretical parameters. With respect to that, one key parameter is the exchange functional. The most popular alternative to the PBE-functional is the LDA-functional, but from previous findings [126], we have no indication that it would improve the agreement. For hydrogen, it would actually make things worse. The inclusion of Hartree-Fock exchange by hybrid functionals increases the band gap whereas the defect levels change only slightly as has been shown for the dangling bond in silicon [159]. Localized dangling bonds with a deep state in the gap should therefore not change much when hybrid functionals were used. More shallow, delocalized defects, on the other hand, might get deeper and thus become more localized at the hybrid-functional level of theory, which then leads to larger  $\alpha$ -values. Another important choice is the pseudopotential, and the associated neglect of core polarization. Yet the good agreement for c-Si defects (Section 4.2.3) suggests that this is not a critical approximation. It is unlikely that pseudopotential errors are strongly enhanced by the amorphous environment.

The situation is more complex with respect to the modelling paradigm of pure a-Si:H (see Section 5.1), which can be divided into three parts. First, one has to obtain a realistic description of the amorphous silicon network by any of the described procedures. Then, hydrogen has to be incorporated, which can form a lot of structural complexes [152, 153, 154, 155, 160, 161]. Thirdly, defects such as dangling bonds, floating bonds [162], but also vacancies [150, 163] have to be identified and either be removed or added in dependence of whether one wants to study them or not. Overall, this leads to a variety of structural effects, which could explain in some way the discrepancy for the  $\alpha$ -parameter. With respect to this point, it would be desirable to have a broader range of statistics for each of these aspects. However, since this would also require a lot of computation time, one should also consider alternative strategies. First, it can be beneficial to study the change of structural properties under an external physical influence. One example for such an approach is the change of the EPR-parameters under the influence of hydrostatic strain, which will be discussed in the next subsection. Secondly, it would be very helpful to have an overview of the atomic structures used in publications in the form of a database (comparable to the database for EPR-centers in semiconductors [164]). This would make it convenient to separate structural features specific to the generational method from those which are of a more universal character. Differences between both could then also be identified by applying new theoretical techniques (such as the GIPAW-formalism) as they become available.

A second important finding of a recent multi-band EPR-study [27] is that the number of Si atoms with a resolved hyperfine interaction  $>100$  MHz is about 2 rather than 1 for an ideal db-defect. This suggests that a more delocalized defect complex such as the floating bond (fb) contributes to the observed EPR-spectrum. In principle, this is reasonable since they appear naturally in theoretical simulations on an equal footing

to dangling bonds [135, 165, 166, 167]. It is also clear that in a real material both, dangling and floating bonds, occur and possibly also interact with each other. Thus the true problem consists in finding the defect with the most significant influence on the EPR-signal. However, we have seen that the a-Si:H db-defect originates from a variety of different local structures, and therefore one would expect the same thing for the floating bond. Consequently, one would assume that these defects are on average more delocalized, but there is no obvious reason why only two silicon atoms should have a strong hyperfine coupling. Indeed, theoretical calculations of the hyperfine parameters [140, 165] support the picture of a complex spin distribution for floating bonds. Furthermore, neither our classification of not-triply coordinated nor the one of delocalized defects (Table 5.1) yields a clear indication of a systematic shift towards significantly smaller  $a$ -values. Besides that, a fb-defect ensemble should yield a  $g$ -distribution shifted to larger  $g$ -values, since theoretical calculation have shown that the defect level is closer to the conduction-band edge [166, 167]. It should also have a lower  $b$ -parameter, which most likely means that the agreement between theory and experiment gets worse compared to the db-defect (for which  $\Delta b = 2$  MHz). Overall, we can take from this that the fb-defect cannot be the only reason for the experimental  $a$ -shift.

It is however possible that a mixture of fb- and db-models comes closer to the experimental observations. Even though this might also be the more realistic description, it would make it hard to identify crucial facets, since one would tremendously increase the number of spin-distribution configurations. Furthermore, it is unclear how to determine the right ratio between fb- and db-models.

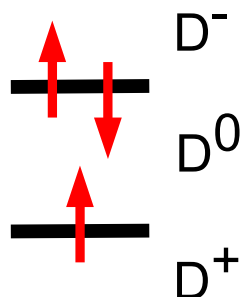
In principle, what the experimental results indicate is not just a simple delocalization of spin, but rather a coupling between two silicon atoms. Thinking along this lines, there are two possible scenarios. First, there could be some kind of coupling between nearby dangling bonds, as they appear in theoretical simulations [147, 168, 169] and modelling of the light-induced defect-creation [158]. However, this also addresses the question of stability, since two dangling bonds too close together will likely form a new bond. The second scenario is inspired by the finding that a-Si regions of strained bonds can also act as traps for charge carriers [170, 171]. Here one can imagine a situation in which a long Si-Si bond (with an appropriate geometrical distortion) leads to a localization of unpaired electrons. For completeness, we mention that it is possible that these weak Si-Si bonds are charged, even though corresponding cluster-calculations showed that these defects are related to other  $g$ -values appearing in the light-induced ESR-spectrum [128, 172].

## 5.4.2 Charging

It is also important to study the properties of existing defect ensembles, since we can learn from this how sensitive the EPR-parameters are to effects like charging or external influences such as hydrostatic strain. This gives new insights in the structural characteristics of the material, and can be useful for finding the relevant mechanisms behind the theory-experiment discrepancy.

First let us consider the charge stability of the dangling bond. A db-state can exist in

Positive  $U$



Negative  $U$

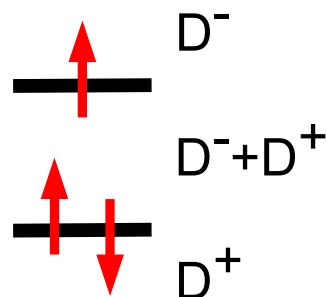


Figure 5.11: Energy levels for positive and negative correlation energy  $U$ .

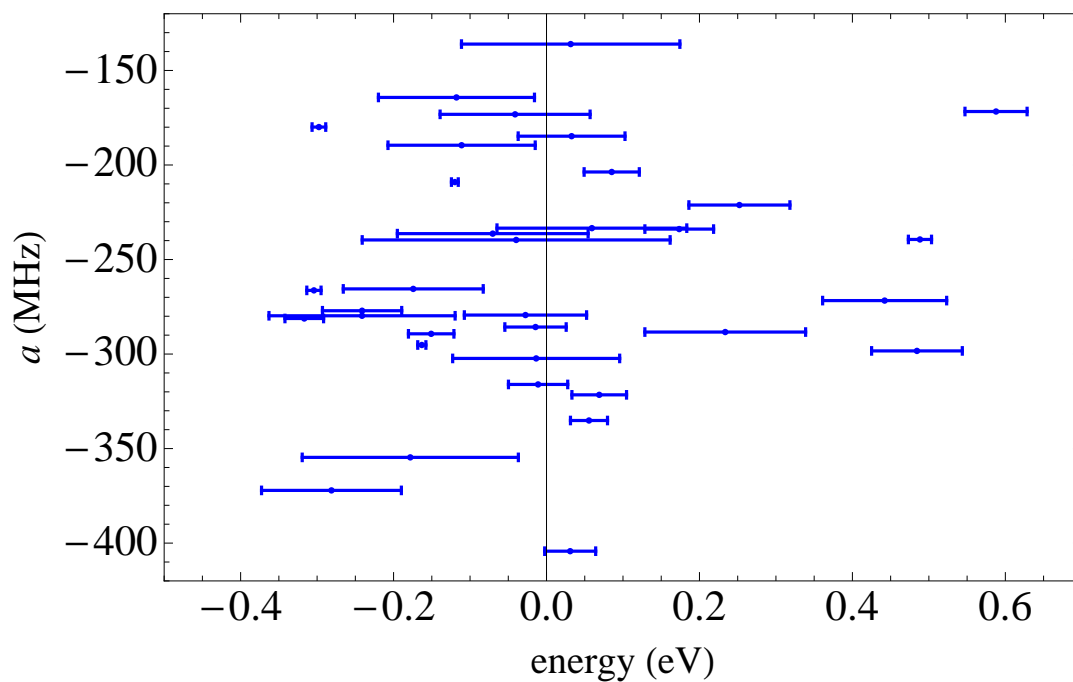


Figure 5.12: Correlation between the isotropic hyperfine parameter and the charge-stability region. The stability region of the neutral state is indicated by a bar for each defect. The Fermi energy defines the origin on the  $x$ -axis. Defects in the neutral state have a region of stability across the Fermi level.

three charge states  $D^+$ ,  $D^0$ , and  $D^-$  corresponding to zero, one or two electrons in the db-orbital [12, 156, 173, 174]. To get the stability range of the neutral, EPR-active state we have to compute the correlation energy  $U$ , which is defined as the difference between the charge-transition levels  $\epsilon^{(0/-)}$  and  $\epsilon^{(0/+)}$ . Charge-transition levels correspond to specific values of the electron chemical potential for which two charge states have equal formation energies. They are defined by the total energies of the defect system  $E_T^D$  in the charge states  $q$ ,  $q'$  referenced to the valence-band maximum  $E_V$

$$\epsilon^{(q/q')} = \frac{E_T^{D,q} - E_T^{D,q'}}{q' - q} - E_V$$

Physically,  $U$  characterizes two situations of the defect reaction  $2D^0 \rightleftharpoons D^+ + D^-$  as sketched in Figure 5.11. If it is negative, two neutral dangling bonds convert into  $D^+$  and  $D^-$ , which are not spin-active. Thus, the detection of the neutral, EPR-active state requires a positive correlation energy. With respect to this, it is interesting that only 37% have a positive  $U$ -value. To exploit the relation between stability and isotropic coupling in more detail, we reference  $U$  to the Fermi energy. The Fermi level is consistently determined from our charge-transition levels by the condition of charge neutrality for the complete ensemble. From Figure 5.12 we see that only 11 db-models are stable in the neutral charge state, whereas the majority of defects only exist in the negative or positive charge state in thermal equilibrium. This finding is in agreement with the defect-pool model [175]. However, there is no correlation between the sub-ensemble of stable dangling bonds and the isotropic hyperfine coupling, since they are homogeneously distributed over the parameter range.

### 5.4.3 Strain

For the c-Si models, we have seen that the effect of strain on the hyperfine parameters is characterized by the interplay of band gap and hybridization (Chapter 4.4.3). To obtain a better understanding of the db-stability, it is interesting to carry out an analogous study for the amorphous db-models. For that reason, we apply again hydrostatic strain to our db-models. We only consider the smaller 64Si-7H supercells, since the relaxation of a db-model at different lattice constants costs a lot of computation time. However, we do not expect drastic differences for the larger supercells, because the EPR-parameter statistics of both are quite similar (Table 5.1).

One general aspect of the resulting strain dependence is their larger structural sensitivity. Consequently there are small relaxational effects even at the ideal lattice constant. Furthermore, in particular for large strains (tensile or compressive) one observes a redistribution of the spin density, and the dangling bond hops from one to the other atom. To take this into account, we consider for each model only the range in which the dangling bond is stable. Practically, this is implemented by first determining the db-atom at the ideal lattice constant. Then one monitors whether it is still the atom with the largest  $a$ -value as a function of the applied strain. Furthermore, since the bonding parameters of Si-H bonds cannot be compared to Si-Si bonds, we only consider those cases in which

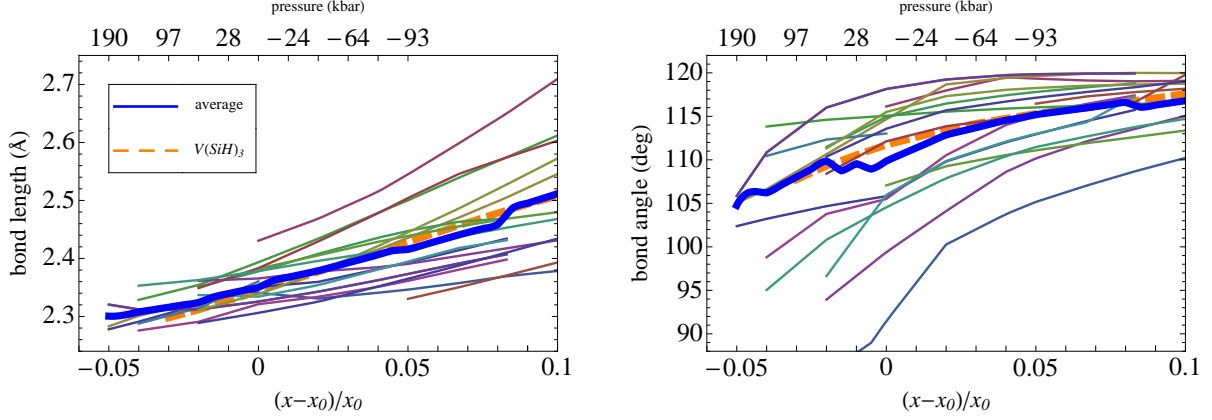


Figure 5.13: The dependence of bond length and bond angle on the elongation  $x$  from the ideal lattice constant  $x_0$ . For the rhombic supercells,  $x_0$  corresponds to the mean lattice constant of the three axis ( $x_1, x_2, x_3$ ). The bond parameters are defined by the average over the three nearest neighbors. The thick blue line indicates the trend for the mean value. Kinks in this curve can occur when the number of included db-models changes with respect to strain. For comparison the thick orange line shows the dependence of the c-Si  $V(\text{SiH}_3)$  db-model. Values of pressure are included for the experimentally relevant range of strains.

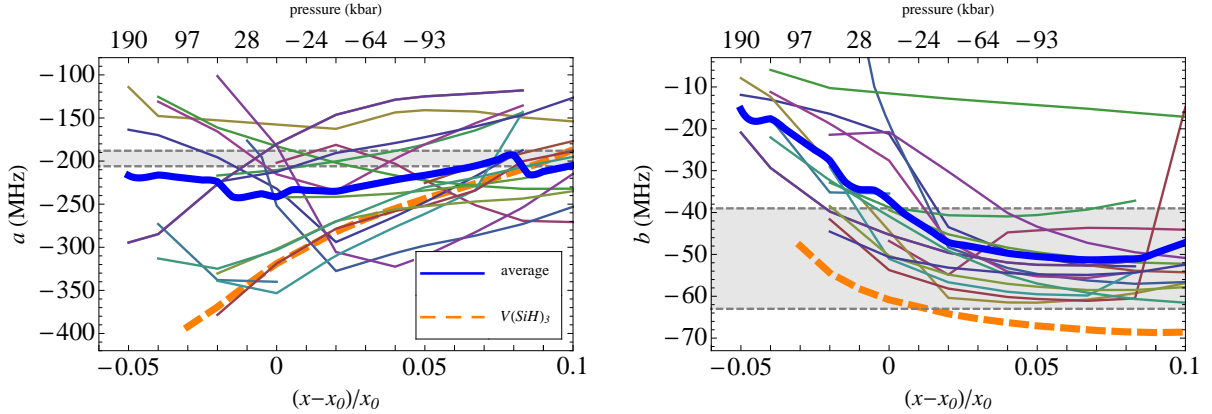


Figure 5.14: The dependence of the hyperfine parameters on the elongation  $x$  from the ideal lattice constant  $x_0$ . For the rhombic supercells,  $x_0$  corresponds to the mean lattice constant of the three axis ( $x_1, x_2, x_3$ ). The bond parameters are defined by the average over the three nearest neighbors. The thick blue line indicates the trend for the mean value. Kinks in this curve can occur when the number of included db-models changes with respect to strain. For comparison, the thick orange line shows the dependence of the c-Si  $V(\text{SiH}_3)$  db-model. Values of pressure are included for the experimentally relevant range of strains.

the dangling bond has 3 silicon atoms as neighbors.

First let us look at the structural parameters of the db-atom as depicted in Figure 5.13. For the mean bond length we recognize that the amorphous db-models show on average the same trends as their crystalline counterparts. In particular, for compressive strain they have a comparable range of stability, and besides that, the increase of  $l$  for tensile strain is on the same order. Significant deviations from this are only observed for  $l > 2.6 \text{ \AA}$  when the model is not triply coordinated at the ideal lattice constant. A similar correspondence is also found for the bond angle  $\alpha$  in the case of tensile strain, since the a-Si:H db-models also favor a rather planar geometry. On the other hand, the diverse picture for compressive strain can be explained by inhomogeneities in the three bond angles which are not captured by the mean parameter. To exemplify this point let us look at the db-model with the largest deviation from the overall trend ( $\alpha = 109.6^\circ$  for  $\Delta x = 0.1$ ). Even though the stability of the dangling bond is very sensitive to tensile strain, it is three-fold coordinated and localized at the ideal lattice constant, i.e. a true db-model. At  $x = x_0$ , the bond angles vary by  $\pm 5^\circ$  from the right angle, and for large tensile strain ( $\Delta x = 0.1$ ) this tendency is enhanced, since in this case  $\alpha$  is in between 101 and 116 Degrees. The large variation among the three bond angles illustrates that the mean value is indeed only an approximative measure of an actually more complex bonding geometry. Despite this deficiency, we learn from Figure 5.13 that the bond parameters in general show the same trends as for the crystalline db-models, and that the bond angles are more sensitive to compressive strain than the bond lengths.

The isotropic hyperfine interaction has no clear trend (Figure 5.14), since we are considering all db-models (despite their coordination and spin localization) on equal footing. Consequently, it can happen that the spin density at the db-atom increases or decreases with applied strain, or that it is rather delocalized over the whole range. In one case, the dangling bond is only stable in between  $\Delta x = [-0.004, 0]$  before it starts to bond to hydrogen. On the other hand, the trend for the  $b$ -parameter is rather homogeneous for almost all models and corresponds to the one observed for the crystalline models with a shift of about 20 MHz. The only exceptions are caused by delocalization, under-coordination and a very small bond angle. However, the true information here is obtained again from the averaged trends. The  $a$ -parameter stays rather constantly in between 200 and 250 MHz throughout the strain range, and there is no obvious dependence on the magnitude of the applied strain. This aspect distinguishes the a-Si:H-db from their crystalline counterparts, and it might be explained by their different origins. The crystalline dangling bond is related to a vacancy complex, which essentially means that it is characterized by the interplay of electronic effects (due to impurities) and the local defect geometry. On the other hand, the amorphous dangling bond is a network defect, which is consequently essentially influenced by spin delocalization into the local environment as well as structural features of the wider surrounding. Thus the trend for the  $a$ -parameter can be explained by spin delocalization for small strains and the planar local db-structure for large tensile strain. This picture is also consistent with the trend for the anisotropic hyperfine coupling, which shows a gradual increase in  $p$ -character of the db-orbital with increasing strain. Overall, we learn from this that for compressive strains delocalization is important and for tensile strains the db-character is enhanced.

Let us now discuss the main implication of this conceptual study for the discrepancy in the  $a$ -parameter. Compressive strain on the order of a few percent can lower the isotropic coupling, so that the difference between both becomes reasonable. However, in this case one should also observe a corresponding shift in the  $b$ -parameter, i.e. the agreement between theory and experiment should become better as well. Since this is not observed, one cannot consider strain as an exclusive explanation. But at least it gives a clear perspective that strain might have an observable influence on the hyperfine parameters, and consequently may play an important role for the defect mechanisms in the material.

Furthermore, it addresses the following questions for future experiments. First, the value for the anisotropic coupling needs to be clarified, since it currently deviates in between [-39,-63] MHz among different experiments (Table 5.1). This is a very important point, since we have seen that a low and a large anisotropic coupling correspond to two opposite strain situations with rather similar isotropic couplings. Secondly, the strain dependence of the hyperfine parameters needs to be measured, since we could then compare the experimental and theoretical trends at least quantitatively. This would yield further insights into the quality of the current theoretical models. Two aspects are important here. First, the study of biaxial strain [176] is probably more realistic than hydrostatic strain. However, test calculations did not yield significant deviations from the case of uniaxial strain. Secondly, the suggested experiment appears to be feasible and corresponding guiding principles do exist. For example, a recent semi-empirical model [177] was able to relate the deposition conditions to internal stress. It suggested that stress originates from the balance between deposition ion momentum (particularly important for compressive stress) and hydrogen void destruction (significant for tensile stress).

## 5.5 Summary and Outlook

In this chapter we have shown that the concept of the a-Si:H db-defect is far more complex than previously assumed [44, 45]. By comparison with a recent multi-frequency EPR-study [27, 28] we were able to clarify some of the experimental observations such as the rhombicity of the  $g$ -tensor or the uniaxiality of the  $A$ -tensor. We have also seen that the  $g$ -tensor can be quite similar for different kinds of spin localization. Furthermore, the removal of one hydrogen from a pure a-Si:H model does not necessarily result in a true localized db-defect, but can relax towards not-triply or delocalized defects. Localized db-models tend to have three silicon backbond neighbors with a rather homogeneous bond-length distribution. On the contrary, their bond angles do have a rather broad distribution, and this is the main reason for the rather complex relation between hyperfine- and structural parameters. In contrast to the crystalline environment, a large superhyperfine interaction is not restricted to the second-nearest backbond neighbor but can occur at both sides of the dangling bond. A similar result is found for the  $a$ -distribution of hydrogen. Both findings emphasize that the amorphous dangling bond is a network defect, which is most likely to occur for suitable geometrical conditions.

However, the lower experimentally observed isotropic hyperfine coupling as well as the number of silicon atoms with an isotropic coupling larger than 100 MHz remain as open problems. On the other hand, we have shown that strain could have an important influence on the hyperfine parameters. With respect to this assumption, a more reliable experimental value for the  $b$ -parameter is decisive, since it would clarify whether the observed hyperfine couplings originate from spin delocalization or from dangling bonds in a planar geometry. Overall, these open questions yield the following perspective for future experimental and theoretical research.

Experimentally, it is necessary to repeat the multi-frequency EPR-approach [27, 28] for  $^{29}\text{Si}$ -enriched samples<sup>1</sup> [127]. First, this would yield further insights into the spin localization and elucidate the number of silicon atoms with  $a > 100$  MHz, which is still under debate [27, 44, 45]. Secondly, a thoroughly analysis of the experiments so far [27, 44, 45] has to be carried out to better understand the large variations in the anisotropic coupling. For that purpose, one will not only have to look at the experimental conditions but also at the used spectrum-fitting procedures. In addition to that, it would be interesting to see whether the theoretical strain dependence of the hyperfine parameters can be verified experimentally.

Besides these rather specific aspects, it would also be important to investigate whether only a subset of possible db-configurations gives rise to the small  $a$ -coupling and thus is observed in EPR. For that purpose, one should alter the experimental conditions in a controlled way. For example, one should vary the method to create dangling bonds (e.g. via light, electron bombardment, currents) at low temperatures to reduce possible equilibration after the creation. Another possibility consists in systematically varying the hydrogen or defect concentration in the samples. The kinetic or thermodynamic stability of the db-ensemble can be investigated by recording the EPR-spectrum at different temperatures in a similar way as has been done for vacancy db-defects in c-Si [41, 42, 105].

From a theoretical point of view, the following tasks lie ahead. First, it would be desirable to increase the number of db-models, so that the statistics become more reliable. Furthermore, one should compute the EPR-parameters of other potentially important defect complexes (floating bond, coupled dangling bonds, etc.). As for our study it will be necessary to consider a sufficiently large defect ensemble, because defect complexes in the amorphous environment will always have a certain structural diversity. Here again, the bottleneck will be the computationally expensive generation of the corresponding a-Si:H-models. Besides that, it will be an ongoing task to improve the structural modelling of the amorphous phase. In the case of a-Si:H, one key question is the incorporation of hydrogen into the disordered network. For that purpose it could be beneficial to compute the NMR-parameters of a-Si:H models by using the GIPAW-formalism, then comparing the results for example with other rudimentary theoretical studies [150, 163].

A complementary approach consists in studying the influence of external parameters on a defect ensemble. As we have shown for strain, this yields new insights into the structural characteristics of the defect and can raise new questions, which can be then

---

<sup>1</sup>The natural abundance of silicon is 4.69% [31]. Isotope-enriched samples contain 9.1-93% [44, 45].

tested experimentally. One open aspect of the strain-dependence is, whether floating bonds are more likely to form for compressive strain and dangling bonds for tensile strain. One heuristic argument for that is that the coordination should naturally increase for shorter bond lengths and decrease for larger ones. In this context, we mention that at least for shear deformation of a-Si one observes an increase of 5-fold coordination with increasing strain [178].

It is difficult to predict whether it will be possible to resolve all open questions regarding the Staebler-Wronski effect, i.e. the light-induced degradation of a-Si:H solar cells. However, as mentioned in the introduction (Chapter 1), several strategies exist to reduce its influence on the conversion efficiency. Future research will doubtlessly lead to further improvements. From our work, the most important lesson is that the amorphous dangling bond differs from its molecular and crystalline counterpart substantially. It appears spontaneously at suitable geometrical distortions in the network, and the local defect structure plays an important role in the db-formation. Yet, this theoretical notion is missing some relevant aspects and can explain the observed EPR-parameters only in part. To resolve the remaining discrepancies between theory and experiment and bring them to quantitative agreement will be a key challenge for the theoretical modelling of the Staebler-Wronski effect in the future.

# Bibliography

- [1] F. BIROL, editor, *World energy outlook 2009*, IEA, 2009.
- [2] INTERNATIONAL ENERGY AGENCY, *Technology Roadmap: Solar Photovoltaic Energy*, Technical report, 2010, [doi:10.1787/9789264088047-en](https://doi.org/10.1787/9789264088047-en).
- [3] B. SINHA, *Current Science* **100**, 654 (2011).
- [4] INTERNATIONAL ENERGY AGENCY, *Technology Roadmap: Concentrating Solar Power*, Technical report, 2010, [doi:10.1787/9789264088139-en](https://doi.org/10.1787/9789264088139-en).
- [5] G. L. PEARSON, *Am. J. Phys.* **25**, 591 (1957), [doi:10.1119/1.1934565](https://doi.org/10.1119/1.1934565).
- [6] J. L. STONE, *Physics Today* **46**, 22 (1993), [doi:10.1063/1.881362](https://doi.org/10.1063/1.881362).
- [7] F. HERRMANN and P. WÜRFEL, *Am. J. Phys.* **74**, 591 (2006), [doi:10.1119/1.2192786](https://doi.org/10.1119/1.2192786).
- [8] A. LUQUE and S. HEGEDUS, *Handbook of Photovoltaic Science and Engineering*, Wiley-VCH, 2003, [doi:10.1002/0470014008](https://doi.org/10.1002/0470014008).
- [9] P. Y. YU and M. CARDONA, *Fundamentals of semiconductors*, Springer, 1996.
- [10] V. AVRUTIN, N. IZYUMSKAYA, and H. MORKOÇ, *Superlattices and Microstructures* **49**, 337 (2011), [doi:10.1016/j.spmi.2010.12.011](https://doi.org/10.1016/j.spmi.2010.12.011).
- [11] S. KASAP and P. CAPPER, editors, *Springer Handbook of electronic and photonic materials*, Springer, 2006.
- [12] R. A. STREET, *Hydrogenated Amorphous Silicon*, Cambridge University Press, 1991.
- [13] A. V. SHAH, R. PLATZ, and H. KEPPNER, *Sol. Energ. Mat. Sol. Cells* **38**, 501 (1995), [doi:10.1016/0927-0248\(94\)00241-X](https://doi.org/10.1016/0927-0248(94)00241-X).
- [14] W. SCHOCKLEY and H. J. QUEISSER, *J. Appl. Phys.* **32**, 510 (1961), [doi:10.1063/1.1736034](https://doi.org/10.1063/1.1736034).
- [15] R. BRENDL, *Thin-Film Crystalline Silicon Solar Cells*, Wiley-VCH, 2003, [doi:10.1002/35276035304](https://doi.org/10.1002/35276035304).
- [16] C. S. SOLANKI and G. BEAUCARNE, *Energy for Sustainable Development* **11**, 17 (2007), [doi:10.1016/S0973-0826\(08\)60573-6](https://doi.org/10.1016/S0973-0826(08)60573-6).

- [17] A. SHAH, P. TORRES, R. TSCHARNER, N. WYRSCH, and H. KEPNER, *Science* **285**, 692 (1999), [doi:10.1126/science.285.5428.692](https://doi.org/10.1126/science.285.5428.692).
- [18] M. KONAGAI, *Jap. J. Appl. Phys.* **50**, 030001 (2011), [doi:10.1143/JJAP.50.030001](https://doi.org/10.1143/JJAP.50.030001).
- [19] M. BRODSKY, *Introduction, Amorphous semiconductors*, Springer, 1985.
- [20] R. B. BERGMANN and J. H. WERNER, *Thin Solid Films* **403**, 162 (2002), [doi:10.1016/S0040-6090\(01\)01556-5](https://doi.org/10.1016/S0040-6090(01)01556-5).
- [21] D. E. CARLSON and C. R. WRONSKI, *Appl. Phys. Lett.* **28**, 671 (1976), [doi:10.1063/1.88617](https://doi.org/10.1063/1.88617).
- [22] D. L. STAEBLER and C. R. WRONSKI, *Appl. Phys. Lett.* **31**, 292 (1977), [doi:10.1063/1.89674](https://doi.org/10.1063/1.89674), [doi:10.1063/1.89674](https://doi.org/10.1063/1.89674).
- [23] A. KOŁODZIEJ, *Opt. El. Rev.* **12**, 21 (2004).
- [24] T. SHIMIZU, *Jap. J. Appl. Phys.* **43**, 3257 (2004), [doi:10.1143/JJAP.43.3257](https://doi.org/10.1143/JJAP.43.3257).
- [25] H. FRITZSCHE, *Ann. Rev. Mat. Res.* **31**, 47 (2001), [doi:10.1146/annurev.mat.sci.31.1.47](https://doi.org/10.1146/annurev.mat.sci.31.1.47).
- [26] J. YANG, A. BANERJEE, and S. GUHA, *Appl. Phys. Lett.* **70**, 2975 (1997), [doi:10.1063/1.118761](https://doi.org/10.1063/1.118761).
- [27] M. FEHR, *Paramagnetic defects in hydrogenated amorphous silicon: an advanced Electron Paramagnetic Resonance study*, PhD thesis, FU Berlin, 2011.
- [28] M. FEHR, A. SCHNEGG, B. RECH, K. LIPS, O. ASTHAKOV, F. FINGER, G. PFANNER, C. FREYSOLDT, J. NEUGEBAUER, R. BITTL, and C. TEUTLOFF, *Phys. Rev. B* **84**, 245203 (2011), [doi:10.1103/PhysRevB.84.245203](https://doi.org/10.1103/PhysRevB.84.245203).
- [29] C. S. SUNANDANA, *Bull. Mater. Sci.* **21** (1998), [doi:10.1007/BF02745018](https://doi.org/10.1007/BF02745018).
- [30] J. M. SPAETH and H. OVERHOF, *Point defects in semiconductors and insulators*, Springer, 2003, [doi:10.1002/3527601678](https://doi.org/10.1002/3527601678).
- [31] J. A. WEIL and J. R. BOLTON, *Electron paramagnetic resonance*, Wiley, 2007, [doi:10.1002/9780470084984.indauth](https://doi.org/10.1002/9780470084984.indauth).
- [32] P. H. RIEGER, *Electron spin resonance*, RSC Publishing, 2007.
- [33] A. G. LUNDIN and V. E. ZORIN, *Physics Uspekhi* **50**, 1053 (2007), [doi:10.1070/PU2007v050n10ABEH006308](https://doi.org/10.1070/PU2007v050n10ABEH006308).
- [34] S. WURMEHL and J. KOHLHEPP, *J. Phys. D* **41**, 173002 (2008), [doi:10.1088/0022-3727/41/17/173002](https://doi.org/10.1088/0022-3727/41/17/173002).

- [35] B. M. HOFFMAN, *J. Phys. Chem.* **98**, 11657 (1994), [doi:10.1021/j100096a006](https://doi.org/10.1021/j100096a006).
- [36] A. ROCKENBAUER and P. SIMON, *J. Mag. Res.* **22**, 243 (1976), [doi:10.1016/0022-2364\(76\)90299-7](https://doi.org/10.1016/0022-2364(76)90299-7).
- [37] F. K. KNEUBÜHL, *Phys. kond. Mat.* **1**, 410 (1963), [doi:10.1007/BF02422740](https://doi.org/10.1007/BF02422740).
- [38] D. J. GRIFFITHS, *Introduction to quantum mechanics*, Prentice Hall, Inc., 1995.
- [39] W. DEMTRÖDER, *Atoms, molecules and photons*, Springer, 2006.
- [40] C. VAN DER WALLE and P. E. BLÖCHL, *Phys. Rev. B* **47**, 4244 (1993), [doi:10.1103/PhysRevB.47.4244](https://doi.org/10.1103/PhysRevB.47.4244).
- [41] P. JOHANNESSEN, B. B. NIELSEN, and J. R. BYBERG, *Phys. Rev. B* **61**, 4659 (2000), [doi:10.1103/PhysRevB.61.4659](https://doi.org/10.1103/PhysRevB.61.4659).
- [42] G. D. WATKINS and J. W. CORBETT, *Phys. Rev.* **134**, A1359 (1964), [doi:10.1103/PhysRev.134.A1359](https://doi.org/10.1103/PhysRev.134.A1359).
- [43] M. SPRENGER, S. H. MULLER, E. G. SIEVERTS, and C. A. J. AMMERLANN, *Phys. Rev. B* **35**, 1566 (1987), [doi:10.1103/PhysRevB.35.1566](https://doi.org/10.1103/PhysRevB.35.1566).
- [44] M. STUTZMANN and D. K. BIEGELSEN, *Phys. Rev. B* **40**, 9834 (1989), [doi:10.1103/PhysRevB.40.9834](https://doi.org/10.1103/PhysRevB.40.9834).
- [45] T. UMEDA, S. YAMASAKI, J. ISOYA, and K. TANAKA, *Phys. Rev. B* **59**, 4849 (1999), [doi:10.1103/PhysRevB.59.4849](https://doi.org/10.1103/PhysRevB.59.4849).
- [46] A. H. EDWARDS and W. B. FOWLER, *Phys. Rev. B* **41**, 19816 (1990), [doi:10.1103/PhysRevB.41.10816](https://doi.org/10.1103/PhysRevB.41.10816).
- [47] J. KOHANOFF, *Electronic structure calculations for solids and molecules*, Cambridge University Press, 2006, [doi:10.2277/0521815916](https://doi.org/10.2277/0521815916).
- [48] R. M. MARTIN, *Electronic structure*, Cambridge University Press, 2004, [doi:10.2277/0521782856](https://doi.org/10.2277/0521782856).
- [49] W. M. C. FOULKES, L. MITAS, R. J. NEEDS, and G. RAJAGOPAL, *Rev. Mod. Phys.* **73**, 33 (2001), [doi:10.1103/RevModPhys.73.33](https://doi.org/10.1103/RevModPhys.73.33).
- [50] E. A. CARTER, *Science* **321**, 800 (2008), [doi:10.1126/science.1158009](https://doi.org/10.1126/science.1158009).
- [51] K. CAPELLE, *Braz. J. Phys.* **36**, 1318 (2006), [doi:10.1590/S0103-97332006000700035](https://doi.org/10.1590/S0103-97332006000700035).
- [52] L. HUNG and E. A. CARTER, *Chem. Phys. Lett.* **475**, 163 (2009), [doi:10.1016/j.cplett.2009.04.059](https://doi.org/10.1016/j.cplett.2009.04.059).

- [53] G. ONIDA, L. REINING, and A. RUBIO, *Rev. Mod. Phys.* **74**, 601 (2002), doi:[10.1103/RevModPhys.74.601](https://doi.org/10.1103/RevModPhys.74.601).
- [54] A. J. FREEMAN and E. WIMMER, *Ann. Rev. Mat. Sci.* **25**, 7 (1995), doi:[10.1146/annurev.ms.25.080195.000255](https://doi.org/10.1146/annurev.ms.25.080195.000255).
- [55] S. BLÜGEL, Density Functional Theory in Practice, in *Computational Condensed Matter Physics : Lecture Manuscripts of the 37th Spring School of the Institute of Solid State Research*, volume 32 of *Schriften des Forschungszentrums Jülich Matter and Materials*, 2006.
- [56] M. C. PAYNE, M. P. TETER, D. C. ALLAN, T. A. ARIAS, and J. D. JOANNOPOULOS, *Rev. Mod. Phys.* **64**, 1045 (1992), doi:[10.1103/RevModPhys.64.1045](https://doi.org/10.1103/RevModPhys.64.1045).
- [57] A. E. MATTSSON, P. A. SCHULTZ, M. P. DESJARLAIS, T. R. MATTSSON, and K. LEUNG, *Mod. Sim. Mat. Sci. Eng.* **13**, R1 (2005), doi:[10.1088/0965-0393/13/1/R01](https://doi.org/10.1088/0965-0393/13/1/R01).
- [58] M. FUCHS and M. SCHEFFLER, *Comp. Phys. Comm.* **119**, 67 (1999), doi:[10.1016/S0010-4655\(98\)00201-X](https://doi.org/10.1016/S0010-4655(98)00201-X).
- [59] F. TRAN and P. BLAHA, *Phys. Rev. Lett.* **102**, 226401 (2009), doi:[10.1103/PhysRevLett.102.226401](https://doi.org/10.1103/PhysRevLett.102.226401).
- [60] J. P. PERDEW, K. BURKE, and M. ERNZERHOF, *Phys. Rev. Lett.* **77**, 3865 (1996), doi:[10.1103/PhysRevLett.77.3865](https://doi.org/10.1103/PhysRevLett.77.3865).
- [61] C. VAN DE WALLE and A. JANOTTI, *Phys. Stat. Sol. B* **248**, 19 (2011), doi:[10.1002/pssb.201046290](https://doi.org/10.1002/pssb.201046290).
- [62] W. R. LAMBRECHT, *Phys. Stat. Sol. B* **248**, 1547 (2011), doi:[10.1002/pssb.201046327](https://doi.org/10.1002/pssb.201046327).
- [63] C. W. M. CASTLETON, A. HÖGLUND, and M. S., *Modelling Simul. Mater. Sci. Eng.* **17**, 084003 (2009), doi:[10.1088/0965-0393/17/8/084003](https://doi.org/10.1088/0965-0393/17/8/084003).
- [64] J. SHIM, E. J. LEE, Y. J. LEE, and R. M. NIEMINEN, *Phys. Rev. B* **71**, 245204 (2005), doi:[10.1103/PhysRevB.71.245204](https://doi.org/10.1103/PhysRevB.71.245204).
- [65] M. KAUPP, M. BÜHL, and V. G. MALKIN, editors, *Calculation of NMR and EPR parameters*, Wiley-VCH, 2004, doi:[10.1002/3527601678](https://doi.org/10.1002/3527601678).
- [66] F. MAURI, B. G. PFROMMER, and S. G. LOUIE, *Phys. Rev. B* **60**, 2941 (1999), doi:[10.1103/PhysRevB.60.2941](https://doi.org/10.1103/PhysRevB.60.2941).
- [67] C. J. PICKARD and F. MAURI, *Phys. Rev. B* **63**, 245101 (2001), doi:[10.1103/PhysRevB.63.245101](https://doi.org/10.1103/PhysRevB.63.245101).

- [68] P. E. BLÖCHL, *Phys. Rev. B* **50**, 17953 (1994), [doi:10.1103/PhysRevB.50.17953](https://doi.org/10.1103/PhysRevB.50.17953).
- [69] N. A. W. HOLZWARTH, A. R. TACKETT, and G. E. MATTHEWS, *Comp. Phys. Comm.* **135**, 329 (2001), [doi:10.1016/S0010-4655\(00\)00244-7](https://doi.org/10.1016/S0010-4655(00)00244-7).
- [70] J. ENKOVAARA, C. ROSTGAARD, J. J. MORTENSEN, J. CHEN, M. DUŁAK, L. FERRIGHI, J. GAVNHOLT, C. GLINSVAD, V. HAIKOLA, H. A. HANSEN, H. H. KRISTOFFERSEN, M. KUISMA, A. H. LARSEN, L. LEHTOVAARA, M. LJUNGBERG, O. LOPEZ-ACEVEDO, P. G. MOSES, J. OJANEN, T. OLSEN, V. PETZOLD, N. A. ROMERO, J. STAUSHOLM-MØLLER, M. STRANGE, G. A. TRITSARIS, M. VANIN, M. WALTER, B. HAMMER, H. HÄKKINEN, G. K. H. MADSEN, R. M. NIEMINEN, J. K. NØRSKOV, M. PUSKA, T. T. RANTALA, J. SCHIØTZ, K. S. THYGESSEN, and K. W. JACOBSEN, *J. Phys.: Cond. Mat.* **22**, 253202 (2010), [doi:10.1088/0953-8984/22/25/253202](https://doi.org/10.1088/0953-8984/22/25/253202).
- [71] G. SCHRECKENBACH and T. ZIEGLER, *J. Phys. Chem. A* **101**, 3388 (1997), [doi:10.1021/jp963060t](https://doi.org/10.1021/jp963060t).
- [72] R. DECLERCK, V. VAN SPEYBROECK, and M. WAROQUIER, *Phys. Rev. B* **73**, 115113 (2006), [doi:10.1103/PhysRevB.73.115113](https://doi.org/10.1103/PhysRevB.73.115113).
- [73] J. AUTSCHBACH and T. ZIEGLER, *Coord. Chem. Rev.* **238**, 83 (2003), [doi:10.1016/S0010-8545\(02\)00287-4](https://doi.org/10.1016/S0010-8545(02)00287-4).
- [74] G. SCHRECKENBACH and T. ZIEGLER, *Theoretical Chemistry Accounts* **99**, 71 (1998), [doi:10.1007/s002140050306](https://doi.org/10.1007/s002140050306).
- [75] C. J. PICKARD and F. MAURI, *Phys. Rev. Lett.* **88**, 086403 (2002), [doi:10.1103/PhysRevLett.88.086403](https://doi.org/10.1103/PhysRevLett.88.086403).
- [76] S. SHARMA, S. PITTALIS, S. KURTH, S. SHALLCROSS, J. K. DEWHURST, and E. K. U. GROSS, *Phys. Rev. B* **76**, 100401(R) (2007), [doi:10.1103/PhysRevB.76.100401](https://doi.org/10.1103/PhysRevB.76.100401).
- [77] L. TRUFLANDIER, M. PARIS, and B. F., *Phys. Rev. B* **76**, 035102 (2007), [doi:10.1103/PhysRevB.76.035102](https://doi.org/10.1103/PhysRevB.76.035102).
- [78] L. PIELA, *Ideas of quantum chemistry*, Elsevier, 2007.
- [79] V. WEBER, M. IANNUZZI, S. GIANI, J. HUTTER, and R. DECLERCK, *J. Chem. Phys.* **131**, 014106 (2009), [doi:10.1063/1.3156803](https://doi.org/10.1063/1.3156803).
- [80] P. GIANNOZZI, S. BARONI, N. BONINI, M. CALANDRA, R. CAR, C. CAVAZZONI, D. CERESOLI, G. L. CHIAROTTI, M. COCOCCIONI, I. DABO, A. DAL CORSO, S. DE GIRONCOLI, S. FABRIS, G. FRATESI, R. GEBAUER, U. GERSTMANN, C. GOUGOUSSIS, A. KOKALJ, M. LAZZERI, L. MARTIN-SAMOS, N. MARZARI, F. MAURI, R. MAZZARELLO, S. PAOLINI, A. PASQUARELLO, L. PAULATTO, C. SBRACCIA, S. SCANDOLO, G. SCLAUZERO, A. P. SEITSONEN, A. SMOGUNOV,

- P. UMARI, and R. M. WENTZCOVITCH, *J. Phys.: Cond. Matter* **21**, 395502 (2009), [doi:10.1088/0953-8984/21/39/395502](https://doi.org/10.1088/0953-8984/21/39/395502).
- [81] D. CERESOLI, U. GERSTMANN, A. P. SEITSONEN, and F. MAURI, *Phys. Rev. B* **81**, 060409(R) (2010), [doi:10.1103/PhysRevB.81.060409](https://doi.org/10.1103/PhysRevB.81.060409).
- [82] E. S. KADANTSEV and T. ZIEGLER, *J. Chem. Phys. A* **113**, 1327 (2009), [doi:10.1021/jp805466c](https://doi.org/10.1021/jp805466c).
- [83] U. GERSTMANN, *Phys. Stat. Sol. B* **248**, 1319 (2011), [doi:10.1002/pssb.201046237](https://doi.org/10.1002/pssb.201046237).
- [84] J. AUTSCHBACH, S. PATCHKOVSKII, and B. PRITCHARD, *J. Chem. Theory Comp.* **7**, 2175 (2011), [doi:10.1021/ct200143w](https://doi.org/10.1021/ct200143w).
- [85] S. BLÜGEL, H. AKAI, R. ZELLER, and P. H. DEDERICHS, *Phys. Rev. B* **35**, 3271 (1987), [doi:10.1103/PhysRevB.35.3271](https://doi.org/10.1103/PhysRevB.35.3271).
- [86] P. E. BLÖCHL, *Phys. Rev. B* **62**, 6158 (2000), [doi:10.1103/PhysRevB.62.6158](https://doi.org/10.1103/PhysRevB.62.6158).
- [87] G. PFANNER, C. FREYSOLDT, and J. NEUGEBAUER, *Phys. Rev. B* **83**, 144110 (2011), [doi:10.1103/PhysRevB.83.144110](https://doi.org/10.1103/PhysRevB.83.144110).
- [88] C. VAN DE WALLE, *Phys. Rev. Lett.* **64**, 669 (1990), [doi:10.1103/PhysRevLett.64.669](https://doi.org/10.1103/PhysRevLett.64.669).
- [89] O. YAZYEV, I. TAVERNELLI, L. HELM, and U. RÖTHLISBERGER, *Phys. Rev. B* **71**, 115110 (2005), [doi:10.1103/PhysRevB.71.115110](https://doi.org/10.1103/PhysRevB.71.115110).
- [90] M. S. BAHRAMY, M. H. F. SLUITER, and Y. KAWAZOE, *Phys. Rev. B* **76**, 035124 (2007), [doi:10.1103/PhysRevB.76.035124](https://doi.org/10.1103/PhysRevB.76.035124).
- [91] V. FILIDOU, D. CERESOLI, J. J. L. MORTON, and F. GIUSTINO, (2012), [arXiv:1201.5849v1](https://arxiv.org/abs/1201.5849v1).
- [92] L. HERMOSILLA, P. CALLE, J. M. GARCIA DE LA VEGA, and C. SIEIRO, *J. Phys. Chem. A* **109**, 1114 (2005), [doi:10.1021/jp0466901](https://doi.org/10.1021/jp0466901).
- [93] S. KOSSMANN, B. KIRCHNER, and F. NEESE, *Mol. Phys.* **105**, 2049 (2007), [doi:10.1080/00268970701604655](https://doi.org/10.1080/00268970701604655).
- [94] E. S. KADANTSEV and T. ZIEGLER, *Magn. Reson. Chem.* **48**, S2 (2010), [doi:10.1002/mrc.2655](https://doi.org/10.1002/mrc.2655).
- [95] K. NAKAMURA, N. MASAKI, S. SATO, and K. SHIMOKOSHI, *J. Chem. Phys.* **83**, 4504 (1985), [doi:10.1063/1.449018](https://doi.org/10.1063/1.449018).
- [96] R. J. VAN ZEE, R. F. FERRANTE, and W. WELTNER, *J. Chem. Phys.* **83**, 6181 (1985), [doi:10.1063/1.449614](https://doi.org/10.1063/1.449614).

- [97] D. A. DRABOLD and S. ESTREICHER, editors, *Theory of Defects in Semiconductors*, volume 104 of *Topics in Applied Physics*, Springer, 2007, doi:10.1007/11690320.
- [98] A. F. WRIGHT, *Phys. Rev. B* **74**, 165116 (2006), doi:10.1103/PhysRevB.74.165116.
- [99] M. G. GANCHENKOVA, L. E. OIKKONEN, V. A. BORODIN, S. NICOLAYSEN, and R. M. NIEMINEN, *Mat. Sci. and Eng.: B* **159**, 107 (2009), doi:10.1016/j.mseb.2008.10.040.
- [100] B. B. NIELSEN, L. HOFFMANN, and M. BUDDE, *Mat. Sci. and Eng.: B* **36**, 259 (1996), doi:10.1016/0921-5107(95)01260-5.
- [101] Z. F. DI, Y. Q. WANG, M. NASTASI, L. SHAO, J. K. LEE, and N. D. THEODORE, *Appl. Phys. Lett.* **93**, 104103 (2008), doi:10.1063/1.2979686.
- [102] N. ROCHAT, A. TAUZIN, F. MAZEN, and L. CLAVELIER, *Electrochem. Solid-State Lett.* **13**, G40 (2010), doi:10.1149/1.3329611.
- [103] E. V. LAVROV, J. WEBER, L. HUANG, and B. B. NIELSEN, *Phys. Rev. B* **64**, 035204 (2001), doi:10.1103/PhysRevB.64.035204.
- [104] W. DÜNGEN, R. JOB, Y. MA, Y. L. HUANG, T. MUELLER, W. R. FAHRNER, L. O. KELLER, J. T. HORSTMANN, and H. FIEDLER, *J. Appl. Phys.* **100**, 034911 (2006), doi:10.1063/1.2227262.
- [105] B. B. NIELSEN, P. JOHANNESSEN, P. STALLINGA, K. B. NIELSEN, and J. R. BYBERG, *Phys. Rev. Lett.* **79**, 1507 (1997), doi:10.1103/PhysRevLett.79.1507.
- [106] F. S. HAM, *J. Lum.* **85**, 193 (2000), doi:10.1016/S0022-2313(99)00187-8.
- [107] P. RAGHUNATHAN and K. SHIMOKOSHI, *Spec. Acta Part A: Mol. Spec.* **36**, 285 (1980), doi:10.1016/0584-8539(80)80133-4.
- [108] W. WELTNER, *Magnetic atoms and molecules*, Dover Publications, 1989.
- [109] G. S. JACKEL and W. GORDY, *Phys. Rev.* **176**, 443 (1968), doi:10.1103/PhysRev.176.443.
- [110] M. J. FRISCH, G. W. TRUCKS, H. B. SCHLEGEL, G. E. SCUSERIA, M. A. ROBB, J. R. CHEESEMAN, J. J. A. MONTGOMERY, T. VREVEN, K. N. KUDIN, J. C. BURANT, J. M. MILLAM, S. S. IYENGAR, J. TOMASI, V. BARONE, B. MENNUCCI, M. COSSI, G. SCALMANI, N. REGA, G. A. PETERSSON, H. NAKATSUJI, M. HADA, M. EHARA, K. TOYOTA, R. FUKUDA, J. HASEGAWA, M. ISHIDA, T. NAKAJIMA, Y. HONDA, O. KITAO, H. NAKAI, M. KLENE, X. LI, J. E. KNOX, H. P. HRATCHIAN, J. B. CROSS, V. BAKKEN, C. ADAMO, J. JARAMILLO, R. GOMPERTS, R. E. STRATMANN, O. YAZYEV, A. J. AUSTIN, R. CAMMI,

- C. POMELLI, J. W. OCHTERSKI, P. Y. AYALA, K. MOROKUMA, G. A. VOTH, P. SALVADOR, J. J. DANNENBERG, V. G. ZAKRZEWSKI, S. DAPPRICH, A. D. DANIELS, M. C. STRAIN, O. FARKAS, D. K. MALICK, A. D. RABUCK, K. RAGHAVACHARI, J. B. FORESMAN, J. V. ORTIZ, Q. CUI, A. G. BABOUL, S. CLIFFORD, J. CIOSLOWSKI, B. B. STEFANOV, G. LIU, A. LIASHENKO, P. PISKORZ, I. KOMAROMI, R. L. MARTIN, D. J. FOX, T. KEITH, M. A. AL-LAHAM, C. Y. PENG, A. NANAYAKKARA, M. CHALLACOMBE, P. M. W. GILL, B. JOHNSON, W. CHEN, M. W. WONG, C. GONZALEZ, and J. A. POPLE, Gaussian 03, Revision D.01, Gaussian, Inc., Wallingford, CT, 2004.
- [111] S. ÖĞÜT and J. CHELIKOWSKY, *Phys. Rev. Lett.* **91**, 235503 (2003), [doi:10.1103/PhysRevLett.91.235503](https://doi.org/10.1103/PhysRevLett.91.235503).
- [112] G. D. WATKINS and J. W. CORBETT, *Phys. Rev.* **138**, A543 (1965), [doi:10.1103/PhysRev.138.A543](https://doi.org/10.1103/PhysRev.138.A543).
- [113] J. G. DE WIT, E. G. SIEVERTS, and C. A. J. AMMERLANN, *Phys. Rev. B* **14**, 3494 (1976), [doi:10.1103/PhysRevB.14.3494](https://doi.org/10.1103/PhysRevB.14.3494).
- [114] E. G. SIEVERTS, S. H. MULLER, and C. A. J. AMMERLANN, *Phys. Rev. B* **18**, 6834 (1978), [doi:10.1103/PhysRevB.18.6834](https://doi.org/10.1103/PhysRevB.18.6834).
- [115] S. ÖĞÜT and J. CHELIKOWSKY, *Phys. Rev. Lett.* **83**, 3852 (1999), [doi:10.1103/PhysRevLett.83.3852](https://doi.org/10.1103/PhysRevLett.83.3852).
- [116] G. D. WATKINS, *Physica B* **376**, 50 (2006), [doi:10.1016/j.physb.2005.12.014](https://doi.org/10.1016/j.physb.2005.12.014).
- [117] D. V. MAKOV and L. J. LEWIS, *Phys. Rev. B* **72**, 073306 (2005), [doi:10.1103/PhysRevB.72.073306](https://doi.org/10.1103/PhysRevB.72.073306).
- [118] R. R. WIXOM and A. F. WRIGHT, *Phys. Rev. B* **74**, 205208 (2006), [doi:10.1103/PhysRevB.74.205208](https://doi.org/10.1103/PhysRevB.74.205208).
- [119] J. I. IWATA, K. SHIRAISHI, and A. OSHIYAMA, *Phys. Rev. B* **77**, 115208 (2008), [doi:10.1103/PhysRevB.77.115208](https://doi.org/10.1103/PhysRevB.77.115208).
- [120] H. XU, *Phys. Rev. B* **46**, 1403 (1992), [doi:10.1103/PhysRevB.46.1403](https://doi.org/10.1103/PhysRevB.46.1403).
- [121] J. COUTINHO, R. JONES, P. R. BRIDDON, and S. ÖBERG, *Phys. Rev. B* **62**, 10824 (2000), [doi:10.1103/PhysRevB.62.10824](https://doi.org/10.1103/PhysRevB.62.10824).
- [122] F. CORSETTI and A. A. MOSTOFI, *Phys. Rev. B* **84**, 035209 (2011), [doi:10.1103/PhysRevB.84.035209](https://doi.org/10.1103/PhysRevB.84.035209).
- [123] U. GERSTMANN, M. ROHRMÜLLER, F. MAURI, and W. G. SCHMIDT, *Phys. Stat. Sol. C* **7**, 157 (2010), [doi:10.1002/pssc.200982462](https://doi.org/10.1002/pssc.200982462).
- [124] M. COOK and C. T. WHITE, *Phys. Rev. B* **38**, 9674 (1988), [doi:10.1103/PhysRevB.38.9674](https://doi.org/10.1103/PhysRevB.38.9674).

- [125] P. STALLINGA, P. JOHANNESSEN, S. HERSTRØM, K. BONDE NIELSEN, B. BECH NIELSEN, and J. R. BYBERG, *Phys. Rev. B* **58**, 3842 (1998), [doi:10.1103/PhysRevB.58.3842](https://doi.org/10.1103/PhysRevB.58.3842).
- [126] R. H. LUCHSINGER, Y. ZHOU, and P. F. MEIER, *Phys. Rev. B* **55**, 6927 (1997), [doi:10.1103/PhysRevB.55.6927](https://doi.org/10.1103/PhysRevB.55.6927).
- [127] D. K. BIEGELSEN and M. STUTZMANN, *Phys. Rev. B* **33**, 3006 (1986), [doi:10.1103/PhysRevB.33.3006](https://doi.org/10.1103/PhysRevB.33.3006).
- [128] N. ISHII and T. SHIMIZU, *Sol. Stat. Comm.* **102**, 647 (1997), [doi:10.1016/S0038-1098\(97\)80074-9](https://doi.org/10.1016/S0038-1098(97)80074-9).
- [129] T. W. HERRING, S. Y. LEE, D. R. MCCAMEY, P. C. TAYLOR, K. LIPS, J. HU, F. ZHU, A. MADAN, and C. BOEHME, *Phys. Rev. B* **79**, 195205 (2009), [doi:10.1103/PhysRevB.79.195205](https://doi.org/10.1103/PhysRevB.79.195205).
- [130] M. FEHR, A. SCHNEGG, C. TEUTLOFF, R. BITTL, O. ASTAKHOV, F. FINGER, B. RECH, and K. LIPS, *Phys. Stat. Sol. A* **207**, 552 (2010), [doi:10.1002/pssa.2009828766](https://doi.org/10.1002/pssa.2009828766).
- [131] H. A. BENT, *Chem. Rev.* **61**, 275 (1961), [doi:10.1021/cr60211a005](https://doi.org/10.1021/cr60211a005).
- [132] F. YU and P. A. FEDDERS, *Sol. Stat. Comm.* **84**, 799 (1992), [doi:10.1016/0038-1098\(92\)90092-N](https://doi.org/10.1016/0038-1098(92)90092-N).
- [133] M. COOK and C. T. WHITE, *Semicond. Sci. Technol* **4**, 1012 (1989), [doi:10.1088/0268-1242/4/12/00](https://doi.org/10.1088/0268-1242/4/12/00).
- [134] R. SINGH, S. PRAKASH, N. N. SHUKLA, and R. PRASAD, *Phys. Rev. B* **70**, 115213 (2004), [doi:10.1103/PhysRevB.70.115213](https://doi.org/10.1103/PhysRevB.70.115213).
- [135] K. JAROLIMEK, R. A. DE GROOT, G. A. DE WIJS, and M. ZEMAN, *Phys. Rev. B* **79**, 155206 (2009), [doi:10.1103/PhysRevB.79.155206](https://doi.org/10.1103/PhysRevB.79.155206).
- [136] K. LAAZIRI, S. KYCIA, S. ROORDA, M. CHICOINE, J. L. ROBERTSON, J. WANG, and S. C. MOSS, *Phys. Rev. B* **60**, 13520 (1999), [doi:10.1103/PhysRevB.60.13520](https://doi.org/10.1103/PhysRevB.60.13520).
- [137] M. WAKAGI, K. OGATA, and A. NAKANO, *Phys. Rev. B* **50**, 10666 (1994), [doi:10.1103/PhysRevB.50.10666](https://doi.org/10.1103/PhysRevB.50.10666).
- [138] P. ROURA, J. FARJAS, and P. ROCA I CABARROCAS, *J. Appl. Phys.* **104**, 073521 (2008), [doi:10.1063/1.2990767](https://doi.org/10.1063/1.2990767).
- [139] J. H. STATHIS, *Phys. Rev. B* **40**, 1232 (1989), [doi:10.1103/PhysRevB.40.1232](https://doi.org/10.1103/PhysRevB.40.1232).
- [140] N. ISHII and T. SHIMIZU, *Phys. Rev. B* **42**, 9697 (1990), [doi:10.1103/PhysRevB.42.9697](https://doi.org/10.1103/PhysRevB.42.9697).

- [141] P. BISWAS, D. N. TAFEN, F. INAM, B. CAI, and D. A. DRABOLD, *J. Phys.: Cond. Matter* **21**, 084207 (2009), [doi:10.1088/0953-8984/21/8/084207](https://doi.org/10.1088/0953-8984/21/8/084207).
- [142] D. A. DRABOLD, *Eur. Phys. J. B* **68**, 1 (2009), [doi:10.1140/epjb/e2009-00080-0](https://doi.org/10.1140/epjb/e2009-00080-0).
- [143] P. BISWAS, R. ATTA-FYNN, and D. A. DRABOLD, *Phys. Rev. B* **69**, 195207 (2004), [doi:10.1103/PhysRevB.69.195207](https://doi.org/10.1103/PhysRevB.69.195207).
- [144] P. BISWAS, R. ATTA-FYNN, and D. A. DRABOLD, *Phys. Rev. B* **76**, 125210 (2007), [doi:10.1103/PhysRevB.76.125210](https://doi.org/10.1103/PhysRevB.76.125210).
- [145] G. OPLETAL, T. C. PETERSEN, I. K. SNOOK, and D. G. MCCULLOCH, *J. Chem. Phys.* **126**, 214705 (2007), [doi:10.1063/1.2743029](https://doi.org/10.1063/1.2743029).
- [146] N. MOUSSEAU and G. T. BARKEMA, *Current Op. Sol. Stat. and Mat. Sci.* **5**, 497 (2001), [doi:10.1016/S1359-0286\(02\)00005-0](https://doi.org/10.1016/S1359-0286(02)00005-0).
- [147] A. A. VALLADARES, F. ALVAREZ, Z. LUI, J. STICHT, and J. HARRIS, *Eur. Phys. J. B* **22**, 443 (2001), [doi:10.1007/s100510170094](https://doi.org/10.1007/s100510170094).
- [148] G. T. BARKEMA and N. MOUSSEAU, *Phys. Rev. B* **62**, 4985 (2000), [doi:10.1103/PhysRevB.62.4985](https://doi.org/10.1103/PhysRevB.62.4985).
- [149] G. T. BARKEMA and N. MOUSSEAU, *Phys. Rev. Lett.* **77**, 4358 (1996), [doi:10.1103/PhysRevLett.77.4358](https://doi.org/10.1103/PhysRevLett.77.4358).
- [150] P. BISWAS and R. TIMILSINA, *J. Phys.: Cond. Mat.* **23**, 065801 (2011), [doi:10.1088/0953-8984/23/6/065801](https://doi.org/10.1088/0953-8984/23/6/065801).
- [151] T. SU and P. C. TAYLOR, *Sol. Energ. Mat. Sol. Cells* **78**, 269 (2003), [doi:10.1016/S0927-0248\(02\)00439-7](https://doi.org/10.1016/S0927-0248(02)00439-7).
- [152] S. AGARWAL, B. HOEX, M. C. M. VAN DE SANDEN, D. MAROUDAS, and E. S. AYDIL, *J. Vac. Sci & Tech. B: Microelectrons and Nanometer Structures* **22**, 2719 (2004), [doi:10.1116/1.1824191](https://doi.org/10.1116/1.1824191).
- [153] P. A. FEDDERS, L. D. J., P. H. CHAN, R. BORZI, and R. E. NORBERG, *Phys. Rev. Lett.* **85**, 401 (2000), [doi:10.1103/PhysRevLett.85.401](https://doi.org/10.1103/PhysRevLett.85.401).
- [154] G. LUCOVSKY, R. J. NEMANICH, and J. C. KNIGHTS, *Phys. Rev. B* **19**, 2064 (1979), [doi:10.1103/PhysRevB.19.2064](https://doi.org/10.1103/PhysRevB.19.2064).
- [155] C. MANFREDOTTI, F. FIZZOTTI, P. PASTORINO, P. POLESELLO, and E. VIT-TONE, *Phys. Rev. B* **50**, 18046 (1994), [doi:10.1103/PhysRevB.50.18046](https://doi.org/10.1103/PhysRevB.50.18046).
- [156] K. JAROLIMEK, G. A. DE WIJS, R. A. DE GROOT, and M. ZEMAN, *Phys. Stat. Sol. A* **207**, 605 (2010), [doi:10.1002/pssa.200982724](https://doi.org/10.1002/pssa.200982724).

- [157] M. STUTZMANN, W. B. JACKSON, and C. C. TSAI, *Phys. Rev. B* **32**, 23 (1985), [doi:10.1103/PhysRevB.32.23](https://doi.org/10.1103/PhysRevB.32.23).
- [158] K. MORIGAKI and H. HIKITA, *Phys. Rev. B* **76**, 085201 (2007), [doi:10.1103/PhysRevB.76.085201](https://doi.org/10.1103/PhysRevB.76.085201).
- [159] P. BROQVIST, A. ALKAUSKAS, and A. PASQUARELLO, *Phys. Rev. B* **78**, 075203 (2008), [doi:10.1103/PhysRevB.78.075203](https://doi.org/10.1103/PhysRevB.78.075203).
- [160] C. VAN DE WALLE, *Hydrogen Interactions with Polycrystalline and Amorphous Silicon - Theory*, volume 61 of *Hydrogen in semiconductors II*, p. 241, Academic Press, 1999, [doi:10.1016/S0080-8784\(08\)62708-8](https://doi.org/10.1016/S0080-8784(08)62708-8).
- [161] B. R. TUTTLE, *Phys. Rev. Lett.* **93**, 215504 (2004), [doi:10.1103/PhysRevLett.93.215504](https://doi.org/10.1103/PhysRevLett.93.215504).
- [162] S. PANTELIDES, *Phys. Rev. Lett.* **57**, 2979 (1986), [doi:10.1103/PhysRevLett.57.2979](https://doi.org/10.1103/PhysRevLett.57.2979).
- [163] S. CHAKRABORTY and D. A. DRABOLD, *Phys. Rev. B* **79**, 115214 (2009), [doi:10.1103/PhysRevB.79.115214](https://doi.org/10.1103/PhysRevB.79.115214).
- [164] T. UMEDA, *Physica B* **376**, 249 (2006), [doi:10.1016/j.physb.2005.12.065](https://doi.org/10.1016/j.physb.2005.12.065).
- [165] P. BIWAS, C. Z. WANG, C. T. CHAN, K. M. HO, and C. M. SOUJOLIS, *Phys. Rev. Lett.* **63**, 1491 (1989), [doi:10.1103/PhysRevLett.63.1491](https://doi.org/10.1103/PhysRevLett.63.1491).
- [166] P. A. FEDDERS, D. A. DRABOLD, P. ORDEJÓN, G. FABRICIUS, D. SÁNCHEZ-PORTAL, E. ARTACHO, and J. M. SOLER, *Phys. Rev. B* **60**, 10594 (1999), [doi:10.1103/PhysRevB.60.10594](https://doi.org/10.1103/PhysRevB.60.10594).
- [167] S. KNIEF and W. VON NIESSEN, *Phys. Rev. B* **60**, 5412 (1999), [doi:10.1103/PhysRevB.60.5412](https://doi.org/10.1103/PhysRevB.60.5412).
- [168] P. BISWAS and B. C. PAN, *Appl. Phys. Lett.* **72**, 371 (1998), [doi:10.1063/1.120740](https://doi.org/10.1063/1.120740).
- [169] M. J. POWELL, S. C. DEANE, and R. B. WEHRSPHON, *Phys. Rev. B* **66**, 155212 (2002), [doi:10.1103/PhysRevB.66.155212](https://doi.org/10.1103/PhysRevB.66.155212).
- [170] L. K. WAGNER and J. C. GROSSMAN, *Phys. Rev. Lett.* **101**, 265501 (2008), [doi:10.1103/PhysRevLett.101.265501](https://doi.org/10.1103/PhysRevLett.101.265501).
- [171] P. A. KHOMYAKOV, W. ANDREONI, N. D. AFIFY, and A. CURIONI, *Phys. Rev. Lett.* **107**, 255502 (2011), [doi:10.1103/PhysRevLett.107.255502](https://doi.org/10.1103/PhysRevLett.107.255502).
- [172] N. ISHII and T. SHIMIZU, *J. Non-Crys. Solids* **227**, 358 (1998), [doi:10.1016/S0022-3093\(98\)00076-3](https://doi.org/10.1016/S0022-3093(98)00076-3).
- [173] J. E. NORTHRUP, *Phys. Rev. B* **40**, 5875 (1989), [doi:10.1103/PhysRevB.40.5875](https://doi.org/10.1103/PhysRevB.40.5875).

- [174] A. ALKAUSKAS, P. BROQVIST, and A. PASQUARELLO, *Defect Levels Through Hybrid Density Functionals: Insights and Applications*, Advanced Calculations for Defects in Materials: Electronic Structure Methods, Wiley-VCH, 2011, [doi:10.1002/9783527638529.ch7](https://doi.org/10.1002/9783527638529.ch7).
- [175] M. J. POWELL and S. C. DEANE, *Phys. Rev. B* **48**, 10815 (1993), [doi:10.1103/PhysRevB.48.10815](https://doi.org/10.1103/PhysRevB.48.10815).
- [176] H. GLESKOVA, I. C. CHENG, S. WAGNER, J. C. STURM, and Z. SUO, *Solar Energy* **80**, 687 (2006).
- [177] E. JOHLIN, N. Tabet, S. CASTRO-GALNARES, A. ABDALLAH, M. I. BERTONI, T. ASAFA, J. C. GROSSMAN, S. SAID, and T. BUONASSISI, *Phys. Rev. B* **85**, 075202 (2012), [doi:10.1103/PhysRevB.85.075202](https://doi.org/10.1103/PhysRevB.85.075202).
- [178] A. KERRACHE, N. MOUSSEAU, and L. J. LEWIS, *Phys. Rev. B* **83**, 134122 (2011), [doi:10.1103/PhysRevB.83.134122](https://doi.org/10.1103/PhysRevB.83.134122).



# Acknowledgements

Tradition has it that the acknowledgement section comes last. It is also common that it is only written as the tight deadline is fast approaching. Well, that is also the case here, and I realize that this page will not be as creative as I had planned it now for years. I can only put down what I am thinking right now, and even if that is not much, it is at least honest.

I think the person I would like to thank first and foremost, is definitely my supervisor Dr. Christoph Freysoldt, who invested a lot of his time (and nerves?) in this project. Dear Christoph, thank you so much for supervising me, thank you for all the nice discussions we had, and thank you for all the hours you spent correcting my thesis. It was a great joy to work with you on this topic and your dedication to science is exemplary. I also want to thank you for your patience and understanding, whenever things were not going too well. Overall I have learned a lot from you and you have made a huge impact on me.

Similarly, I would also like to thank Professor Jörg Neugebauer for valuable criticism of my work as well as providing me with this great, inspiring working environment in the CM-department.

I would like to thank all the partners from the EPR-solar network, most notably Dr. Matthias Fehr, as well as Dr. Uwe Gerstmann for all the discussions and suggestions.

I am also very grateful for all the help, which the 'computer people' provided to solve technical problems. This in particular includes Ingeborg Weidl, Ulrich Wellms, Wolfgang Vogt and Dr. Sixten Boeck.

I thank Dr. Andrew Duff, Dr. Chris Race, Dr. Fritz Körmann, and Dr. Johann von Pezold for proof-reading my thesis, and Björn Lange for helping me with formatting issues of this thesis.

Of course, I would also like to thank my family and friends for all their support.

Finally, I would like to thank you, my fellow reader, for reading this thesis to this point.

# List of publications

## Diploma thesis

- *Phonon-Assisted Decoherence in the Production of Polarization-Entangled Photons in a Single Semiconductor Quantum Dot* - HOHENESTER, PFANNER, SELIGER, [Phys. Rev. Lett. 99, 047402](#) (2007)
- *Entangled photon sources based on semiconductor quantum dots: The role of pure dephasing* - PFANNER, SELIGER, HOHENESTER, [Phys. Rev. B 78, 195410](#) (2008)
- *Entangled photons from quantum dot devices: efficiency of post-selection* - SELIGER, HOHENESTER, PFANNER, [physica status solidi \(b\) 246, 289](#) (2008)

## PhD thesis

- *Ab initio study of electron paramagnetic resonance hyperfine structure of the silicon dangling bond: Role of the local environment* - PFANNER, FREYSOLDT, NEUGEBAUER, [Phys. Rev. B 83, 144110](#) (2011)
- *Combined multifrequency EPR and DFT study of dangling bonds in a-Si:H* - FEHR, SCHNEGG, RECH, LIPS, ASTAKHOV, FINGER, PFANNER, FREYSOLDT, NEUGEBAUER, BITTL, TEUTLOFF, [Phys. Rev. B 84, 245203](#) (2011)
- *Ab initio EPR parameters for dangling-bond defect complexes in silicon: Effect of Jahn-Teller distortion* - PFANNER, FREYSOLDT, NEUGEBAUER, GERSTMANN, [Phys. Rev. B 85, 195202](#) (2012)
- *The dangling-bond defect in amorphous silicon: Statistical random versus kinetically driven defect geometries* - FREYSOLDT, PFANNER, NEUGEBAUER, [J. Non-Crys. Solids, doi:10.1016/j.jnoncrysol.2011.12.090](#) (in press)
- *The dangling-bond defect in a-Si:H: Characterization of network and strain effects by first-principles calculation of the EPR-parameters* - PFANNER, FREYSOLDT, NEUGEBAUER, INAM, DRABOLD, JAROLIMEK, ZEMAN (in preparation)

# Erklärungen

Hiermit versichere ich diese Arbeit selbstständig verfasst und keine anderen als die angegebenen Quellen und Hilfsmittel verwendet zu haben.

\_\_\_\_\_  
(Ort, Datum)

\_\_\_\_\_  
(Unterschrift)

Hiermit versichere ich in Kenntnis der geltenden Promotionsordnung zu sein.

\_\_\_\_\_  
(Ort, Datum)

\_\_\_\_\_  
(Unterschrift)

Hiermit versichere ich, dass ich weder zu einem früheren Zeitpunkt noch zum jetzigen ein Promotionsverfahren bei einem anderen Fachbereich bzw. einer anderen Fakultät beantragt habe.

\_\_\_\_\_  
(Ort, Datum)

\_\_\_\_\_  
(Unterschrift)